

AD-A256 004



AFOSR-TR-92 0874

2

GRADUATE AERONAUTICAL LABORATORIES CALIFORNIA INSTITUTE OF TECHNOLOGY

Chemical Reactions in Turbulent Mixing Flows

Paul E. Dimotakis*, James E. Broadwell** and Anthony Leonard†

Air Force Office of Scientific Research
Grant No. 90-0304
Final Technical Report: Period ending 14 May 1992

DTIC
ELECTE
SEP 23 1992
S A D

15 July 1992

This document has been approved
for public release and sale; its
distribution is unlimited.

Firestone Flight Sciences Laboratory

Guggenheim Aeronautical Laboratory

Karman Laboratory of Fluid Mechanics and Jet Propulsion

92 9 22 100 157700 92-25669



Pasadena

GRADUATE AERONAUTICAL LABORATORIES
CALIFORNIA INSTITUTE of TECHNOLOGY
Pasadena, California 91125

Chemical Reactions in Turbulent Mixing Flows

Paul E. Dimotakis*, James E. Broadwell** and Anthony Leonard†

Air Force Office of Scientific Research
Grant No. 90-0304
Final Technical Report: Period ending 14 May 1992

15 July 1992

Accession For	
NTIS CRA&I	<input checked="" type="checkbox"/>
DTIC TAB	<input type="checkbox"/>
Unannounced	<input type="checkbox"/>
Justification	
By	
Distribution /	
Availability Codes	
Dist	Avail and/or Special
A-1	

* Professor, Aeronautics & Applied Physics.

** Senior Scientist, Aeronautics.

† Professor, Aeronautics.

DTIC QUALITY INSPECTED 3

REPORT DOCUMENTATION PAGE			Form Approved OMB No. 0704-0188	
<small>Public reporting burden for this collection of information is estimated to average 1 hour per response, including the time for reviewing instructions, searching existing data sources, gathering and maintaining the data needed, and completing and reviewing the collection of information. Send comments regarding this burden estimate or any other aspect of this collection of information, including suggestions for reducing this burden, to Washington Headquarters Services, Directorate for Information Operations and Reports, 1215 Jefferson Davis Highway, Suite 1204, Arlington, VA 22202-4302, and to the Office of Management and Budget, Paperwork Reduction Project (0704-0188), Washington, DC 20503.</small>				
1. AGENCY USE ONLY (Leave blank)		2. REPORT DATE 15 July 1992		3. REPORT TYPE AND DATES COVERED Final: 15 May 1991 - 14 May 1992
4. TITLE AND SUBTITLE Chemical Reactions in Turbulent Mixing Flows (w)			5. FUNDING NUMBERS PE - 61102F PR - 2308 SA - BS G - AFOSR-90-0304	
6. AUTHOR(S) Paul E. Dimotakis James E. Broadwell Anthony Leonard				
7. PERFORMING ORGANIZATION NAME(S) AND ADDRESS(ES) California Institute of Technology Graduate Aeronautical Laboratories Mail Stop 301-46 Pasadena, CA 91125			8. PERFORMING ORGANIZATION REPORT NUMBER	
9. SPONSORING/MONITORING AGENCY NAME(S) AND ADDRESS(ES) AFOSR/NA Building 410 Bolling AFB DC 20332-6448			10. SPONSORING/MONITORING AGENCY REPORT NUMBER	
11. SUPPLEMENTARY NOTES				
12a. DISTRIBUTION/AVAILABILITY STATEMENT Approved for public release; distribution is unlimited			12b. DISTRIBUTION CODE	
13. ABSTRACT (Maximum 200 words) The purpose of this research is to conduct fundamental investigations of turbulent mixing, chemical reaction and combustion processes in turbulent, subsonic and supersonic flows. Our approach has been to carry out a series of detailed theoretical and experimental studies of turbulent mixing in both free shear layers and axisymmetric jets. To elucidate molecular transport effects, experiments and theory concern themselves with both reacting and non-reacting flows of liquids and gases, in fully-developed turbulent flows, i.e., in moderate to high Reynolds number flows. The computational studies are, at present, focused at fundamental issues pertaining to the computational simulation of both compressible and incompressible flows. Modeling has been focused on both shear layers and turbulent jets, with an effort to include the physics of the molecular transport processes, as well as formulations of models that permit the full chemical kinetics of the combustion process to be incorporated. Our primary diagnostic development efforts are currently focused on data-acquisition electronics to meet very high-speed, high-volume data requirements, the acquisition of single, or a sequence, of two-dimensional images, and the acquisition of data from arrays of supersonic flow sensors. Progress has also been made in the development of a dual-beam laser interferometer/correlator to measure convection velocities of large scale structures in supersonic shear layers and in a new method to acquire velocity field data using pairs of scalar images closely spaced in time.				
14. SUBJECT TERMS Turbulence, shear Layers, jets, mixing, combustion, numerical simulation, fractals, turbulent mixing modeling, velocimetry			15. NUMBER OF PAGES 75	
			16. PRICE CODE	
17. SECURITY CLASSIFICATION OF REPORT Unclassified	18. SECURITY CLASSIFICATION OF THIS PAGE Unclassified	19. SECURITY CLASSIFICATION OF ABSTRACT Unclassified	20. LIMITATION OF ABSTRACT UL	

Abstract

The purpose of this research is to conduct fundamental investigations of turbulent mixing, chemical reaction and combustion processes in turbulent, subsonic and supersonic flows. Our program is comprised of several parts:

- a. an experimental effort,
- b. an analytical effort,
- c. a computational effort,
- d. a modeling effort,

and

- e. a diagnostics development and data-acquisition effort,

the latter as dictated by specific needs of the experimental part of the overall program.

Our approach has been to carry out a series of detailed theoretical and experimental studies of turbulent mixing in primarily in two, well-defined, fundamentally important flow fields: free shear layers and axisymmetric jets.

To elucidate molecular transport effects, experiments and theory concern themselves with both reacting and non-reacting flows of liquids and gases, in fully-developed turbulent flows, *i.e.*, in moderate to high Reynolds number flows. The computational studies are, at present, focused at fundamental issues pertaining to the computational simulation of both compressible and incompressible flows. Modeling has been focused on both shear layers and turbulent jets, with an effort to include the physics of the molecular transport processes, as well as formulations of models that permit the full chemical kinetics of the combustion process to be incorporated. Our primary diagnostic development efforts are currently focused on data-acquisition electronics to meet very high-speed, high-volume data requirements, the acquisition of single, or a sequence, of two-dimensional images, and the acquisition of data from arrays of supersonic flow sensors. Progress has also been made in the development of a dual-beam laser interferometer/correlator to measure convection velocities of large scale structures in supersonic shear layers and in a new method to acquire velocity field data using pairs of scalar images closely spaced in time.

1. Introduction

We have made progress under the sponsorship of this Grant, for the period ending 14 May 1992, in several areas. A review paper documenting much of the work at Caltech in shear layer mixing and combustion in the last ten years, or so, has appeared as Chapter 5 in the *High-Speed Flight Propulsion Systems*, Volume 137 of the *AIAA Progress Series in Astronautics and Aeronautics* (Dimotakis 1991). Copies are available on request.

In our experimental effort in supersonic shear layers, we have increased the high-speed stream Mach number to 2.5 and performed a first set of exploratory investigations at this higher compressibility condition. We have also performed a first set of experiments in the transonic shear layer regime.

In our investigations of turbulent jets,[†] two theses are now available. *An Experimental Investigation of Chemically-Reacting, Gas-Phase Turbulent Jets* (Gilbrech 1991), that explored Reynolds number effects on turbulent flame length and the influence of buoyancy on turbulent jet flames; and *Mixing in High Schmidt Number Turbulent Jets* (Miller 1991), that examined Reynolds number effects, Schmidt number effects, and the influence of initial conditions on the turbulent jet's mixing behavior. Progress has also been made in understanding buoyancy effects in turbulent jets, with an eye in understanding the mixing enhancement that we have documented occurs under certain conditions. Finally the development of jet mixing models that permit the inclusion of full chemical kinetics calculations has also progressed, with considerable improvements in the quantitative descriptions of a host of phenomena, including NO_x production by turbulent jet flames.

In our analytical/computational effort, we are developing new, reliable methods for computing interactions of shock waves and other discontinuous waves that may arise in multidimensional, unsteady compressible flows.

In our diagnostics effort, we are continuing our progress with a new generation of high-speed, high-volume data acquisition systems, with the development of a new two-beam laser correlator to measure turbulent structure convection velocities, and a new method to measure velocity field information from pairs of images.

[†] The investigations of turbulent mixing and combustion in turbulent jets are co-sponsored by the Gas Research Institute.

2. Mixing and combustion in supersonic, turbulent shear layers

Some preliminary runs were made during the last year at a high-speed stream Mach number of 2.5 and at compressible but subsonic flow conditions. Both of these showed new and interesting phenomena. However, on 28 June 1991, the Sierra Madre earthquake caused a major disruption to the Supersonic Shear Layer (S^3L) combustion facility. The high pressure tank seal developed a leak, forcing a significant design reevaluation and repair effort. While that effort was in progress, a new instrument designed to measure large-scale-structure convection velocities was being developed. These are important for modeling chemically reacting shear layers.

2.1 Preliminaries at Mach 2.5

The expansion of the operating range of the facility to a high-speed stream Mach number of 2.5 was begun in May 1991 with Dr. Jeffery Hall. This work was left in the preliminary stage due to several factors; the discovery of a flaw in the original design of the S^3L test section splitter plate and the earthquake damage to the high speed supply tank. Despite these shortcomings, significant new information was gleaned from these preliminary runs. Based on previous experience, the growth rate of these cases should be very close to runs at ideal conditions; additionally, the structures indicated by the travelling waves are a robust manifestation of supersonic convection velocities of turbulent structures with respect to the shear layer free streams.

The new $M_1 = 2.5 [N_2]$ runs provide highly compressible flows with a different density ratio from our previous $M_1 = 1.55 [He]$ runs (Hall 1991). These flows have similar isentropic convective Mach numbers with respect to each stream. Both runs exhibit travelling waves in the low-speed stream, but the wave speeds are different, due, in large part, to the lower (absolute) speed of the $M_1 = 2.5 [N_2]$ stream ($U_1 = 600$ m/s), as opposed to the $M_1 = 1.55 [He]$ stream ($U_1 = 1100$ m/s). The normalized growth rates also are consistent (for the most part) with the established body of data, at this time, except for the N_2/Ar case. The latter, however, was found to have a non-zero pressure gradient. Although the lowest compressibility case seems to have a low normalized growth rate, this was not unexpected. By this criterion, it is similar to the low density ratio cases from previous experiments at $M_1 \simeq 1.5$.



FIG. 1 Supersonic shear layer schlieren image data: $M_1 = 2.5[\text{N}_2]$ over $U_2 = 80 \text{ m/s} [\text{Ar}]$.

The $M_1 = 2.5[\text{He}]$ runs showed some unexpected but not unprecedented results. These runs were characterized by much higher compressibility, *i.e.*, high convective Mach numbers, than any previous runs in the S³L facility. The expected travelling waves on the low-speed side were seen, and fast-response pressure transducers were used to measure their convection velocities using correlation techniques. Unexpectedly, the high speed stream also showed signs of travelling waves. See Fig. 2. The fast pressure transducers confirmed this, giving a velocity of $U_{c1} \simeq 350 \text{ m/s}$ in a stream with a velocity close to $U_1 = 1500 \text{ m/s}$.

Two other features of interest were observed in the same cases. A density decrease on the upper edge of the layer (*cf.* Figs. 1 and 2) and a normalized growth rate of 30 – 35% of the incompressible value. Most presently available data at such high compressibility show a growth rate only $\sim 20\%$ of the incompressible value. The density decrease is of interest because it implies that the helium is heating up from the freestream (static) temperature value of $T_1 \simeq 97 \text{ K}$ before mixing to any significant extent with the N_2 low-speed stream. There is reason to believe that the three unusual factors are related.

The schlieren data pictures of these flows show evidence of the original design shortcomings. Waves can be seen to emanate from the supersonic nozzle in both cases. In the N_2 run, this was caused by one factor. The original design underestimated the bending loads on the test section splitter plate tip; the support is too far back to prevent the plate from elastically bending by about 0.060 in., when exposed to the $p_{01} \simeq 17 \text{ atm}$ required in the plenum for $M_1 \simeq 2.5$. The deflection, in effect, results in a two-dimensional expansion nozzle with a slightly incorrect shape.

This problem has been addressed by a redesign that should result in a deflection

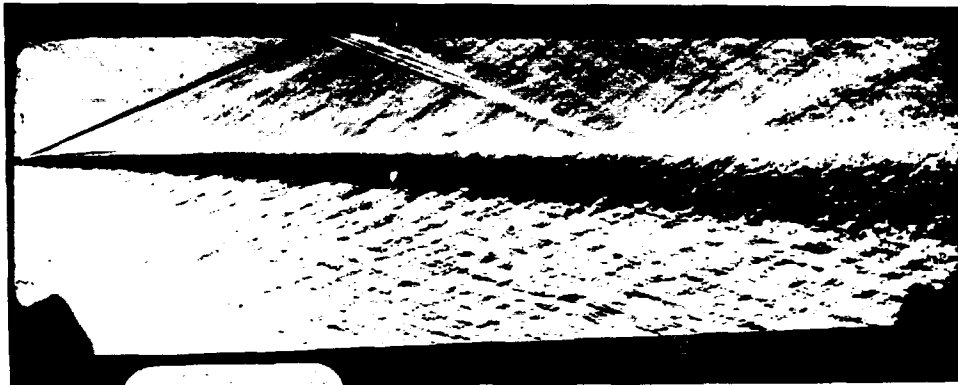


FIG. 2 Supersonic shear layer schlieren image data: $M_1 \simeq 2.5[\text{He}]$ over $U_2 = 100 \text{ m/s}[\text{N}_2]$.

that is less than 0.001 in., with plenum pressures as high as 50 atm. By way of comparison, the $M_1 \simeq 1.5$ flows require a plenum pressure that is less than 4 atm. In the helium high-speed stream case, the waves are stronger and the shear layer can be seen to bend. This is a result of using the same nozzle, originally designed for N_2 ($\gamma \equiv c_p/c_v = 7/5$), with He ($\gamma \simeq 5/3$), as we did for the $M_1 = 1.5$ runs. At $M_1 = 1.5$, the two contours are almost identical. At $M_1 = 2.5$, however, the differences are too large. A new nozzle block has been designed and fabricated to rectify this problem.

In previous experiments in the S^3L facility, we had found that even strong wave interactions with the shear layer produced relatively weak effects on the growth rate of the shear layer. This gives some confidence that the growth rate observed in the current flows is close (within a few percent) to the growth rate of a compressible shear layer that should be expected under ideal flow conditions. The $M_1 = 2.5[\text{N}_2]$ flows are only slightly affected; the shear layer is still straight. The $M_1 = 2.5[\text{He}]$ flows are more affected by the nozzle shape mismatch; the shear layer can be seen to bend on interaction with the waves emanating from the nozzle. Despite this, the turbulence-generated travelling waves are a robust feature of the flow. They initially appear at the splitter plate and do not change as the stationary waves emanating from the nozzle interact with them. As a consequence, we can expect that the growth rate (Fig. 3) and the travelling waves are not significantly influenced by the complications resulting from nozzle shape imperfections.

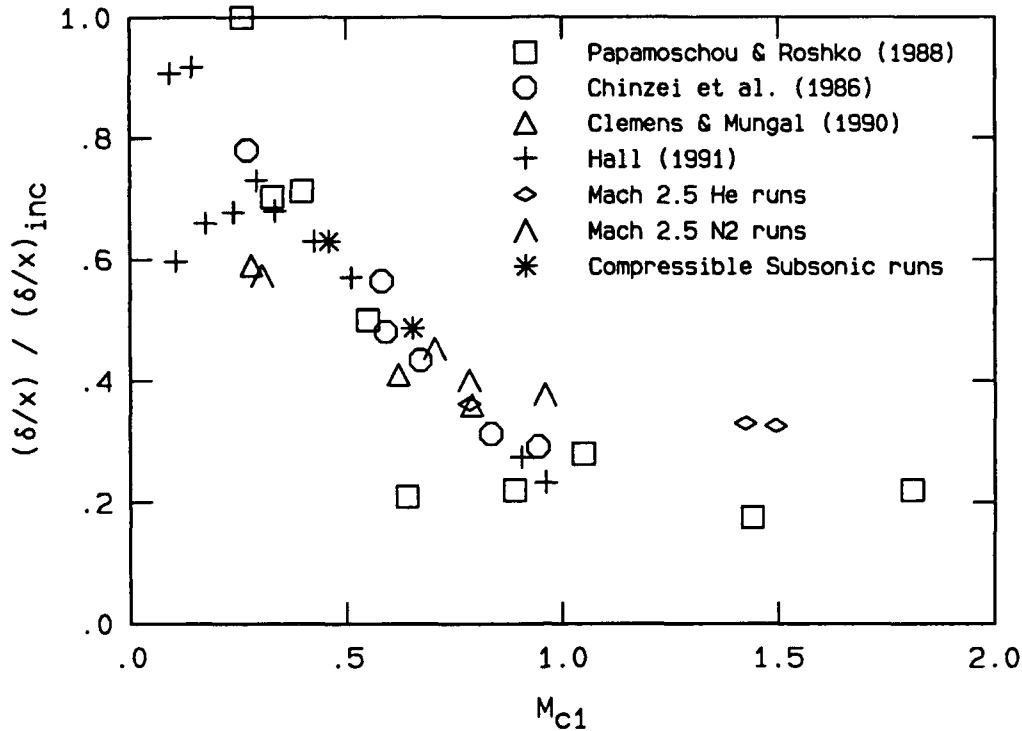


FIG. 3 Compressible shear layer normalized growth rate data: New $M_1 = 2.5$ and subsonic runs, as well as previous data.

2.2 Compressible subsonic shear layer flows

Several runs were made with a transonic, $M_1 = 0.97$ [He] high-speed stream, over a $U_2 = 50$ m/s [N₂] low-speed stream. As can be seen in Fig. 4, *although both sides were subsonic, weak travelling waves are discernible on the low-speed side*. It should be noted that, under these conditions, the growth rate is so high that the shear layer attaches to the lower guidewall (just beyond the end of the field of view in the picture). The contrast between the shear layer in Fig. 4 and those in Figs. 1 and 2 should not escape unnoticed. Despite this high growth, the normalized growth rate fits well with other cases of comparable compressibility. This addresses a significant issue and provides evidence that the whether the flow is hyperbolic, or not (*e.g.*, Papamoschou 1989), is less important than the compressibility of the shear layer. The growth rates for this, and a less compressible, case with no travelling waves are plotted in Fig. 3.



FIG. 4 Transonic shear layer schlieren image data: $M_1 = 0.97$ [He], over $U_2 = 50$ m/s [N₂].

2.3 Recent earthquakes and required repairs

Work on both the efforts described above was interrupted by a major repair job necessitated by the June 1991 Sierra Madre earthquake. After discovering the leak, we were forced to stop experiments. In addition to considering simply replacing the seal, other alternatives were investigated. These alternatives included remanufacturing the tank to eliminate the large 36 in. flange. Unfortunately, the necessity of including the high heat capacity aluminum packing to prevent a significant stagnation temperature drop in the high speed stream, in the course of a run, prevented the most favorable resolution: the heat-treating temperature of the welds (as required by the high pressure vessel code for hydrogen-capable tanks) is too close to the melting temperature of aluminum.

In the end, we decided to replace the seal, with several steps taken to minimize the probability of future problems. Specifically, the seal material was changed to one that gives the closest coefficient of thermal expansion to minimize thermal stresses when the tank heating is activated. In addition, a ultrasonic measuring device was used, in retorquing the large flange bolts, to ensure that a uniform and sufficient tension was placed on the bolts. This should give the best chance to prevent damage from any future event by giving us a level of consistency which could not be obtained merely by tightening to a fixed torque. For better or for worse, we had the opportunity to test this. Following the recent Landers earthquake (28 June 1992, magnitude 7.4, 90 miles east of Pasadena) and long sequence of strong aftershocks, we loaded the large tank to working pressure with helium. No leaks were found using a sensitive helium leak detector.

2.4 Design of a new instrument

At this time, travelling waves provide us with the only means of measuring the turbulent structure(s) convection velocity. Accurate chemical kinetic modelling of the reacting shear layer depends significantly upon this velocity as it determines the time of flight and also enters in the modeling of the entrainment ratio. Specifically, a higher velocity gives a shorter time for reactions and thus raises the required concentrations/temperatures for fast chemistry. A relative velocity ratio with respect to the two freestreams provides an asymmetric entrainment environment. There is a possibility that the wave velocity might not be the only velocity in the shear layer; if the wave velocity is not the fluid velocity, then a model based on the wave velocity could be significantly wrong. For this reason, a new instrument was designed to measure density (index of refraction) interface convection velocities. This should be able to measure both the fluid velocity and wave velocities, whether they are the same or different.

3. Mixing and combustion in turbulent jets

The research effort on turbulent jet mixing, involving both the gas-phase, chemically reacting and liquid-phase, non-reacting jet investigations, is cosponsored by the Gas Research Institute, GRI Contract No. 5087-260-1467.

3.1 Gas-phase chemically reacting jet investigations

The results described below are from the Ph.D. thesis by Gilbrech (1991) that was completed during the last year (copies are available on request). A paper describing some of the work (Gilbrech & Dimotakis 1992) is included as Appendix B of this report. The experimental investigations reported in the thesis investigate a steady, effectively unconfined, chemically-reacting turbulent jet issuing into a quiescent reservoir. The Reynolds number (based on the nozzle exit diameter) is varied through pressure, *i.e.*, density, with the jet exit velocity and exit diameter held constant. The time-averaged line integral of temperature, measured along the transverse axis of the jet by the wires, displays a logarithmic dependence on x/d^* within the flame zone, and asymptotes to a constant value beyond the flame tip. The main result of the work is that the flame length, as estimated from the temperature measurements, varies with changes in Reynolds number, suggesting that the mixing process is not Reynolds number independent up to $Re = 1.5 \times 10^5$. Specifically, the normalized flame length L_f/d^* displays a linear dependence on the stoichiometric mixture ratio ϕ , with a slope that decreases from $Re \simeq 1.0 \times 10^4$ to $Re \simeq 2.0 \times 10^4$, and then remains constant for $Re > 2.0 \times 10^4$. Additionally, the measurements revealed a "mixing virtual origin," defined as the far-field flame length extrapolated to $\phi = 0$, that increases with increasing Reynolds number, for $Re \leq 2.0 \times 10^4$ and then decreases with increasing Reynolds number for $Re > 2.0 \times 10^4$.

The chemically reacting jet experiments were performed at a Damköhler number greater than 5.2, a value found to be the threshold to the fast chemistry regime.

To insure that the turbulent jets investigated were momentum dominated to the farthest measuring station, a separate set of experiments was performed. In these experiments, the adiabatic flame temperature ΔT_f was raised to where buoyancy affected the product thickness δ_p distribution and the logarithmic dependence on x/d^* of the time-averaged line integral of temperature no longer held. Under these conditions, it was found that molecular mixing is enhanced.

3.1.1 Stoichiometric mixture ratio and Reynolds number effects

All runs were performed at pressures between $1 \text{ atm} \leq p \leq 15 \text{ atm}$. The jet gas was always F_2 in a N_2 diluent and the reservoir gas was always NO in a N_2 diluent.

Experiments at four stoichiometric mixture ratios, ϕ , were performed at each Reynolds number to produce four different flame lengths. In this study, ϕ is defined in the usual manner as the mass fraction of F_2 in N_2 , divided by the mass fraction of NO in N_2 , normalized by the corresponding stoichiometric mass fraction ratio, i.e.,

$$\phi \equiv \frac{(Y_{\text{F}_2}/Y_{\text{NO}})}{(Y_{\text{F}_2}/Y_{\text{NO}})_{\text{st}}} \quad , \quad (1)$$

where the mass fraction, Y_i , is defined for a mixture of N species, as

$$Y_i \equiv \frac{m_i}{\sum_{i=1}^N m_i} \quad , \quad (2)$$

and

$$m_i = \text{mass of the } i^{\text{th}} \text{ species} \quad .$$

The adiabatic flame temperature rise ΔT_f for each ϕ was computed using the CHEMKIN chemical kinetics program (Kee *et al.* 1980). The four values of ϕ with the corresponding mass fractions and ΔT_f 's are given in the following table.

Table 1: Stoichiometric mixture ratios, mass fractions, and adiabatic flame temperature rises.			
ϕ	Y_{F_2}	Y_{NO}	ΔT_f (K)
7.0	0.0127	0.0029	7.2
10.0	0.0174	0.0028	6.9
14.0	0.0237	0.0027	6.9
17.9	0.0300	0.0027	6.7

The choice of ΔT_f was determined from several preliminary experiments. The lowest value of ΔT_f that could be measured accurately and with repeatability was sought to reduce both buoyancy effects and heat release effects on the flow dynamics. The choice of $\Delta T_f \approx 7 \text{ K}$, on the basis of buoyancy concerns, will be developed below.

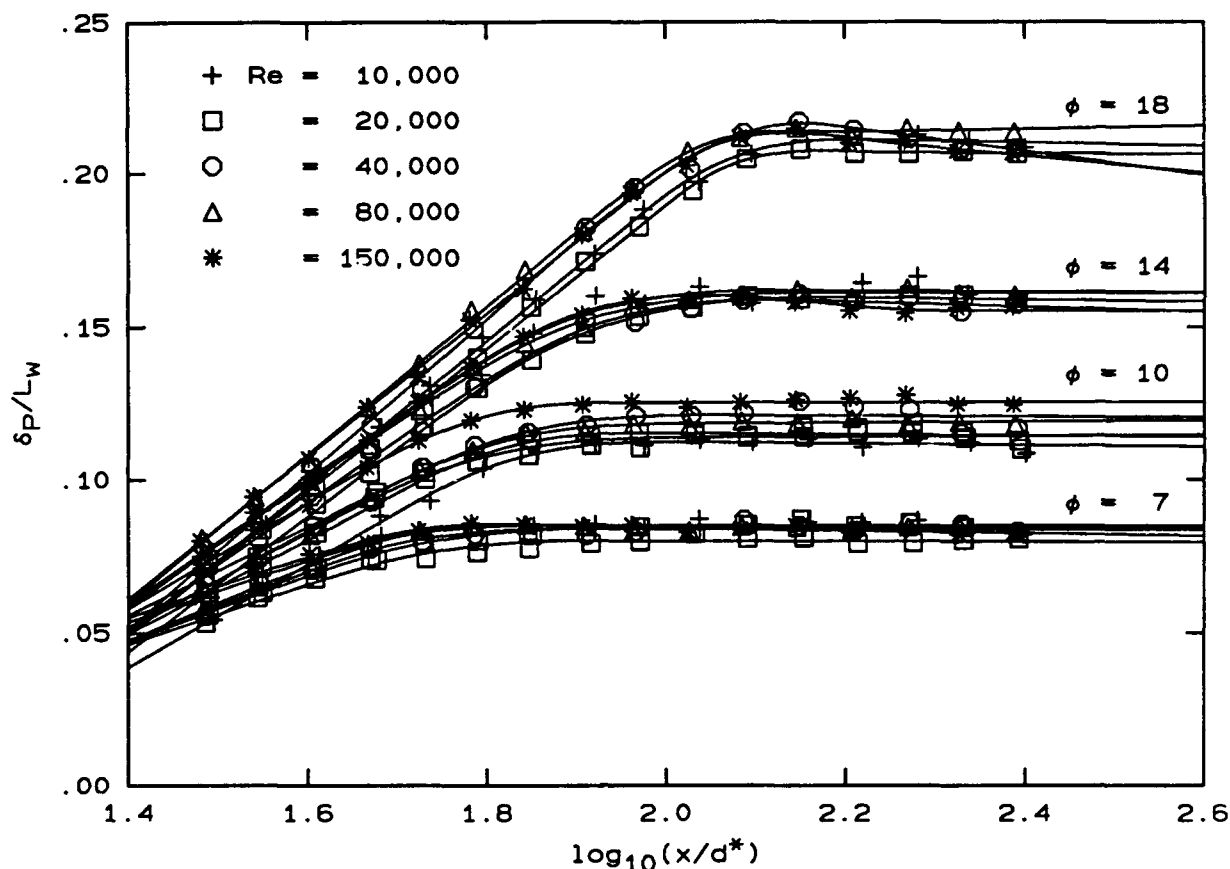
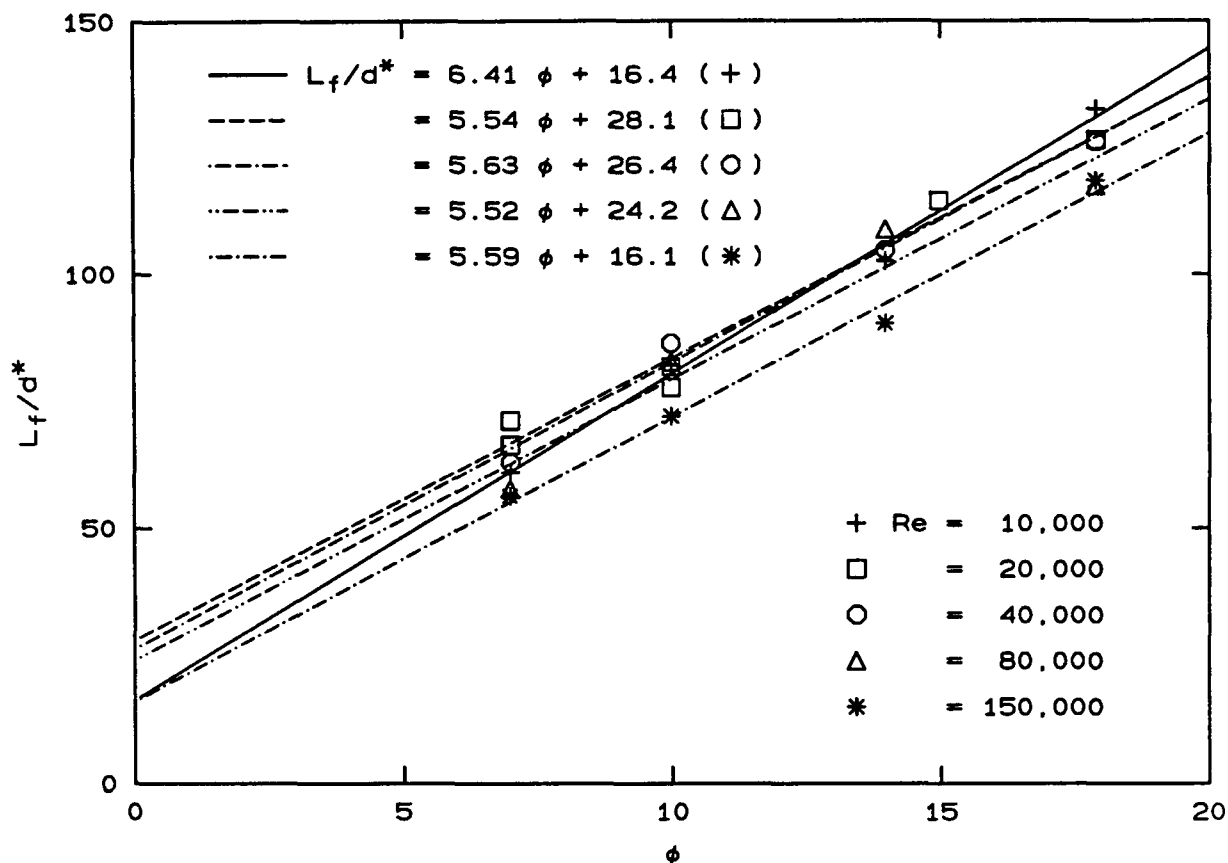


FIG.5 Normalized product thickness versus $\log_{10}(x/d^*)$ for the various ϕ 's.

Figure 5 shows the data for the $\phi = 7, 10, 14$, and 18 runs. The solid line is a compound curve fit with a linear least squares fit in the ramp region and a cubic spline fit to the knee region. The runs were fairly repeatable as shown by the good agreement of the repeated runs. All of the runs exhibit a linear ramp region when plotted in semi-logarithmic coordinates and a nearly constant asymptotic level after the knee or flame tip region. The average flame lengths were estimated from these curves by determining the 99% of maximum δ_P/L_w point. These flame lengths are plotted versus ϕ for the various Reynolds numbers in Fig. 6. The straight lines are linear least-squares fits to the data of the form

$$\frac{L_f}{d^*} = A\phi + B, \quad (3)$$

where A and B are functions of Re with A being the slope and B being defined as the "mixing virtual origin". This mixing virtual origin is a new observation and corresponds to the abscissa-intercept in Fig. 6, i.e., the flame length extrapolated to $\phi = 0$. If the flow could be described by its far-field behavior at the nozzle exit,

FIG. 6 Normalized flame length versus ϕ .

then B would be the flame length measured in the limit of $\phi \rightarrow 0$. The variation of B in Fig. 6 indicates that this mixing virtual origin systematically decreases with increasing Reynolds number for $Re \geq 2.0 \times 10^4$. Some of the variation in B could be attributable to the uncertainty in the curve fits used for the flame length determination. Another possibility could be a variation in x_0 , the virtual origin of the jet, with increasing Re . However, even combined, these effects are not large enough to explain such a large variation in B . A nonzero intercept in itself is not surprising, if one realizes that the potential core extends roughly six diameters from the nozzle exit and that the self-similar region of the jet typically begins around $x/d_0 = 20$ (e.g., Dowling & Dimotakis 1990). Therefore, fully-developed turbulent mixing on a molecular scale requires some distance downstream of the nozzle exit to develop, hence the streamwise delay in molecular mixing. The fact that B has such a large value and that it varies with Re , however, is a new observation.

3.1.2 Kinetics

The F_2/NO chemistry in this study can be described by the "effective" reaction:

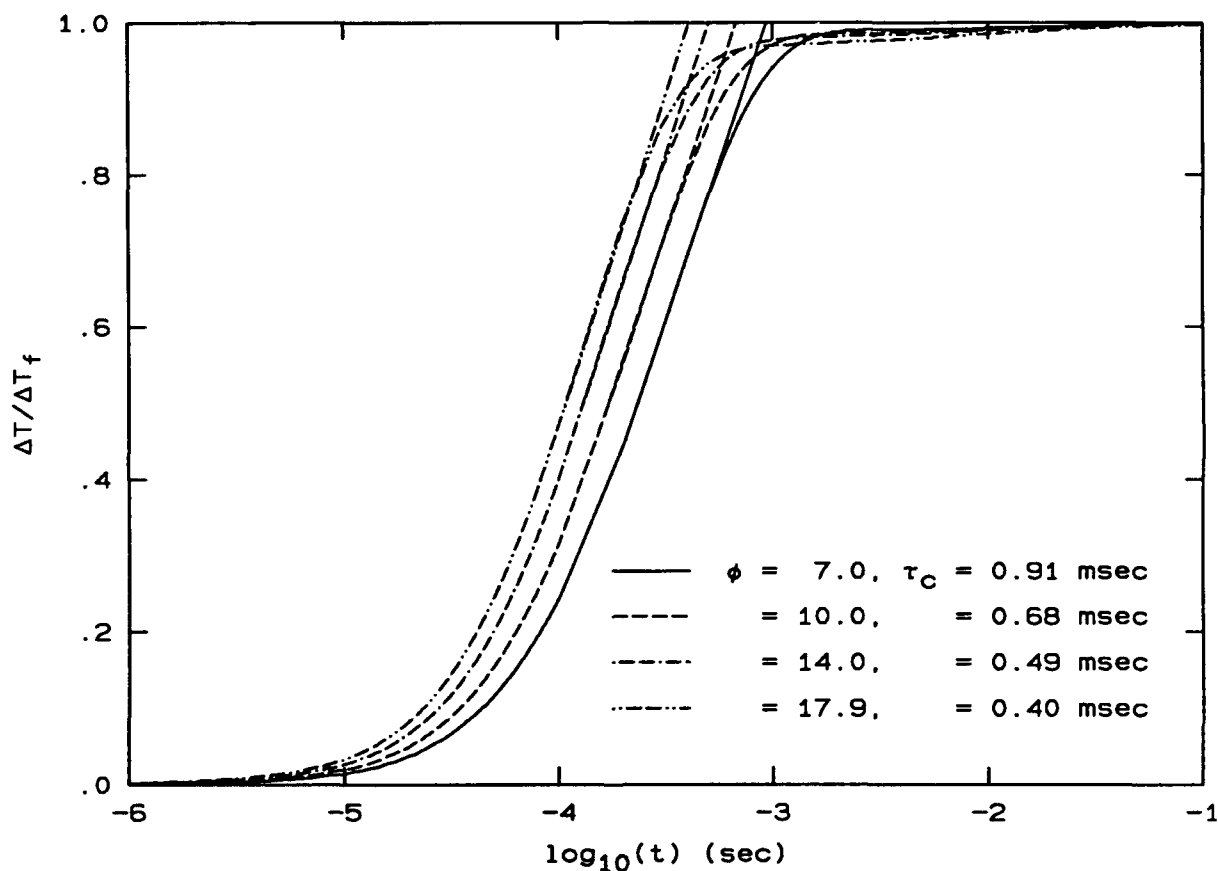
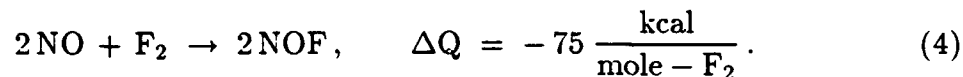


FIG. 7 Chemical reaction times for some of the runs described in Sec. 3.1.1, $p = 1$ atm, $T = 293$ K.

The reaction actually consists of two chain reactions of different rates and heat of reaction. To estimate the chemical reaction time τ_c , these reactions were investigated using the CHEMKIN chemical kinetics software package (Kee *et al.* 1980) with a constant-mass, constant-pressure reactor. Figure 7 shows a sample result from the program for the mass fractions corresponding to the four ϕ 's used in Sec. 3.1.1.

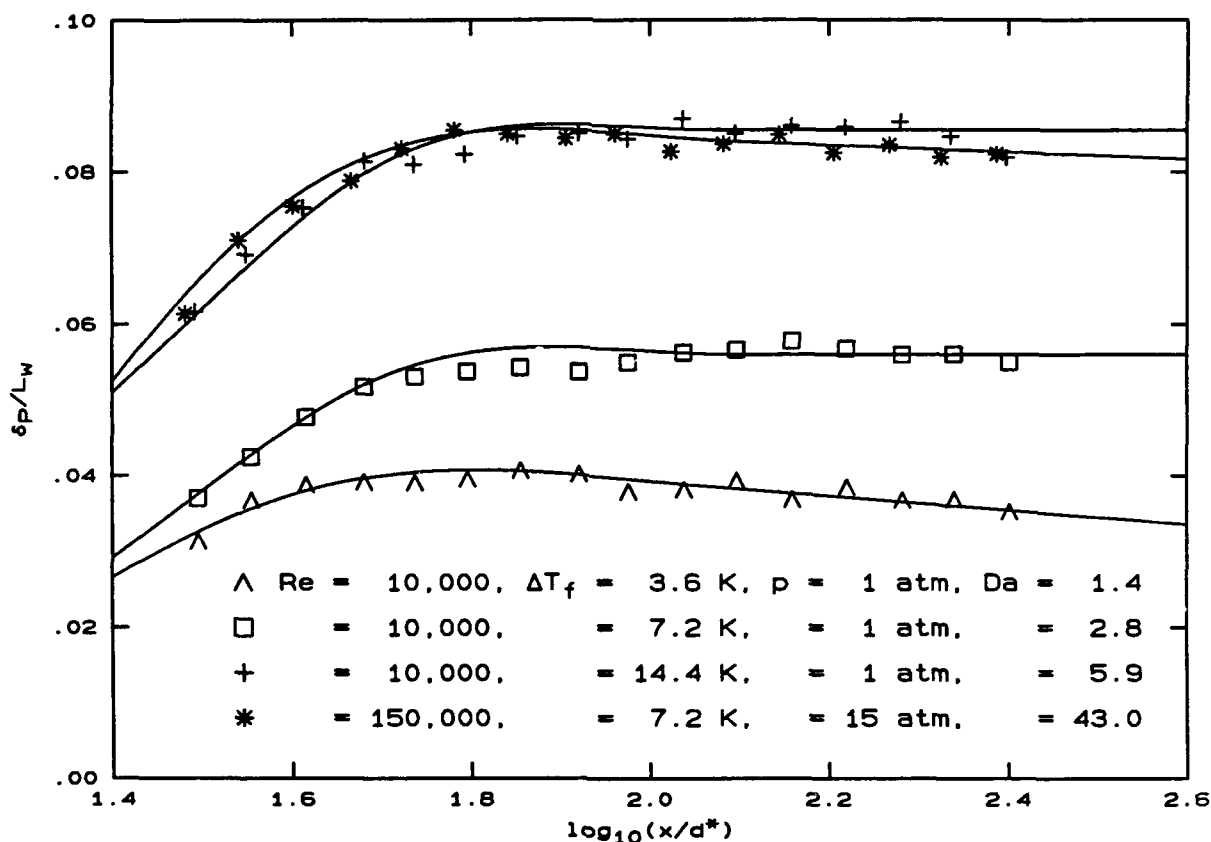


FIG. 8 Temperature doubling to check kinetic rate, $\phi = 7$, $U_0 = 62.4$ m/s. Damköhler number is given for $x/d^* = 30$.

The reaction time τ_c was determined by drawing a tangent to the curve at its steepest point and using the intersection of this tangent line with the adiabatic flame temperature as the chemical time. The slowest rate is for $\phi = 7$, $p = 1$ atm with $\tau_c = 0.91$ msec.

For these experiments, it was required that the time lag between molecular mixing and chemical product formation be negligible. In this mixing-limited condition, that we will designate as the fast chemistry regime, there is a one-to-one correspondence between molecular mixing and product formation. The ratio of the local large-scale passage time to the chemical reaction time is one way of estimating when the reacting flow is in the fast chemistry regime. This ratio of these two quantities is (one of) the Damköhler number(s), defined by

$$Da \equiv \frac{\tau_\delta}{\tau_c}, \quad (5)$$

where τ_δ is the local large-scale passage time, estimated by dividing the local jet diameter $\delta(x)$ by the mean centerline velocity U_{cl} , *i.e.*,

$$\tau_\delta = \frac{\delta(x)}{U_{cl}} \quad , \quad (6)$$

and τ_c is the chemical reaction time, computed as described above. The local jet diameter $\delta(x)$ for a turbulent jet has been measured by many experimenters (*e.g.*, White 1974, p. 509; Dowling 1988) and can be approximated by

$$\delta(x) \approx 0.44 x \quad . \quad (7)$$

An estimate of U_{cl} is given for a momentum-dominated, density-matched jet by Chen & Rodi (1980) as

$$\frac{U_{cl}}{U_0} = 6.2 \frac{d_0}{x - x_0} \quad . \quad (8)$$

The jet exit diameter d_0 in the formula above should actually be replaced by d^* , the momentum diameter of the jet, but for a properly designed nozzle with density-matched jet and reservoir gases, $d^* \approx d_0$. In the limit of fast chemistry, *i.e.*, $Da \gg 1$, chemical product formation tracks molecular mixing. The lowest Da of the runs in Sec. 3.1.1 occurs at $x/d^* = 30$ for the $\phi = 7$ run of Fig. 7, with a corresponding Damköhler number of $Da = 2.8$.

Since U_0 was held constant for the Reynolds number experiments described in Sec. 3.1.1, and the spreading rate of the jet is assumed to be constant (*i.e.*, Reynolds number independent), τ_δ for a given x/d^* is the same for all of the current experiments in Sec. 3.1.1. The chemical time τ_c decreases with reactant number density (*i.e.*, pressure). This means that, for the experiments described in Sec. 3.1.1, the numerator in Eq. 5 remains constant and the denominator is decreasing with increasing Reynolds number. Therefore, demonstrating fast chemistry for the lowest Reynolds number runs guarantees that the higher Reynolds number experiments of Sec. 3.1.1 are in the fast chemistry regime.

One way of determining if a run is in the fast chemistry regime is to repeat the experiment, doubling the reactant concentrations of both jet and reservoir fluids. This doubles the adiabatic flame temperature. The kinetic rate is proportional to reactant number density and also exponentially dependent on the reaction temperature. Therefore, a concentration doubling increases the kinetic rate through higher reactant concentrations and by increasing the reaction temperature. The temperature rise for the higher concentration run should double, if the chemical

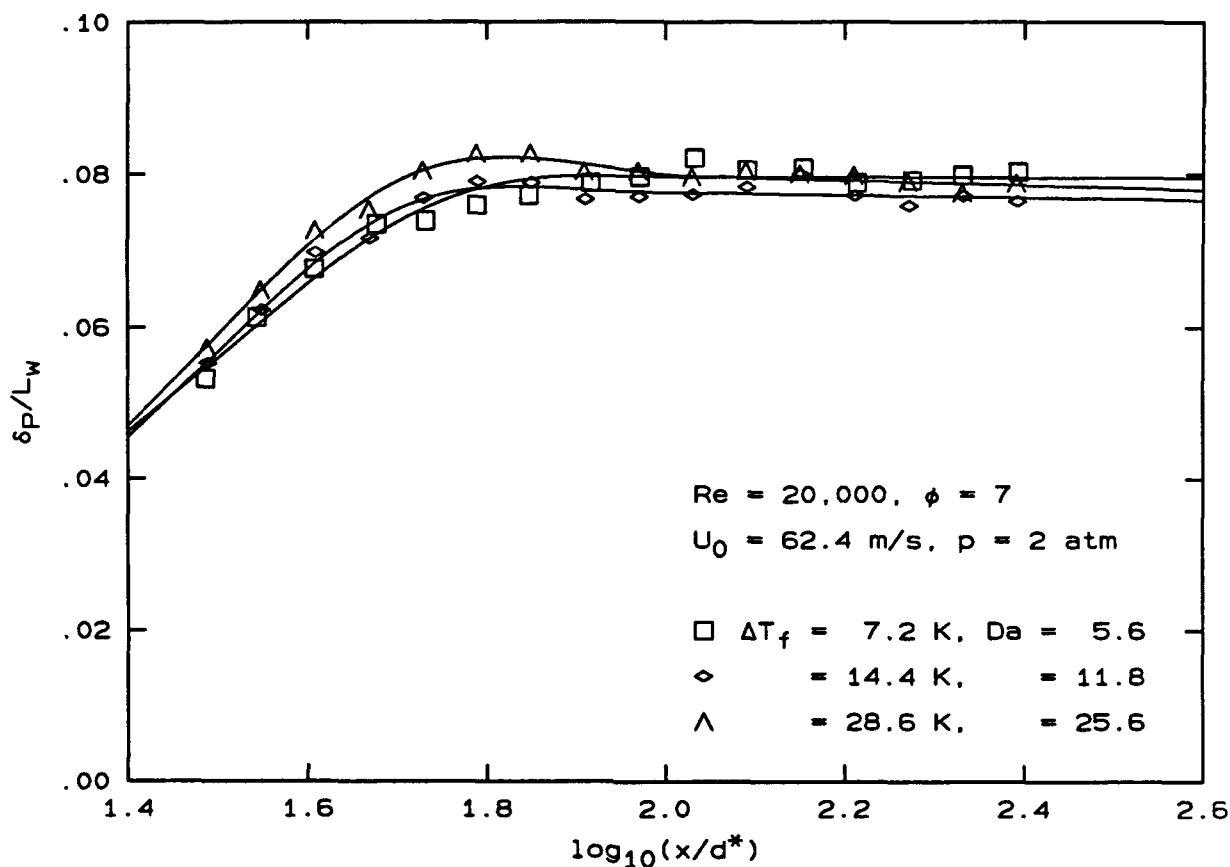


FIG. 9 Temperature doubling to check kinetic rate. Damköhler number is given for $x/d^* = 30$.

product formation is already mixing-limited. If the chemistry was not fast before the concentration doubling, the faster kinetic rate after the doubling should result in more than double the chemical product and, correspondingly, more than double the temperature rise.

A similar temperature doubling was performed for the run in Sec. 3.1.1 with the lowest Damköhler number, shown in Fig. 8. These data do not collapse. Slow chemistry should only affect the ramp region of the curve and possibly result in a longer flame length. The asymptotic level, however, should eventually agree at some downstream location because all of the F_2 should react if one goes far enough downstream. The asymptotic level does not agree for the various ΔT_f 's. The asymptotic level nearly doubles for each temperature doubling leading to the hypothesis that some of the F_2 was being depleted by passivation of the nozzle plenum screens and honeycomb during each run. At low concentrations, doubling

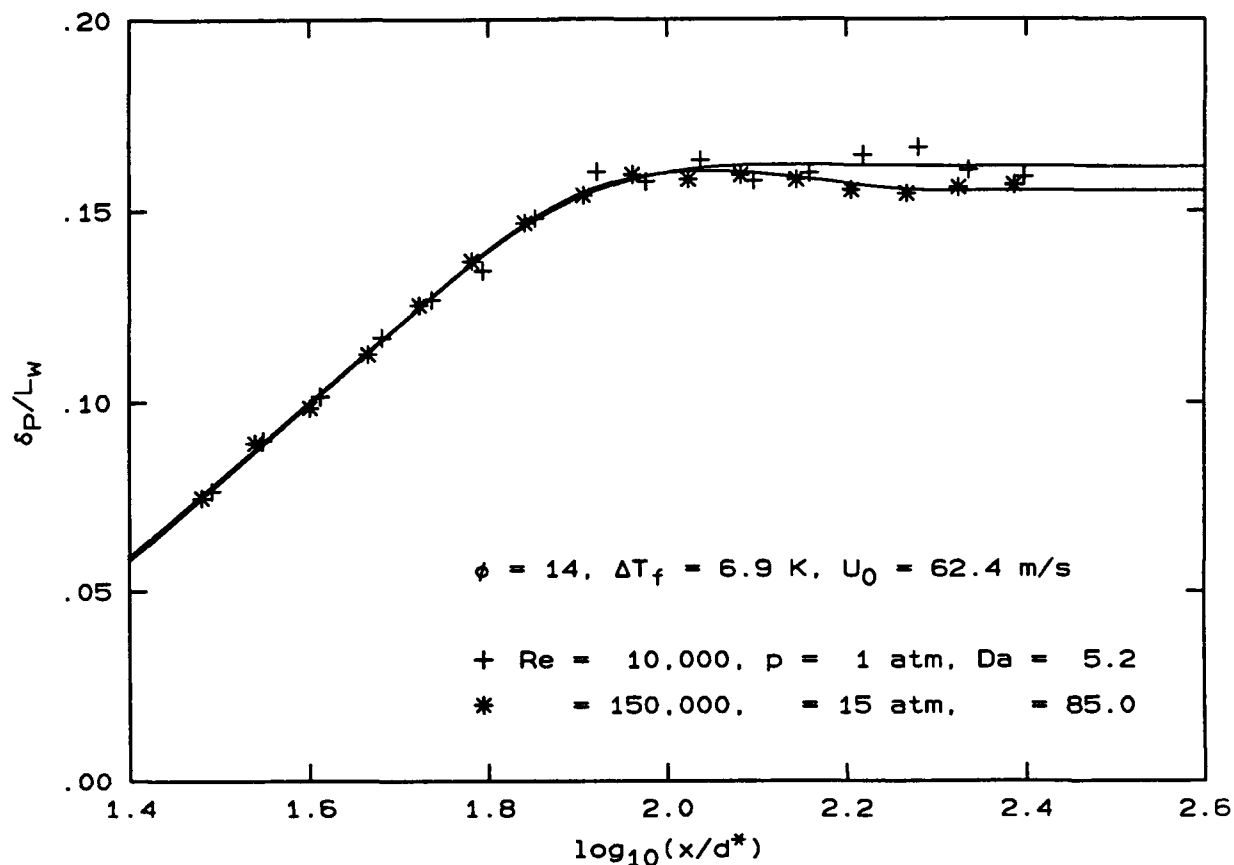


FIG. 10 Runs showing the lowest Damköhler number that still demonstrates fast chemistry. Da is given for $x/d^* = 30$.

the absolute number of moles of F_2 , by doubling the reactant concentrations, should reduce the passivation effect in half. This appears to be what is happening in Fig. 8, supporting the passivation hypothesis.

The kinetics and the passivation problems disappear for the run with $\Delta T_f = 14.4 \text{ K}$ in Fig. 8, as demonstrated by the collapse of the data with the higher Reynolds number run that should be in the fast chemistry regime.

Figure 9 shows the result of a similar experiment at $p = 2 \text{ atm}$ with two temperature doublings. The collapse is good and this condition appears to be in the fast chemistry regime with the $\Delta T_f = 7.2 \text{ K}$ run having a $Da = 5.6$.

Figure 10 compares the run at $p = 1 \text{ atm}$, $\phi = 14$, to the run at $p = 15 \text{ atm}$ and the same ϕ and flame temperature. This is the lowest value of the Damköhler

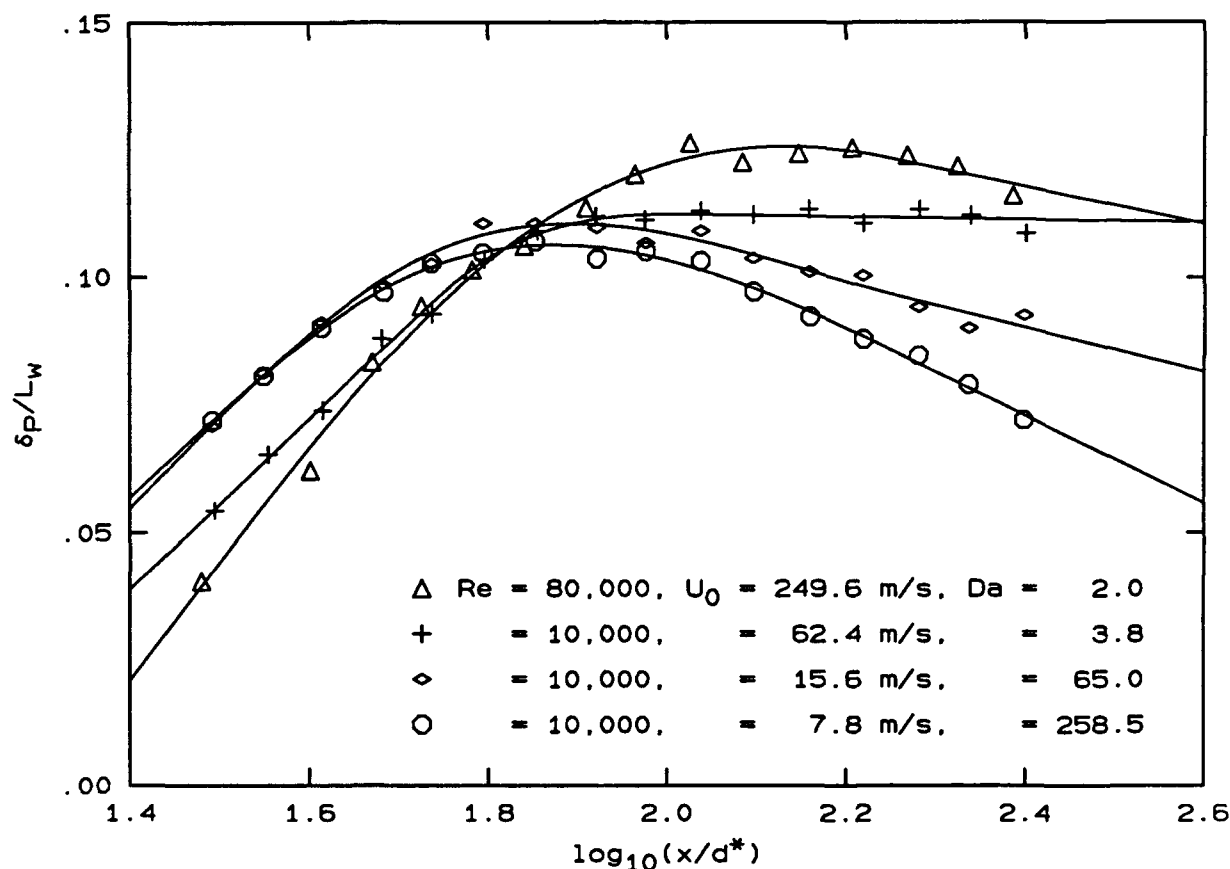


FIG. 11 Runs showing effects of slow chemistry in the ramp region, $\phi = 10$, $\Delta T_f = 6.9$ K. Damköhler number given for $x/d^* = 30$.

number in all of the experiments which still collapses well with an experiment at a much larger Damköhler number. The lower limit of Damköhler number in these experiments, in which the flow can be considered to be in the fast chemistry regime, is therefore $Da \simeq 5.2$.

In the runs described thus far, the Damköhler number was changed by varying the chemical time, but changing the large-scale passage time τ_δ is another way of varying Da . Several runs at different velocities and pressures were performed in which the Damköhler number was low but the temperature measurement beyond the flame tip achieved the correct level, showing them to be free of passivation problems. Figure 11 shows runs at various velocities and Damköhler numbers. The temperatures for the slow chemistry conditions lag behind the fast chemistry runs but eventually achieve the same level beyond the flame tip. This is how slow chemistry was expected to manifest itself. The Damköhler numbers are consistent

with the limiting value of $Da \simeq 5.2$ discussed above. The lower velocity runs show the effects of buoyancy beyond the flame tip. The high-velocity run is repeatable.

3.1.3 Buoyancy Effects

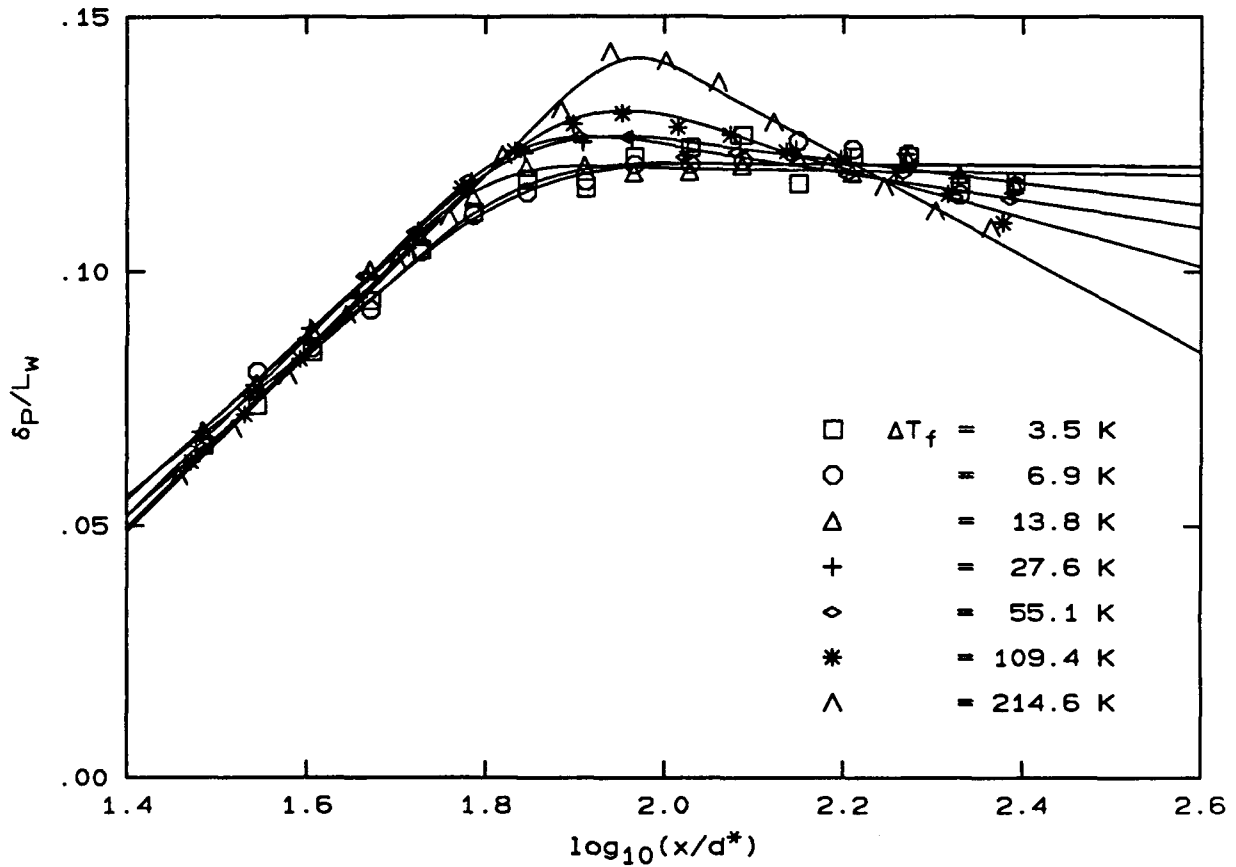


FIG. 12 Normalized product thickness versus $\log_{10}(x/d^*)$ for several adiabatic flame temperatures, $Re = 4.0 \times 10^4$, $\phi = 10$, $U_0 = 62.4$ m/s, $p = 4$ atm.

Buoyancy is an issue that was explicitly addressed in these experiments. The positively buoyant jet (*i.e.*, a jet in which the momentum flux increases with x) entrains at a higher rate than the momentum-dominated jet (*e.g.*, Becker & Yamazaki 1978). Therefore, the similarity law that results in a constant average temperature measurement beyond the flame tip will change.

The temperature excess beyond the flame tip is a conserved scalar obeying the similarity law for a momentum-dominated jet. Therefore, the average temperature measurement will decay beyond the flame tip at some point when buoyancy forces become comparable to the jet source momentum flux.

For the experiments described above, ΔT_f was chosen by the requirement that the jet remain momentum-dominated up to the last measuring station at $x/d_0 = 240$ for the ϕ 's investigated. This was done by performing a set of preliminary experiments at several ϕ 's. The longest flame length occurs at $\phi = 17.9$. This case was examined by systematically increasing ΔT_f until the temperature measurement beyond the flame tip was no longer constant, but was observed to decrease. As expected, the longest flame length is the most sensitive to buoyancy effects from temperature.

Figure 12 shows a set of experiments spanning adiabatic flame temperatures ΔT_f from 3.5 K to 215 K. A Reynolds number of 4.0×10^4 , was chosen for this scan. A ϕ of 10 placed the flame tip in the center of the $\log_{10}(x/d_0)$ range, giving an equal number of points on each side of the knee. The temperature measurements beyond the flame tip reach a constant value for the low heat release runs, indicating that they are momentum-dominated. As the flame temperature increases, however, the temperature measurements no longer attain a constant level but begin to decrease with increasing x/d^* , as shown in Fig. 12, for $\Delta T_f = 27.6$ K.

These data are presented here as a first effort to ascertain that the Reynolds number study was conducted in the momentum-dominated flow regime. This series of experiments showed an enhancement to molecular mixing under the influence of buoyancy. This enhancement depends on the relative effect of buoyancy to momentum forces. Further study of this behavior is currently in progress, as this effect plays an important role in the context of flow and mixing control.

3.2 Liquid-phase turbulent jet mixing

During the past year, a thesis investigating the fine scale turbulent structure in a high Schmidt number (liquid phase) jet was completed (Miller 1991). Close to one hundred copies have been distributed to people throughout the world. Limited numbers are still available upon request. An additional publication related to this work appeared in *Physics of Fluids A* (Miller & Dimotakis 1991b) during the reporting period (Appendix A of this report), and a third has been submitted for publication (Miller & Dimotakis 1992). Seminars, lectures, and talks highlighting specific aspects of this work have been given by Paul Miller and Paul Dimotakis at ASU, Caltech, U. Chicago, UCSD, USC, at the Institute of Advanced Studies in Princeton, the DLR and Max Planck Institute (Göttingen, Germany), LLNL, the Sandia STAR meeting, and the November 1991 meeting of the APS Division of Fluid Dynamics.

Results to date include an analysis of scalar interfaces for fractal properties (which differed substantially from previous reports in the literature), evidence of Taylor scales in the turbulent jet, and the absence of a k^{-1} region in the small scale region of this high Schmidt number flow — all of which have been discussed in previous reports. Important new observations concerning the applicability of fractal power-law ideas to turbulence have grown out of our work in that area, and a paper discussing the issue is included as Appendix C. This paper, in conjunction with Miller & Dimotakis (1991a), has changed how fractals are viewed in the Fluid Dynamics community.

Additional findings during this report period include additional new evidence that the jet pdf's, variance, and spectra *vary with Reynolds number*, and that these changes with Re are also Schmidt number dependent. The long-time statistics of the jet concentration field were found to converge very slowly, scalar spectra were found *not* to obey the classical $k^{-5/3}$ power-law prediction, a log-normal behavior was discovered at small scales in the power spectra (with a starting point which scales like $Re^{3/4}$), and initial conditions in the jet plenum and near the nozzle were seen to influence the flow's mixing behavior *in the far-field*.

In the following sections, we will describe some of these new findings in greater detail. For topics not covered here and for a more complete documentation, the reader is directed to Dimotakis & Miller (1990), Miller (1991), as well as Miller & Dimotakis (1991a,b and 1992).

3.2.1 Reynolds and Schmidt number effects

An important result from these experiments is that the jet concentration field changes with Reynolds number. Reynolds number for these jets is defined as

$$Re \equiv \frac{u_0 d}{\nu}, \quad (9)$$

where u_0 is the jet exit velocity, d is the jet nozzle exit diameter, and ν is the kinematic viscosity of the fluid (water), and was varied in these experiments by altering u_0 . The jet concentration was measured on the centerline, and the probability density functions, or pdf's, were accumulated. The current results from the high Schmidt number jet, for a wide range of Re , are displayed in Fig. 13, along with data from gas-phase jets (Dowling 1988).

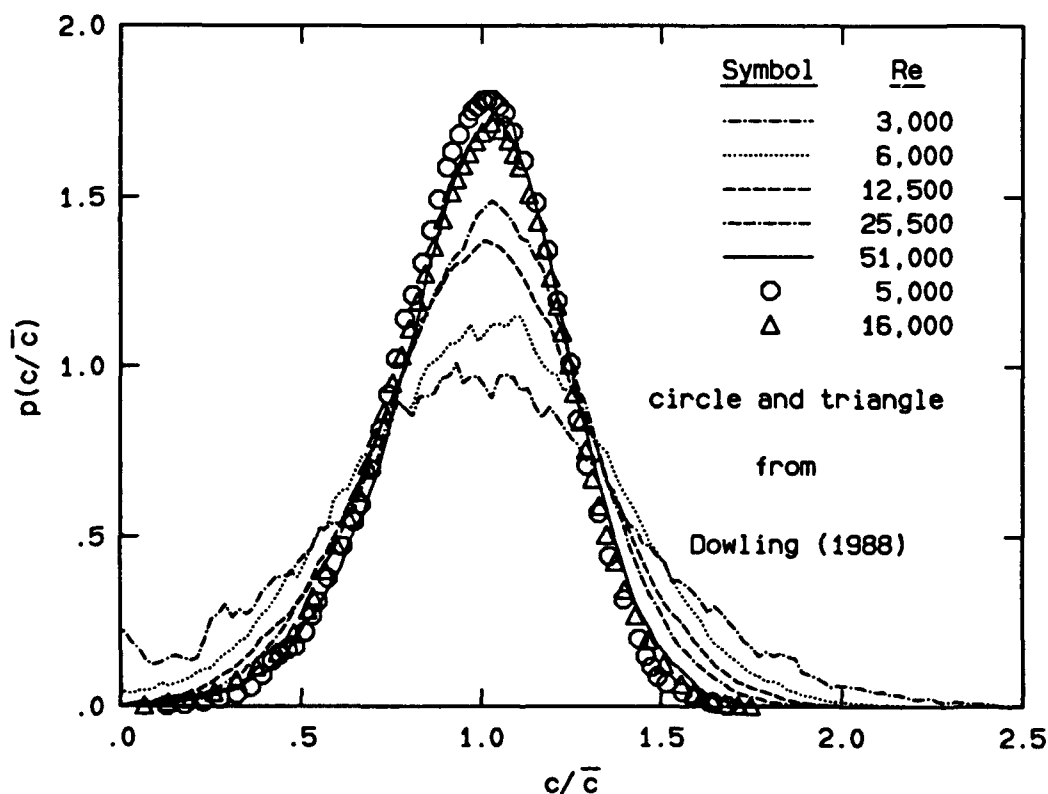


FIG. 13 Comparison of current pdf's with gas-phase results from Dowling (1988).

As is apparent in Fig. 13, the high Schmidt number pdf's become taller and narrower with increasing Re , while the gas-phase pdf's vary little. It should be noted that a narrower pdf implies a mixture with a more uniform concentration.

i.e., more homogeneous or well-mixed. Therefore, we conclude that the behavior of the pdf's in Fig. 13 suggests that the liquid-phase jet is less well mixed than the gas-phase jet, but that this difference decreases with increasing Re . Alternatively, the gas-phase composition is relatively insensitive to Re , while the liquid-phase jet becomes better mixed with increasing Re .

Another, related, measure of the mixedness of the jet is the scalar, or concentration, variance defined as

$$\text{var}\{c\} = \overline{c'^2} \equiv \int_0^{c_{\max}} (c - \bar{c})^2 p(c) dc, \quad (10)$$

(*cf.* Miller & Dimotakis 1991b), where c_{\max} is the highest concentration present and $p(c)$ is the probability density function of the jet fluid concentration c , normalized such that

$$\int_0^{c_{\max}} p(c) dc = 1. \quad (11)$$

The variance is typically nondimensionalized by the mean squared, \bar{c}^2 . The resulting quantity is a measure of the width of the distribution $p(c/\bar{c})$, *i.e.*, pdf's such as in Fig. 13. Just as a narrower pdf indicates a better mixed jet, smaller variance values imply more uniform composition, with a perfectly homogeneous, constant concentration having a variance of zero. The concentration variance was calculated from the jet concentration data over a range of Reynolds numbers. The results are compared with the gas-phase results in Fig. 14.

The high Schmidt number points are fit with a function chosen for its simplicity, ability to approximate the observed behavior, and capability to either approach a nonzero asymptotic value (or zero, if it were indicated). The fit does suggest that the points are approaching a constant value with increasing Reynolds number, and the determined asymptote, 0.039, is in good agreement with the finding from the analysis of previous data of 0.04 (Miller & Dimotakis 1991b), as discussed further in Miller (1991).

The observed decrease of the concentration variance (or, equivalently, the rms) in the high Schmidt number jet is a substantial effect. The jet becomes better mixed, apparently approaching an asymptotic, high Reynolds number value of the variance and a similarity in the concentration pdf's. *In a span of 1.5 decades in Reynolds number, the variance is reduced by over 70%.* The decline is not from deteriorating resolution, as discussed both in Miller & Dimotakis (1991b) and Miller (1991).

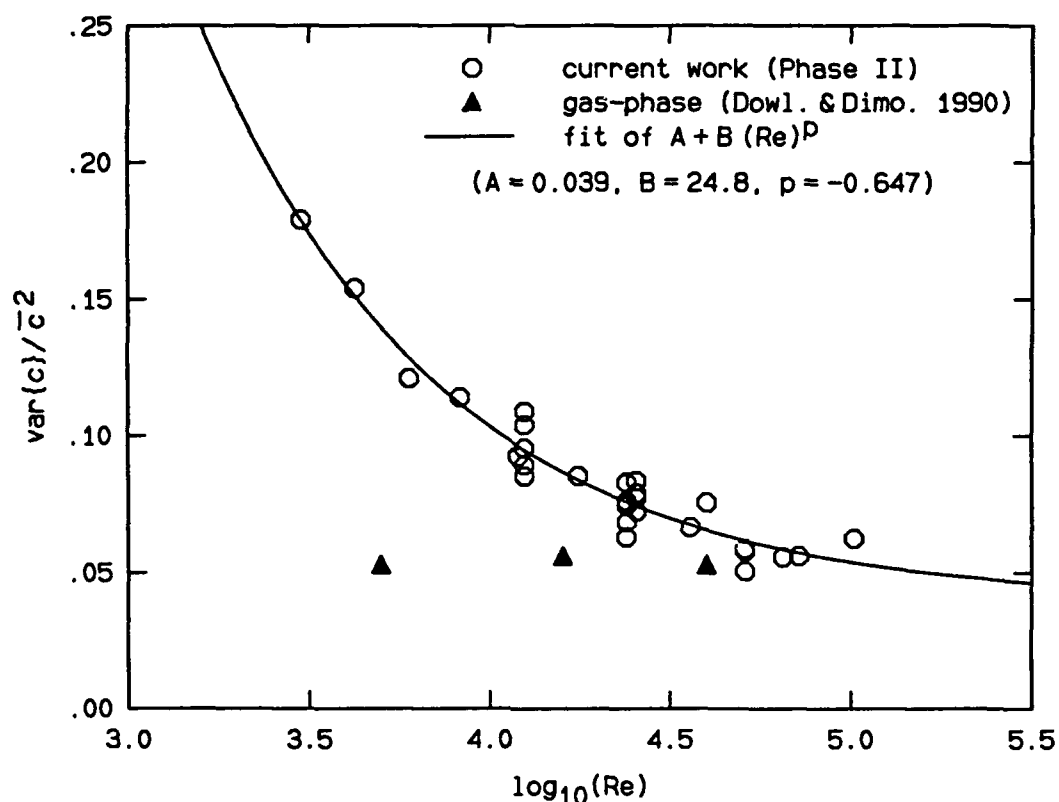


FIG. 14 Comparison of variance values with gas-phase results of Dowling & Dimotakis (1990).

Like the pdf's, the gas-phase variances measured by Dowling (1988) change little over the range of Reynolds numbers investigated, indicating a fundamental difference between the order unity Schmidt number (gas-phase) and the high Schmidt number (liquid-phase) jet mixing. This difference is also reflected in the behavior of the corresponding power spectra for the two cases. Figure 15 displays selected concentration power spectra from the current work, with the results of Dowling (1988) for comparison.

The high Sc spectra have a considerably greater extent than the order unity Sc spectra at the high frequencies. This behavior is expected in view of a species diffusion scale that is smaller than the viscous diffusion scale, which provides an additional length scale in the flow (as noted by Batchelor 1959). While no constant -1 spectral slope is present, as discussed in previous reports, a log-normal range is observed at frequencies higher than the viscous scale, suggesting that the particular assumptions of Batchelor's theory which lead to the -1 slope require reexamination (*cf.* Dimotakis & Miller 1990). These findings were presented at the 1991 meeting

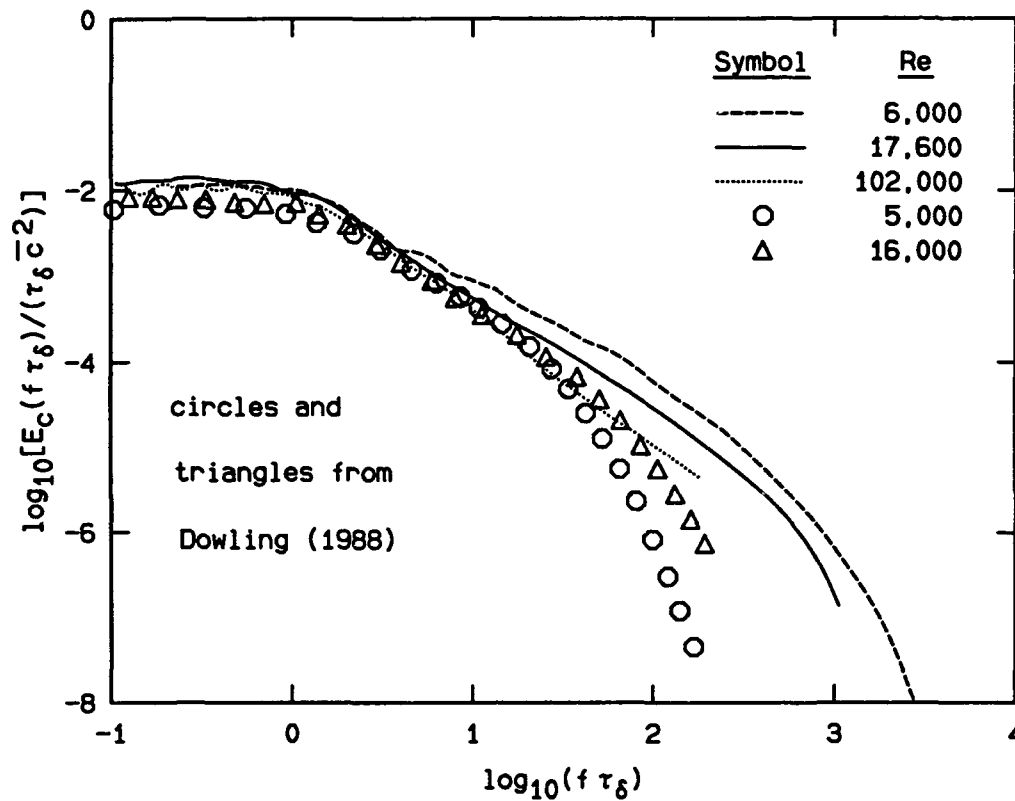


FIG. 15 Comparison of power spectra with gas-phase results from Dowling (1988).

of the APS Division of Fluid Dynamics, and are addressed at greater length in a recently submitted paper (Miller & Dimotakis 1992).

In addition to the greater extent of the high frequency portion of the high Sc spectra, it is also noted that the power spectral densities are slightly larger than the gas-phase values, over the entire range of frequencies. A possible factor in this difference is that Dowling's jet nozzle was externally contoured, and a mild co-flow was provided to satisfy the entrainment requirements of the (enclosed) jet. There was no co-flow in the current work. If the effect of the co-flow was to reduce fluctuations near the nozzle, and consequently throughout the jet (in light of findings described below), it may have resulted in the broadly lower spectral densities.

3.2.2 Effects of initial conditions

It became apparent, during the course of the experiments discussed above, that something was influencing the behavior of the scalar variance. The cause was determined to be the fluid disturbance levels in both the jet plenum and beneath the nozzle exit. Additional runs were conducted specifically to address this issue. One type of run made was termed a "quick run," in which the jet plenum was filled rapidly and the run started within a minute. Eliminating the usual half-hour period wait for the plenum fluid to settle resulted in a substantially higher level of fluid motion, or disturbances, within the plenum during the run. A cruciform originally inside the plenum to damp such fluid disturbances was removed, except for one comparison run. Along with the "quick runs," other "quiet runs" were made in which the plenum fluid was left to settle for over half an hour, allowing the fluid disturbances to decay. Finally, one "quiet run" was made in which the tank fluid immediately beneath the nozzle was given a vigorous stir with a hand, just before initiating the run. This is the "extra disturbance" run shown in Fig. 16, along with the other results.

It can be seen in Fig. 16 that, within some scatter of the results, the quick runs have higher variance values than their corresponding quiet runs. The extra disturbance case also has a higher variance, while the run with the cruciform in place has a low variance which agrees well with a fit (dashed line) to the data previously displayed in Fig. 14. These quantitative measures of the effect of qualitatively different disturbance levels lead us to conclude that the jet variance *increases with increasing disturbance level*, both in the plenum and in the vicinity of the nozzle exit.

This is a somewhat surprising finding. It says that adding perturbations (in the form of disturbances) to the jet conditions causes the variance to *increase*, *i.e.*, making the jet *less* well mixed. It raises the possibility that the natural, undisturbed turbulent jet may provide the most "efficient" mixing. These results are for the liquid-phase (high Schmidt number) jet, and should be viewed in light of the earlier discussion of Sc effects. At this point, the corresponding gas-phase behavior has not been examined.

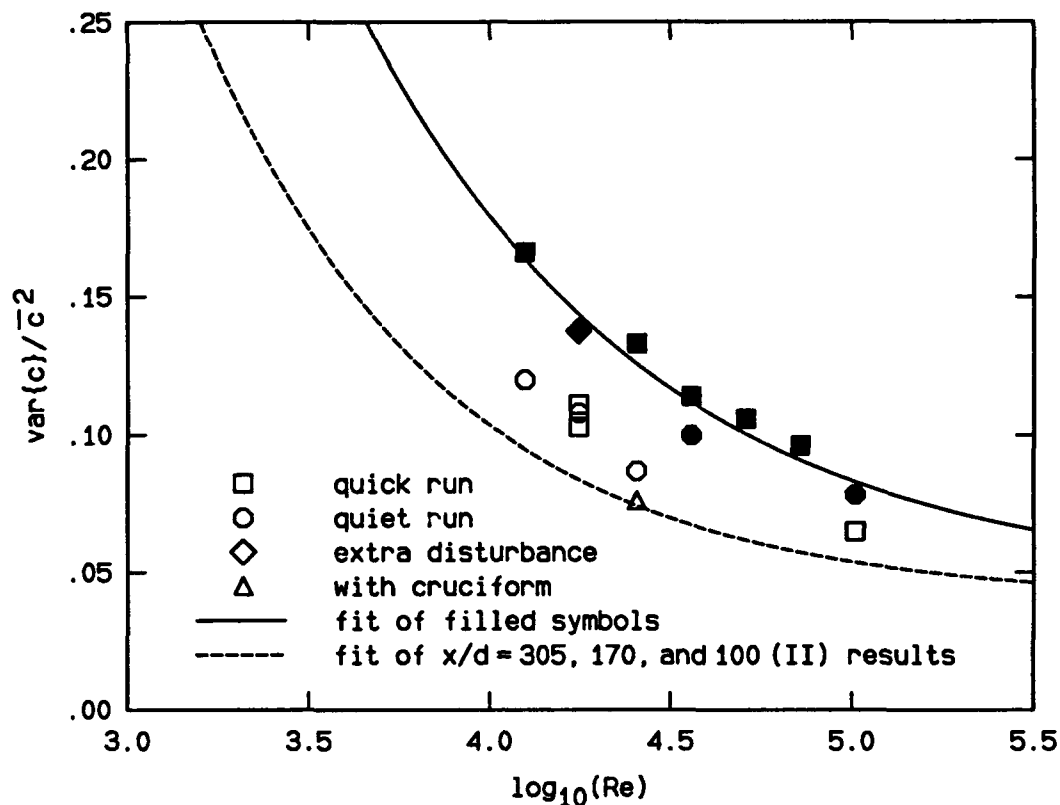


FIG. 16 Measured variance values for the $x/d = 295$ runs. The *shapes* of the symbols designate the run conditions. Additionally, the filled symbols were selected as representative of an upper bound of the measured values, and fit with an expression of the form $A + B Re^p$. Parameter values determined from the fit are: $A = 0.045$, $B = 19.6$, and $p = -0.54$.

3.2.3 Effects of plenum/nozzle geometry

A second factor, the plenum/nozzle geometry, was also found to affect the resulting scalar variance values in the high Schmidt number turbulent jet. Earlier experiments, described in Miller & Dimotakis (1991b) and referred to in Miller (1991) as "Phase I data," also displayed a decrease in the jet scalar variance as seen in Fig. 14, but had smaller values and approached their asymptotic behavior sooner (at a lower Reynolds number). The Phase I data are displayed in Fig. 17 as inverted triangles. They appear to lie on a distinct "branch", apart from the other data.

We attribute the difference in behavior seen in Fig. 17 to the only parameters that were changed between the two cases: the plenum/nozzle geometry. The Phase I experiments utilized a smaller diameter plenum assembly than the following (Phase II) experiments, although the nozzle exit diameter was the same. Therefore,

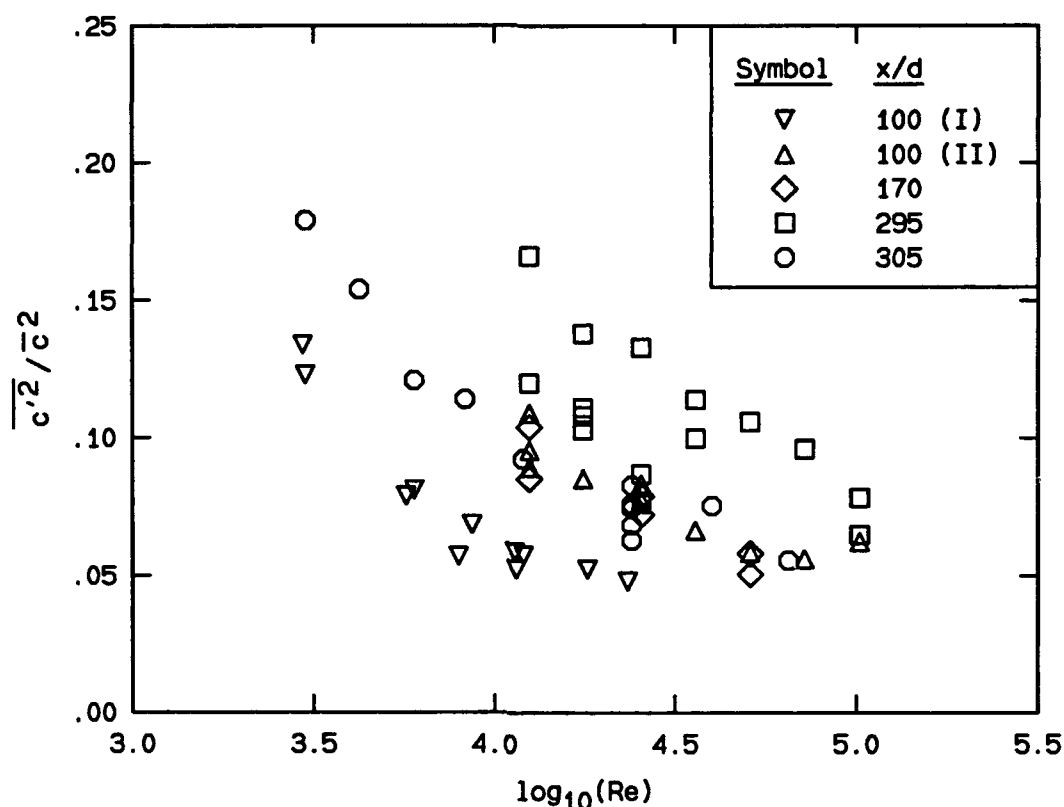


FIG. 17 Measured variance values for three major types of runs. The inverted triangles represent a different plenum/nozzle geometry. The squares are the data displayed in Fig. 16. The other symbols are the data shown in Fig. 14.

the contraction ratios were quite different, with Phase I being smaller. In addition, the details of the nozzle geometries differed between the two cases. The Phase I nozzle consisted of a smooth radius at the inlet and a short length of 0.254 cm (0.1 in.) I.D. tubing extending 1.8 cm (0.7 in.) beyond the plenum endplate. The tubing extension was tapered on the outside to provide a thin edge at the nozzle exit. The Phase II nozzle consisted of a circular contour leading to the exit plane of the nozzle plate, with a $\sim 3^\circ$ converging angle at the exit. With no extension tube, the nozzle exit was flush with the surface of the lucite nozzle plate. Photographs of the plenum/nozzle assemblies may be found in Miller (1991).

The conclusion from these results is that the jet plenum/nozzle geometry affects the mixing occurring in these turbulent jets, as demonstrated by the changes in the jet scalar variance. At this time, we have not isolated which particular aspects of the differences between the geometries were responsible for this behavior. However, considering the above discussion of the influence of disturbances, both the change in

contraction ratios and the variations in the nozzles are consistent with that effect. The contraction ratio serves to amplify disturbances in the plenum fluid as it passes into the nozzle. Therefore, it might be expected that a larger contraction ratio would exhibit a larger variance, which was indeed the case.

The small extension on the Phase I nozzle, in contrast to the flush-mounted hole of the Phase II nozzle, permitted a different (entrained) flow in the vicinity of the nozzle exit. Such a flow could be more stable to small disturbances in the vicinity of the nozzle exit. Recalling that introducing a disturbance beneath the nozzle exit increased the variance (Fig. 16), it is likely that the Phase I nozzle is less sensitive to disturbances, and, therefore, yields a lower variance. This is also consistent with the observed behavior.

3.3 Joint Caltech-Sandia National Laboratories modeling effort

As has been described in previous reports and papers, the Two-Stage Lagrangian model, under further development in collaboration with Sandia, has correctly predicted the influence of the several parameters that control combustion generated NO_x . The absolute level of the predicted emission index, however, has been too high by as much as an order of magnitude. The source of the error has now been identified.

The model, in essence, is a description of the nature and rate of molecular mixing, with the rate determined from scaling arguments and constants taken from experiment. In the past, the mixing rate, because of the lack of other data, was inferred from the dependence of the flame length on the stoichiometric ratio. Fixing the scaling law constants by this procedure obviously leads to the correct dependence of the flame length on the various parameters, but since this length is determined by the last element of nozzle fluid, to reach the stoichiometric ratio, the absolute value of the mixing rate so determined is much too low. Since the NO_x emission index depends critically upon residence time which in turn depends inversely on the mixing rate, it is now clear that a low rate yields too high an index.

What is instead the slowest rate (which determines the flame length) is a mean rate. For a cold jet, the data from Dowling & Dimotakis (1990) provide the necessary information. For reacting jets, the temperature profiles measured by Becker & Yamazaki (1978), combined with an energy conservation analysis, yield the required rate.

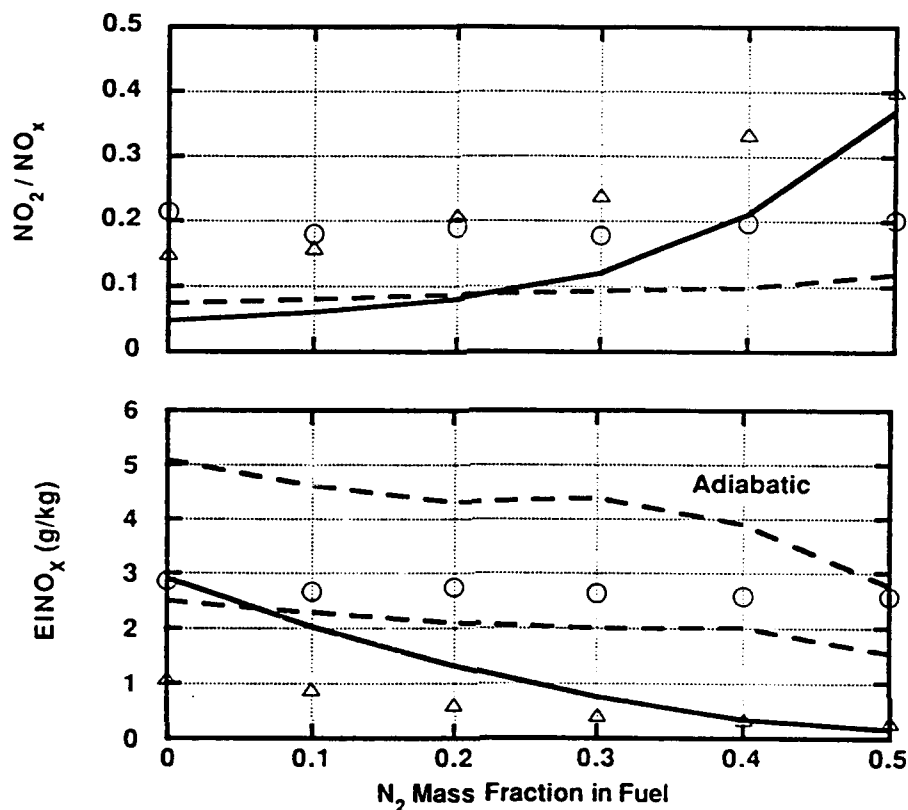


FIG. 18 Variation of NO_x emissions indices and molar NO_2/NO_x ratios with N_2 dilution of the fuel. Solid curves and triangles denote CO/H_2 flames; dashed curves and circles denote CH_4 flames. Radiant fractions for the undiluted CO/H_2 and CH_4 flames are 0.04 and 0.115 respectively, decreasing to 0.018 and 0.084 at the maximum dilution.

A. E. Lutz, Sandia, has used the new entrainment constant to compute the NO and NO_2 emission values, as well as other flame quantities, for the nitrogen diluted $CO - H_2$ and the CH_4 flames of S. R. Turns, Pennsylvania State. The model and experimental NO_x results are in good agreement and a joint paper is in preparation. Figs. 18, 19 and 20 and the following *verbatim* discussion are taken from this paper.

Figure 18 shows measurements and model predictions of NO_x emission indices ($EINO_x$). For the CO/H_2 flames, $EINO_x$ decreases with dilution as a result of both lower temperatures and shorter residence times. The influence of the radiant

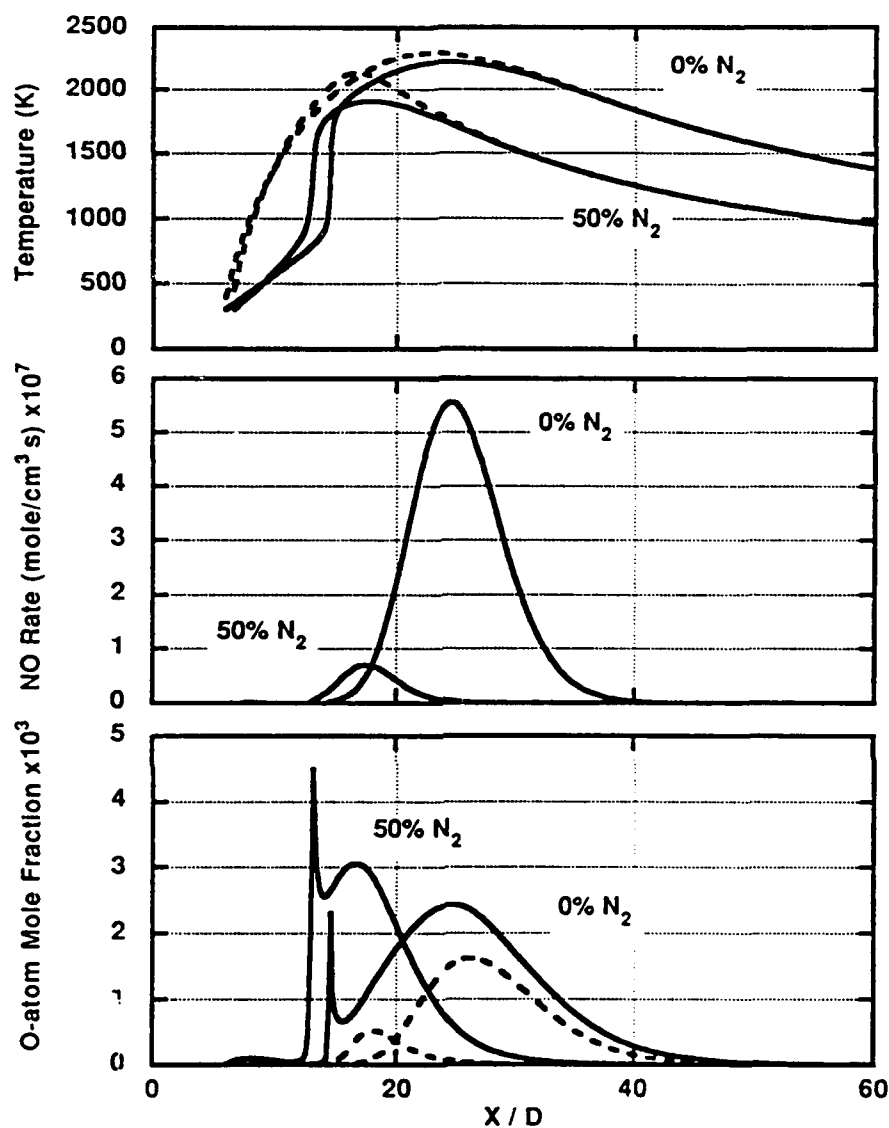


FIG. 19 Solutions for temperature, NO production rate, and O atom concentration, *vs.* axial location illustrating chemical effects on NO production rates in CO/H₂ flames. Dashed lines: equilibrium solutions for instantaneous (local) mixture fractions. The superequilibrium O atom fraction is larger in the diluted flame, because the residence time is a factor of two smaller.

energy loss is small in these flames. In contrast, radiant losses are important in the CH₄ flames, as witnessed by the adiabatic NO_x predictions being twice the non

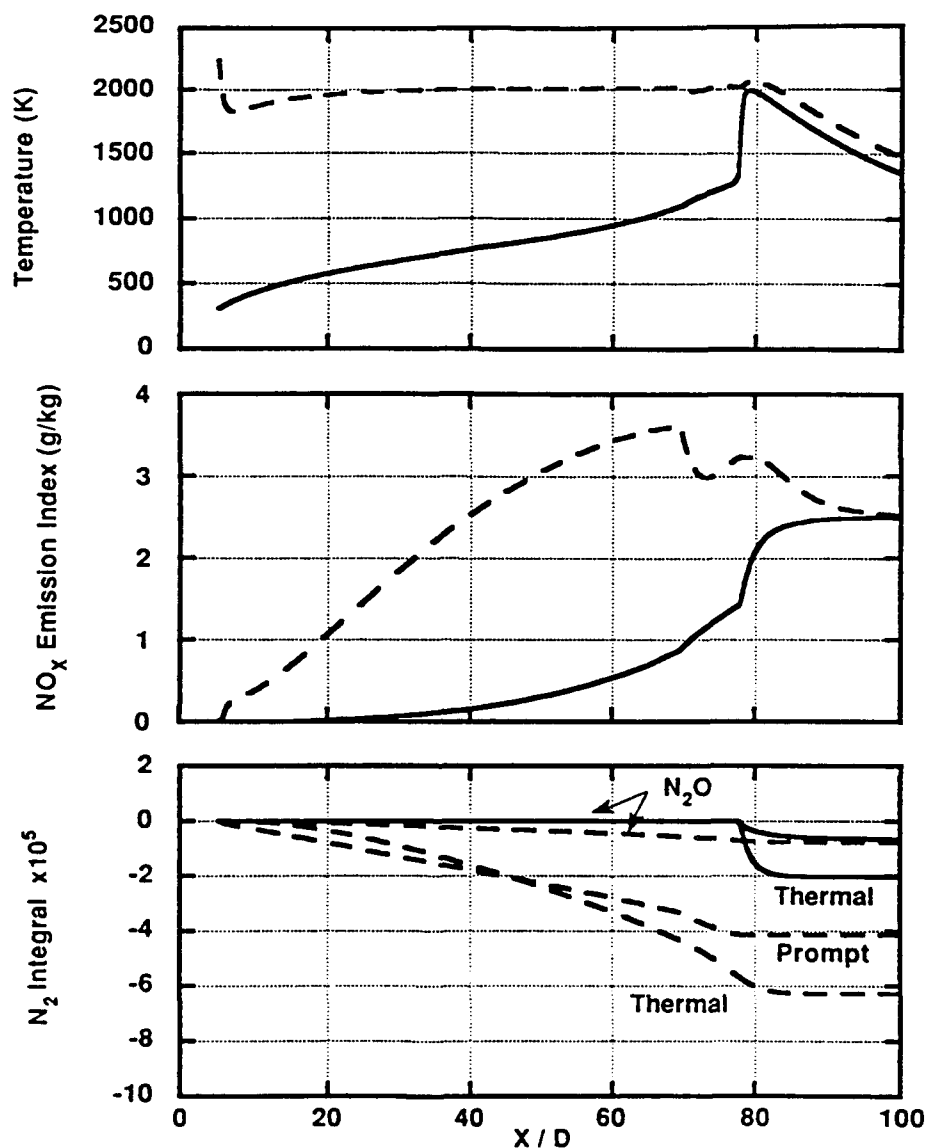
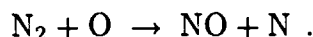


FIG. 20 Solutions for the temperature, NO_x emission index, and integrated N_2 production vs. axial location in the undiluted CH_4 flame. Solid curves: homogeneous reactor. Dashed curves: flame-sheet reactor. The integral is weighted by the relative mass in the reactors, by $\int (\dot{w}/\rho\bar{u})(m_i/m)dx$. \dot{w} is the mass of N_2O produced per unit volume in the i^{th} reactor. \bar{u} is the average velocity. The reactions are: Thermal, $\text{N}_2 + \text{O} \rightarrow \text{NO} + \text{N}$; prompt, $\text{N}_2 + \text{CH} \rightarrow \text{HCN} + \text{N}$; and the N_2O route, $\text{N}_2 + \text{O} + \text{M} \rightarrow \text{N}_2\text{O} + \text{M}$ minus $\text{N}_2\text{O} + \text{H} \rightarrow \text{N}_2 + \text{OH}$.

adiabatic values. Remarkably, the CH_4 emission indices decrease only slightly with dilution, because, as noted above, the opposing effects of dilution leave the flame temperature nearly constant.

Analysis of the chemical rate processes leading to NO production shows that the thermal (Zeldovich) mechanism is the only significant route for NO formation in the CO/H_2 flames. The rate-determining step in this mechanism is the reaction

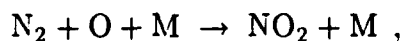


Since the N_2 mole fraction remains nearly constant, NO production in these flames depends on two factors: the O atom concentration history and the temperature history.

Figure 19 illustrates the degree to which predicted O atom concentrations are in excess of their equilibrium values (dashed curves). The O atom superequilibrium ratio is greater for the N_2 diluted flame ($[\text{O}]/[\text{O}]_{\text{eq}} = 6.2$ vs. 1.5), since residence time in this flame is less than half in the undiluted flame (1.7 ms vs. 4 ms). The spikes in the kinetic O atom concentrations occur when the cold mixture in the homogeneous reactor is ignited by the hot stoichiometric mixture in the flame sheet reactor.

More important to NO production is the departure from equilibrium of the flame temperature. Peak temperatures are suppressed approximately 50 K and 250 K for the undiluted and 50%- N_2 flames, respectively (Fig. 19). The temperature during NO production is lower in the diluted flame, so the NO production rate is slower despite the higher O atom concentrations. The temperature effect overwhelms the concentration effect, because the thermal NO reaction has a large activation energy (close to 75 kcal/gmole), as noted by Correa *et al.*, (1984).

In the CH_4 flames, the NO formation chemistry is complicated by the contribution of the prompt mechanism, as initiated by the reaction $\text{N}_2 + \text{CH} \rightarrow \text{HCN} + \text{N}$. The free N atom easily forms NO by collision with either ≤ 2 or OH. The HCN radical can lead to either production or consumption of NO. The prompt initiation step breaks apart 30% of the N_2 that is consumed, compared to 60% via the thermal mechanism (Table I and Fig. 20). The remaining N_2 consumption (10%) occurs via the N_2O route,



which has a rate comparable to the thermal initiation step,

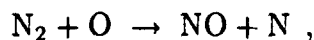


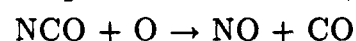
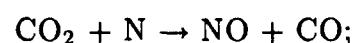
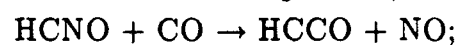
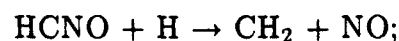
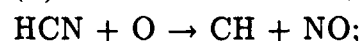
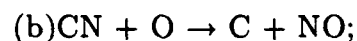
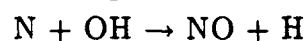
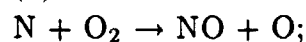
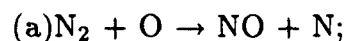
TABLE I
Contributions of various kinetic mechanisms
to total NO production in undiluted CH₄ flames

N₂ consumption (% of total in both reactors):

Path	Homogeneous	Flame-sheet
Thermal	15	45
N ₂ O route	4	6
Prompt	0	30

NO production (% of total in both reactors):

Path	Homogeneous	Flame-sheet
Thermal(a)	21	100
Prompt (b)	0	-18
NO ₂ conversion	-12	4
HNO loop	-3	8



except that most of the N₂O returns to N₂ by collision with H atoms. Of the total N₂ consumed in the simulation, 80% occurs in the flame-sheet reactor, which is not surprising, because the mixture here is hot during the whole flame length. Similarly, 94% of the total NO production comes in the flame-sheet reactor. The contribution of the homogeneous reactor occurs via the thermal mechanism when the reactor ignites at $x/d = 80$ (Fig. 20).

We exercised the model without the prompt reactions included in the mechanism and found that the computed EINO_x was 30% lower than predicted by the

full mechanism. While this agrees with the N_2 consumption associated with the prompt initiation step above, we caution that superposition does not strictly apply to the nonlinear solution.

The evolution of the NO_x emission index in the simulation (Fig. 20) indicates that prior to the ignition of the homogeneous reactor, NO_x produced in the flame-sheet is transported to the homogeneous reactor. When the buoyant switch accelerates the entrainment of cold surroundings at $x/d = 70$, a period of transient NO conversion to HNO occurs in the flame-sheet (dashed curve) via a three-body reaction with H atoms. Shortly thereafter, when the homogeneous reactor ignites, NO production proceeds again, until the fuel is exhausted and the temperature begins to decay. The final emission level comes as a result of the fluid exchange between reactors as they continue to entrain cold air.

Next we examine the NO_2 fraction of the total NO_x . The NO_2 fraction increases as the CO/H_2 flames are increasingly diluted, while the NO_2 fractions are unaffected by dilution in the CH_4 flame (Fig. 19). The model predictions and experiments are in excellent agreement, especially considering the small absolute quantities of NO_2 produced. Although the NO_2 fractions increase in the CO/H_2 flames, NO_2 emission indices ($EINO_2$) actually decrease with N_2 dilution (0.137 – 0.061 g/kg predicted for 0-50% N_2). The model predicts that the NO_2 is formed after NO formation is complete, well downstream of the maximum temperature. It is also interesting to note that the peak NO_2 production occurs in all of the flames in the temperature range of 1100 – 1400 K.

In conclusion, predictions from a turbulent jet flame model that employs a relatively simple model of fluid mixing but detailed chemical kinetics were compared with experimental measurements from N_2 -diluted CO/H_2 and CH_4 flames. The model predictions of NO and NO_2 emission indices are in good qualitative and reasonable quantitative agreement with measurements from both flames. Inclusion of the radiant heat losses is necessary to predict NO_x levels and trends with N_2 dilution from the CH_4 flames. The thermal mechanism is the only significant route for NO formation in the homogeneous reactor model of CO/H_2 flames. It is also the dominant route in the CH_4 flames, except for a 30% contribution of the prompt mechanism, which appear in the flame-sheet reactor only.

The different channels of NO_x formation reasonably well predicted by a detailed chemical kinetics model contribute to a better understanding and controlling NO_x emissions from combustion sources. The model is now in good agreement with experimental results, after the mixing rate was determined to be too low, originally.

4. Analytical and computational effort

A new approach for computing multidimensional flows of an inviscid gas has been developed as part of our on-going computational effort. It may be considered an extension of the method of characteristics to multidimensional, unsteady gas dynamics.

The idea is to use the knowledge of the one-dimensional characteristic problem for gasdynamics to compute genuinely multidimensional flows in a mathematically consistent way. A family of spacetime manifolds is found on which an "equivalent" 1-D problem holds. These manifolds are referred to as Riemann Invariant Manifolds and play the role that the characteristic manifolds play in the method of characteristics for 1-D unsteady or 2-D steady gas dynamics. Their geometry depends on the local spatial gradients of the flow and they provide locally a convenient system of coordinate surfaces for spacetime. In the case of zero entropy gradients, functions analogous to the Riemann invariants of 1-D gasdynamics can be introduced. These generalized Riemann Invariants are constant on the Riemann Invariant Manifolds. The equations of motion are integrable on these manifolds and the problem of computing the solution becomes that of determining the geometry of these manifolds locally in spacetime. This theory allows one to look at such flows in a very useful way, reminiscent of the method of characteristics. A whole family of numerical schemes can be devised using these ideas.

The progress made in recent years in the development of numerical schemes for computing such flows is based on the various higher order extensions of the original Godunov (1959) scheme. These schemes allow high order accuracy without spurious oscillations near the flow discontinuities. The main idea of the Godunov scheme and its extensions is to use the knowledge from the theory of characteristics, locally in each computational cell, to compute the various flux terms. By doing this, the local characteristic wave patterns are accounted for, accurately. Since discontinuities are likely to be present, the characteristic problem is generalized to allow for their presence. This constitutes the well known Riemann problem. Two arbitrary constant states, separated by a discontinuity in space, are given as the initial condition. The solution to the Riemann problem is used as the building block for numerical methods of this type. It provides the information needed to compute the fluxes at the interfaces of the computational cells.

Although the application of this idea is straightforward for the one-dimensional case, the extension to multidimensional flows is not. Practically, these schemes are

extended to more dimensions by treating the additional spatial dimensions separately. The computation is not truly multidimensional, but rather a number of separate one-dimensional computations in each spatial direction. Even schemes that appear to be multidimensional (unsplit), actually use the local directions of the grid to set up and solve a 1-D Riemann problem, thus taking advantage of the 1-D results. The only real effort to create a multidimensional scheme are those by Roe (1986), Hirsch & Lacor (1989), and Deconick *et al.* (1986).

We have used the Riemann Invariant Manifold theory to develop a novel scheme. This scheme is a standard high-order shock-capturing Godunov scheme which has been modified to take into account the multidimensional character of the flow in a mathematically consistent way. No flux-splitting or other multidimensional "fixes", that are usually employed, are needed. This multidimensional correction can be directly extended to three-dimensional flows. We are currently testing this scheme on a variety of test problems.

A first paper, documenting our earlier, 1-D unsteady gasdynamic flow simulation method, has been accepted for publication (Lappas *et al.* 1992).

5. Diagnostics and instrumentation development

Our diagnostic and instrumentation development is proceeding very well. A new instrument to measure the turbulent structure(s) convection velocity was previously mentioned in Sec. 2.4, and will not be discussed further here.

As part of a major effort, we have developed the capability to acquire data at very high rates, beyond those achievable with commercial devices. This will permit us to acquire sequences of high resolution images, using CCD cameras. Additionally, we are proceeding with the design of electronics to support a custom CCD array, designed in collaboration with JPL, which has been dubbed the "MACH CCD." The MACH CCD will permit us to record two high-resolution images within a fraction of a microsecond of each other. We will then be able to image supersonic flows, and, utilizing image correlation velocimetry techniques, determine the two-dimensional velocity field in the plane of the images.

5.1 High-speed data acquisition

We have completed the first two A/D converter boards for high speed and high resolution image acquisition. The first board has two 12 bit 15 megahertz A/D converters and can digitize two analog inputs at 15 MHz or one input at 30 MHz. The second board has two 12 bit 20 megahertz A/D converters and can digitize two inputs at 20 MHz or one input at 40 MHz. Both boards have 32 megabytes of local buffer memory and plug into a standard VXI backplane. A VMEbus computer running the OS-9 real time operating system controls the A/D converters through a VME to VXI bus converter. The OS-9 system can transfer the acquired images to the VAXcluster through the Ethernet.

The A/D subsystem has been used with a Hitachi high resolution RGB camera. The camera has three CCD's (one per color) with a resolution of 560H by 480V pixels. A phase locked loop has been built for the Hitachi camera to reconstruct the pixel clock and synchronize the A/D converter boards. We can digitize up to 56 consecutive frames when digitizing 2 of the three colors or up to 28 consecutive frames digitizing all 3 colors.

We have also used a high resolution black and white camera manufactured by Texas Instruments (resolution of 1134H by 480V pixels). This camera has a pixel clock output, so a small board was constructed to buffer the pixel clock, horizontal sync, and vertical sync for the A/D converter boards. One A/D converter board can digitize up to 28 consecutive frames (this can be extended to 56 frames by chaining a second board after the first).

Additionally, we are designing a controller board that will be able to control the MACH dual image CCD camera being built by JPL. The controller board will have two microsequencers. The first (pixel) microsequencer will generate the complex waveforms needed by the MACH CCD camera and control the A/D converter boards. The pixel microsequencer can be programmed to digitize a subset of the image (region of interest) in order to conserve memory. The second (real time) microsequencer is used to generate the timing waveforms for the YAG lasers, the camera shutter, and other laboratory devices. Both microsequencers can be triggered from an external control signal or from the other microsequencer.

For instance, the real time microsequencer can wait for an external trigger signal (e.g. the start of a run), then fire the first YAG laser, tell the pixel microsequencer to store the first image, then fire the second YAG laser, and finally tell the pixel microsequencer to start digitizing the two images. The MACH CCD should be able to acquire two images as short as 200 nanoseconds apart.

5.2 Image correlation velocimetry

We are developing the capability to use the correlation of two scalar images for the purpose of motion detection. In particular, we can map the deformation of a flow field over time. Quantities like the velocity, vorticity, and strain rate are estimated directly from a pair of scalar images. Initial investigations designed to tune this process have examined the flow past a circular cylinder.

To measure the movement of a scalar image over time, consider two images or scalar fields (e.g., dye, temperature, or density), spaced in time. It is clear that there is a mapping taking the first image to the second. One such mapping is simply the motion of the fluid together with the equations of motion of the scalar. Integrating the equation of motion of a scalar, over time, we may write:

$$\mathcal{I}_{t_1}(\xi(\mathbf{x})) - \mathcal{I}_{t_0}(\mathbf{x}) - \mathcal{D} \int_{t_0}^{t_1} \nabla^2 \mathcal{I}(\mathbf{x}(t)) dt \equiv 0, \quad (12)$$

where $\xi(\mathbf{x})$ is some (vector) coordinate transformation mapping the image taken at time t_0 , $\mathcal{I}_{t_0}(\mathbf{x})$, to the image at time t_1 , $\mathcal{I}_{t_1}(\mathbf{x})$. The unknown, and highly nonlinear vector transformation $\xi(\mathbf{x})$, is then calculated by solving Eq. 12. A more reliable method is to minimize Eq. 12 over some volume V , *e.g.*, in a least squares sense,

$$\min_{\xi(\cdot)} \int_V \left[\mathcal{I}_{t_1}(\xi(\mathbf{x})) - \mathcal{I}_{t_0}(\mathbf{x}) - \mathcal{D} \int_{t_0}^{t_1} \nabla^2 \mathcal{I}(\mathbf{x}(t)) dt \right]^2 d\mathbf{x} \quad (13)$$

Now consider that $\xi(\mathbf{x})$ is just a displacement of some point \mathbf{x} to another $\xi(\mathbf{x})$. Since $\xi(\mathbf{x})$ is a complicated nonlinear function we linearize (locally expand) in a neighborhood \mathcal{N} about a point $\hat{\mathbf{x}}$, so,

$$\xi(\mathbf{x}) = \xi(\hat{\mathbf{x}}) + (\mathbf{x} - \hat{\mathbf{x}}) \cdot \nabla \xi(\hat{\mathbf{x}}) + \dots \quad (14)$$

Clearly $\xi(\hat{\mathbf{x}})$ is the displacement (velocity) of the center of \mathcal{N} , and $(\mathbf{x} - \hat{\mathbf{x}}) \cdot \nabla \xi(\hat{\mathbf{x}})$ is the local deformation (rotation, strain, dilatation, *etc.*), that \mathcal{N} experienced when moving from $\hat{\mathbf{x}}$ to $\xi(\hat{\mathbf{x}})$.

Note that the state of the art in image velocimetry does no better than the first order displacement, $\xi(\hat{\mathbf{x}})$, of \mathcal{N} . Using Eqns. 13 and 14 over a neighborhood \mathcal{N} yields,

$$\min_{\xi(\hat{\mathbf{x}}), \nabla \xi(\hat{\mathbf{x}}), \dots} \int_{\mathcal{N}} \left[\mathcal{I}_{t_1}(\xi(\hat{\mathbf{x}}) + (\mathbf{x} - \hat{\mathbf{x}}) \cdot \nabla \xi(\hat{\mathbf{x}}) + \dots) - \mathcal{I}_{t_0}(\mathbf{x}) - \mathcal{D} \int_{t_0}^{t_1} \nabla^2 \mathcal{I}(\mathbf{x}(t)) dt \right]^2 dV \quad (15)$$

Note that there is little justification in going beyond the second order term in Eq. 15. This is because of the rapid increase in the number of parameters that occurs when going to higher order in the minimization. Trying to fit too many parameters would be time-consuming, and, in the presence of noise, meaningless.

Our experience suggests that a second order expansion of the displacement field will yield better velocity estimates than results using a traditional first order approximation. Keeping the second order terms in the minimization (Eq. 15) increases the reliability of the first order term, particularly in regions where the flow contains large velocity gradients or rotational motions. In addition, the local vorticity, strain, and divergence can be determined directly from the minimization parameters, obviating the large errors inherent in using only the first order estimate of the displacement and then differentiating to obtain these higher order derivatives of the flow field.

The high-speed data acquisition is part of the work by D. Lang, and the scalar correlation velocimetry is being carried out by P. Tokumaru, both in collaboration with P. Dimotakis.

6. Personnel

In addition to the Principal Investigators:

P. E. Dimotakis: Professor, Aeronautics & Applied Physics;

J. E. Broadwell: Senior Scientist, Aeronautics;

A. Leonard: Professor, Aeronautics;

other personnel who have participated directly in the effort during the current reporting period are listed below (all are in the Aeronautics option):

C. L. Bond: Graduate Research Assistant;

H. J. Catrakis: Graduate Research Assistant;

E. Dahl: Member of the Technical Staff;

D. C. Fourquette: Post-doctoral Research Fellow;

R. J. Gilbrech: Graduate Research Assistant; ‡

J. L. Hall: Graduate Research Assistant; *

D. B. Lang: Staff Engineer;

T. Lappas: Graduate Research Assistant;

P. L. Miller: Post-Doctoral Research Fellow;

H. Rosemann: Post-doctoral Research Fellow; **

P. T. Tokumaru: Post-doctoral Research Fellow.

‡ Ph.D., June 1991; presently working for NASA's Stennis Space Center, Mississippi.

* Ph.D., June 1991.

** Appointment ended, June 1991; presently working for the DLR, Göttingen, Germany.

7. References

Bibliographical references denoted by a bullet (•) in this list below represent publications of work under the sponsorship of this Grant that have appeared during the present reporting period.

BATCHELOR, G. K. 1959 "Small-scale variation of convected quantities like temperature in turbulent fluid. Part 1. General discussion and the case of small conductivity," *J. Fluid Mech.* **5**, 113-133.

BECKER, H. A. & YAMAZAKI, S. 1978 "Entrainment, Momentum and Temperature in Vertical Free Turbulent Diffusion Flames," *Comb. and Flame* **33**, 123-149.

CHEN, C. J. & RODI, W. 1980 *Vertical Turbulent Buoyant Jets. A Review of Experimental Data* (Pergamon Press, Oxford).

CHINZEI, N., MASUA, G., KOMURO, T. MURAKAMI, A. & KUDOU, K. 1986 "Spreading of two-stream supersonic turbulent mixing layers," *Phys. Fluids* **29**, 1345-1347.

CLEMENS, N. T. & MUNGAL, M. G. 1990 "Two- and Three-Dimensional Effects in the Supersonic Mixing Layer," 26th AIAA/SAE/ASME/ASEE Joint Propulsion Conference, Paper 90-1978.

CORREA, S.M., DRAKE, M.C., PITZ, R.W. & SHYY, W. 1984 "Prediction and Measurement of a Non-Equilibrium Turbulent Diffusion Flame," 20th Symposium (Int) on Combustion, p.337, The Combustion Institute.

DECONINCK, H., HIRSCH, C. & PEUTEMAN, J. 1986 "Characteristic Decomposition Methods for the Multidimensional Euler Equations," 10th International Conference on Numerical Methods in Fluid Dynamics (Beijing, June 1986).

- DIMOTAKIS, P. E. 1991 "Fractals, dimensional analysis and similarity, and turbulence," *Nonlinear Sci. Today* #2/91, pp. 1, 27-31 (Appendix C, this report).
- DIMOTAKIS, P. E. 1991 "Turbulent Free Shear Layer Mixing and Combustion," *High Speed Flight Propulsion Systems, in Progress in Astronautics and Aeronautics* **137**, Ch. 5, 265-340.

DIMOTAKIS, P. E. & MILLER, P. L. 1990 "Some consequences of the boundedness of scalar fluctuations," *Phys. Fluids A* **2**(11), 1919-1920.

DOWLING, D. R. 1988 *Mixing in Gas Phase Turbulent Jets*, Ph.D. thesis, California Institute of Technology.

DOWLING, D. R. & DIMOTAKIS, P. E. 1990 "Similarity of the concentration field of gas-phase turbulent jets," *J. Fluid Mech.* **218**, 109-141.

- GILBRECH, R. J. 1991 *An Experimental Investigation of Chemically-Reacting, Gas-Phase Turbulent Jets*, Ph.D. thesis, California Institute of Technology.
- GILBRECH, R. J. & DIMOTAKIS, P. E. 1992 "Product Formation in Chemically-Reacting Turbulent Jets," *AIAA 30th Aerospace Sciences Meeting*, AIAA Paper 92-0581 (Appendix B, this report).

GODUNOV, S. K. 1959 "A Finite Difference Method for the Numerical Computation of Discontinuous Solutions of the Equations of Fluid Dynamics," *Mat. Sb.* **47**, 271-306.

HALL, J. L. 1991 *An Experimental Investigation of Structure, Mixing and Combustion in Compressible Turbulent Shear Layers*, Ph.D. thesis, California Institute of Technology.

HIRSCH, C. & LACOR, C. 1989 "Upwind Algorithms Based on a Diagonalization of the Multidimensional Euler Equations," AIAA Paper No. 89-1958.

KEE, R. J., MILLER, J. A. & JEFFERSON, T. H. 1980 "CHEMKIN: A General Purpose, Problem-independent, Transportable, Fortran Chemical Kinetics Code Package," SANDIA Report SAND80-8003.

- LAPPAS, T., LEONARD, A. & DIMOTAKIS, P. E. 1992 "An Adaptive Lagrangian Method for Computing 1-D Reacting and Non-Reacting Flows," *J. Comp. Phys.* (to appear).
- MILLER, P. L. 1991 *Mixing in High Schmidt Number Turbulent Jets*, Ph.D. thesis, California Institute of Technology.

MILLER, P. L. & DIMOTAKIS, P. E. 1991a "Stochastic geometric properties of scalar interfaces in turbulent jets," *Phys. Fluids A* **3**(1), 168-177.

- MILLER, P. L. & DIMOTAKIS, P. E. 1991b "Reynolds number dependence of scalar fluctuations in a high Schmidt number turbulent jet," *Phys. Fluids A* **3**(5), 1156-1163 (Appendix A, this report).

MILLER, P. L. & DIMOTAKIS, P. E. 1992 "Measurements of scalar power spectra in high Schmidt number turbulent jets," *Phys. Fluids A* (submitted).

PAPAMOSCHOU, D. 1989 "Acoustic Paths in Compressible Shear Layers," *Bull. Am. Phys. Soc.* **34**(10), 2252.

PAPAMOSCHOU, D. & ROSHKO, A. 1988 "The Compressible Turbulent Shear Layer: An Experimental Study," *J. Fluid Mech.* **197**, 453-477.

ROE, P. L. 1986 "Discrete Models for the Numerical Analysis of Time-Dependent Multidimensional Gas Dynamics," *J. Comp. Phys.* **63**, 458-476.

WHITE, F. M. 1974 *Viscous Fluid Flow* (McGraw-Hill, New York).

Appendix A

MILLER, P. L. & DIMOTAKIS, P. E. 1991 "Reynolds number dependence of scalar fluctuations in a high Schmidt number turbulent jet," *Phys. Fluids A* **3**(5), 1156–1163.

Reynolds number dependence of scalar fluctuations in a high Schmidt number turbulent jet

Paul L. Miller and Paul E. Dimotakis

Graduate Aeronautical Laboratories, California Institute of Technology, Pasadena, California 91125

(Received 28 August 1990; accepted 9 January 1991)

The scalar rms fluctuations in a turbulent jet were investigated experimentally, using high-resolution, laser-induced fluorescence techniques. The experiments were conducted in a high Schmidt number fluid (water), on the jet centerline, over a jet Reynolds number range of $3000 < Re < 24\,000$. It was found that the normalized scalar rms fluctuations c'/\bar{c} decrease with increasing flow Reynolds number, at least for the range of Reynolds numbers investigated. Since c'/\bar{c} is a measure of the inhomogeneity of the scalar field, this implies that high Schmidt number turbulent jets become more homogeneous, or better mixed, with increasing Re . These findings need to be assessed in the context of the documented Reynolds number independence of flame length for $Re > 3000$ or 6500 .

1. INTRODUCTION

The correct description of the probability density function (pdf) of the fluctuations of a conserved passive scalar in turbulent flow has been a matter of theoretical and engineering interest for some time. Knowing the pdf of the conserved scalar allows the computation of the amount of chemical product that would be formed in a chemical reaction in which the scalar is transported as a passive quantity.¹

Experimental evidence and theoretical arguments in the last few years suggest that the turbulent mixing process is sensitive to the value of the molecular diffusion coefficients, even at Reynolds numbers typically regarded as high. We recognize that this remains a controversial proposal, at this writing, especially in the case of turbulent jet mixing.² We note, in particular, that accepting it would imply that the conserved scalar pdf, as well as other statistics of the mixing process, should be expected to be functions of the flow Reynolds number $Re = U\delta/\nu$, where U is the local flow velocity, δ is the local extent of the turbulent flow and ν denotes the (molecular) kinematic viscosity, and the Schmidt number $Sc = \nu/\mathcal{D}$, where \mathcal{D} is the scalar species (molecular) diffusivity. There is no consensus at this time as to how such effects should be described, let alone predicted, with the associated nonlinear dynamics essentially involving terms in the equations of motion with factors that vanish, multiplied by factors that become unbounded in the limit of $Re \rightarrow \infty$, or $Sc \rightarrow \infty$.

Nevertheless, the qualitative dependence on Sc might be argued on simple grounds, namely, that decreasing the species diffusivity, i.e., increasing the Schmidt number, keeping all other flow and fluid quantities fixed, can only decrease the rate of (molecular) mixing and the amount of mixed fluid. This is corroborated by a comparison of the results of experiments in gas phase shear layers³ ($Sc \sim 1$) versus those in liquid phase shear layers⁴ ($Sc \sim 10^3$) at comparable Reynolds numbers.

An *a priori* argument for the dependence on Reynolds number is not as straightforward. Reliable experimental

data at large Reynolds numbers are difficult to obtain. Experiments at high Reynolds numbers must rely on chemically reacting flows to infer the degree of molecular mixing. In the case of gas phase shear layers, the experimental evidence from a single experiment is that the amount of mixing decreases as the Reynolds number increases, albeit slowly.⁵ The evidence shows a Reynolds number dependence in liquid phase shear layers that appears to be weaker, but this conclusion is based on scatter data.⁴

In turbulent jets, the behavior is even less clear. Experimental "flame length" data in liquid jets,⁶ as well as other liquid and gas phase turbulent jet flame length data reviewed in Fig. 1 of Dahm and Dimotakis,⁷ suggest that this quantity may well be independent of both Schmidt number and Reynolds number, at least for Reynolds numbers greater than about 3×10^3 , or so, as had been reported in the earlier Weddell⁸ (see also Hottel, Ref. 9) findings. The scatter in these data is large enough, however, to have masked a weak dependence on Schmidt number or Reynolds number, not to speak of the likely contamination of the results by buoyancy effects in the case of high heat release, gas phase jet flames. As a case in point, the results of Kristmanson and Danckwerts¹⁰ suggest that Reynolds number independence of the flame length in a liquid jet does not occur until a Re greater than 6500 , or so.

More recently, direct measurements of the jet fluid concentration pdf in gas phase turbulent jets by Dowling and Dimotakis¹¹ suggest a Reynolds number independence, at least in the Reynolds number range from 5.0×10^3 to 4.0×10^4 . These authors also compare their estimates of the jet fluid concentration pdf on the jet axis with those measured by other investigators,¹²⁻¹⁶ for Schmidt (Prandtl) numbers ranging from 0.7 to 10^3 and Reynolds numbers ranging from 5×10^3 to 5.2×10^4 (Dowling and Dimotakis,¹¹ Fig. 28). While the reported pdf's may not collapse particularly well, it is difficult to assess whether the differences are attributable to Schmidt number or Reynolds number effects, or to experimental difficulties.

Our own investigations of the behavior of the turbulent

jet fluid concentration fluctuations were undertaken as part of a larger effort to address the role of Reynolds number as a parameter in the dynamics of turbulent jet mixing. The experiments reported here were performed in liquid phase turbulent jets ($Sc \sim 10^3$), in a Reynolds number range from 3.0×10^3 to 2.4×10^4 . Our measurements permitted direct estimates of the pdf, rms, as well as the spectrum of the conserved scalar fluctuations to be computed.

II. APPARATUS AND PROCEDURE

While the experimental setup has been documented previously,^{6,17} the following short description is included for completeness. The experiments were carried out utilizing the facility shown in Fig. 1. A large rectangular water tank, about 1 m square and 2 m high, acted as the (discharge) reservoir. Large windows on all sides of the tank provided optical access. To establish the flow, the jet plenum was filled with water tagged by a fluorescent laser dye (sodium fluorescein) and air was sonically metered to drive the jet fluid at constant velocity through a 2.54 mm (0.1 in.) diam nozzle at the base of the plenum. The beam from an argon ion

laser was passed through appropriate optics and aligned radially through the centerline of the jet. A beam stop prevented reflections from the opposite window. For these measurements, the laser beam optics were designed to generate a small Gaussian waist at the focus. A low laser power of 1.0 W was used to avoid heating of the dyed fluid in the very small focal volume and to prevent saturation. The plenum dye concentration was kept less than 10^{-6} M. Consequently, the much lower concentrations at the measuring station did not significantly attenuate or steer the beam.

A low $f\#$ lens was used to collect light from a short segment centered at the waist of the focused laser beam (on the jet centerline, at $x/d = 100$) onto a photomultiplier tube, effectively yielding single-point concentration values versus time. An optical low-pass filter eliminated background laser light, transmitting only the frequency-shifted fluorescence. A slit spatial filter defined the length of the laser line segment sampled. The slit width was chosen such that the sampling volume was roughly cylindrical, about $80 \mu\text{m}$ in diameter and less than $50 \mu\text{m}$ in length. The use of the slit rather than a pinhole ensured that any small transverse beam movements did not alter the measurement volume. The long Rayleigh range and latitude in the depth of field

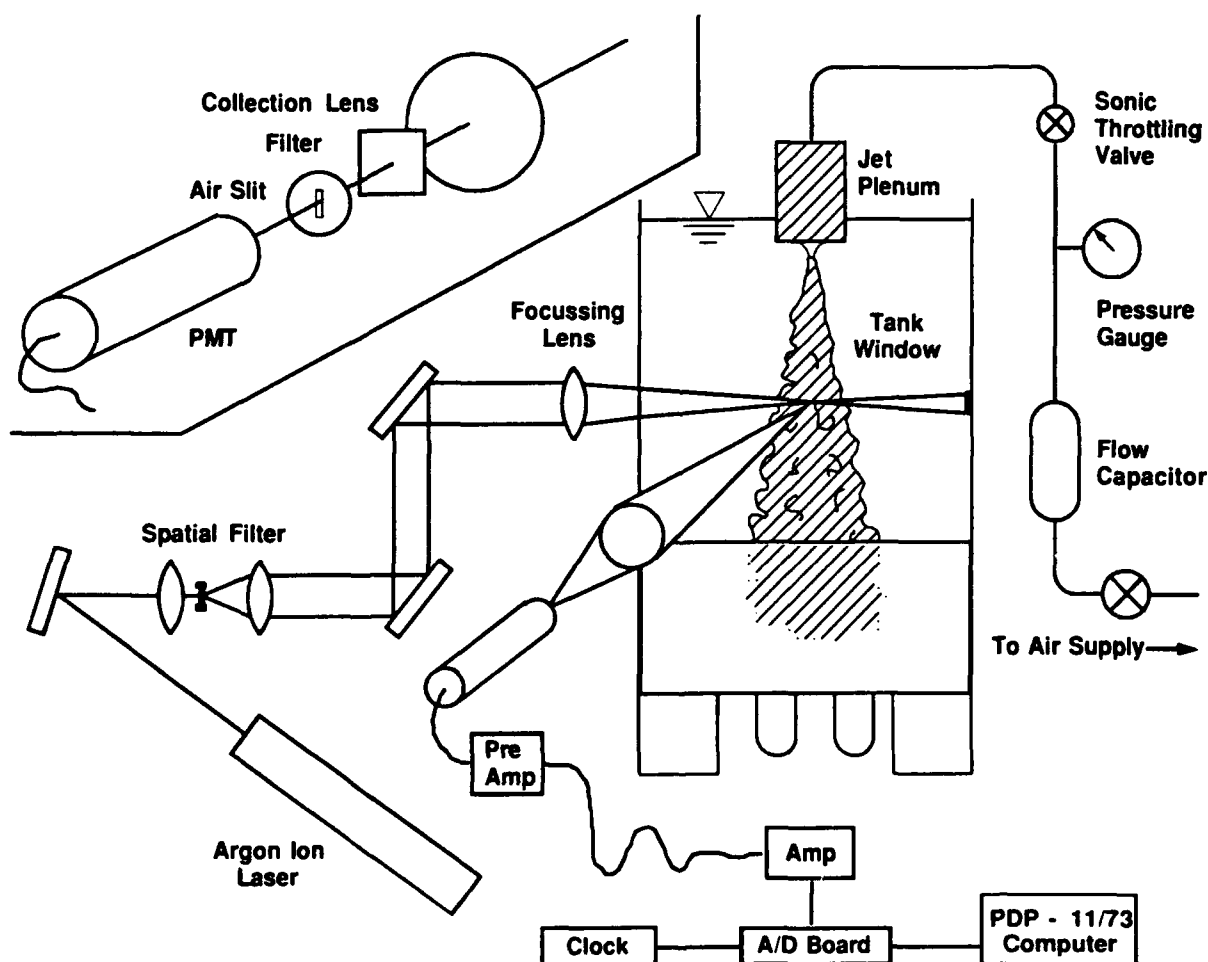


FIG. 1. Experimental apparatus.

minimized the effect of motion in either of the two horizontal directions. Data acquisition was computer-controlled. The signal amplifier incorporated a three-pole Butterworth filter, with a cutoff frequency set slightly under 10 kHz. The data were sampled at 20 kHz for all the runs.

Careful consideration has been given to the reduction of noise in these measurements, especially since we wish to examine the normalized scalar rms fluctuations, c'/\bar{c} . As described previously,^{17,18} we utilized Wiener filter techniques^{19,20} in processing the data. The issues of buoyancy and attenuation of the laser beam have been examined, and are discussed in Appendix A. We conclude that neither is a factor in these jets. Finally, an important consideration when measuring a quantity such as c'/\bar{c} is resolution, since fluctuations at scales smaller than the measuring volume are low-pass filtered. It is therefore necessary to determine that either the smallest scales of the flow are resolved or that the contribution to the fluctuations by scales smaller than the resolution is negligible. We discuss resolution concerns later in this paper.

III. RESULTS

For our discussions, the jet Reynolds number is defined as $Re = U_0 d / \nu$, where U_0 is the jet exit velocity, d is the diameter of the jet nozzle, and ν is the kinematic viscosity of the working fluids (water).

Our measurements indicate that the scalar field of a high Schmidt number turbulent jet has, in some sense, not reached an asymptotic state for Re as large as 10 000 to 20 000, or more. This is apparent in the behavior of the scalar pdf's with varying Re . In Fig. 2, we show four sample pdf's, spanning Reynolds numbers from 3000 to 24 000. One hundred and fifty histogram bins were used to compile each pdf. Approximately 34 large-scale structure passages were captured at the lowest Re , and over 125 at the highest.

These pdf's display a decreasing relative concentration fluctuation amplitude and imply that the jet is becoming more homogeneous in composition with increasing Re . It could be argued that this may be attributable to worsening resolution, as Re increases. It turns out, however, that the

effect is not due to resolution difficulties, as will be addressed below.

Another manifestation of a change with Re is in the corresponding scalar power spectra (Fig. 3). Here, we plot the spectra $E_c(f\tau_\delta)$ at the four Reynolds numbers, normalized by the estimated large-scale times,

$$\tau_\delta \equiv \delta / U_{cl}, \quad (1)$$

and the local mean concentration squared, \bar{c}^2 . The frequency axis has also been nondimensionalized by τ_δ . With these normalizations, equal (equivalent) length scales line up on the $f\tau_\delta$ axis, regardless of Re . The large-scale passage frequencies, as independently estimated by the local centerline velocities divided by the width of the jet, are seen to be aligned at $f\tau_\delta = 1$, corresponding to the length scale δ . So, alternatively, the $f\tau_\delta$ axis can be viewed as a nondimensional, inverse length scale, which is the same for all Re . This view will be useful in the discussion below.

An important observation is that these spectra do not collapse when normalized in this fashion. The central (mid-frequency) portion of the spectra can be seen to bulge upward with decreasing Reynolds number. This might, perhaps, be understandable given the low Re involved and the documented reluctance of the jet spectrum to develop a constant slope region until at much higher Re . However, in addition to the shape differences, there is a discrepancy between the low-frequency levels of the spectra. If the normalization was the cause of these discrepancies, the only "free" parameter would be τ_δ , the estimate of the large-scale time.

Two considerations help to rule out attributing the variations to the value of τ_δ . One is that, since τ_δ multiplies the frequency but divides the spectrum, changes in τ_δ shift the normalized spectra along lines of slope -1 . This does not improve the collapse. The second point is that the ratio of the constant level region at the lowest Re to that at the highest Re is greater than 2. A variation in τ_δ by this amount is not admissible by the uncertainties in this quantity. Therefore, possible uncertainties in normalization cannot explain the variation in the spectra observed.

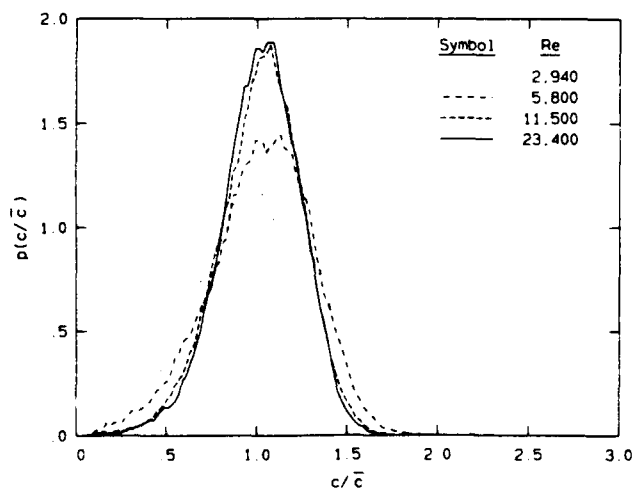


FIG. 2. Scalar pdf's for varying Re (on axis, $x/d = 100$).

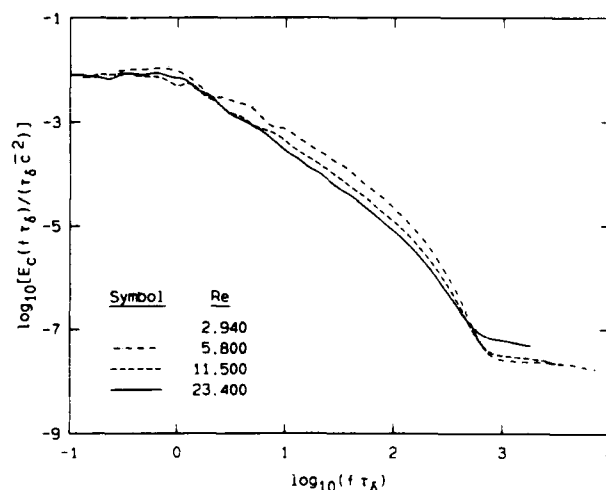


FIG. 3. Normalized scalar power spectra for varying Re (on axis, $x/d = 100$).

Since the area under the power spectrum is equal to $\overline{c'^2}/\bar{c}^2$, the bulging spectra at the lower Re also indicate that c'/\bar{c} decreases with increasing Re. It is significant that the area of greatest contribution to this effect is at scales *unaffected by potential resolution difficulties*, namely, from the variation at the lower frequencies, corresponding to time scales of the order of the large-scale passage time, or length scales close to the local jet diameter.

We calculate the normalized scalar rms c'/\bar{c} from the data and plot it as a function of Re (Fig. 4). These values are, again, from data collected at $x/d = 100$, with the exception of one point (fifth from the right), which is from data recorded at $x/d = 300$. The resulting c'/\bar{c} can be seen to continuously decrease with increasing Re. This is consistent with the behavior of the pdf's and the spectra. The smooth line in Fig. 4 was generated by fitting the measured values of c'/\bar{c} using a function of the form

$$c'/\bar{c} = A + B \text{Re}^p. \quad (2)$$

The values of the fit parameters obtained were $A = 0.20$, $B = 550$, and $p = -1.02$. The quality of the fit is insensitive to small changes (of several percent) in these parameter values, as measured by the mean squared error's response.

We note that the nonzero value of A indicates that c'/\bar{c} may be approaching an asymptotic value of about 0.20 at very large Reynolds numbers. We will return to this point below.

IV. ISSUES OF RESOLUTION

The issue of resolution for these measurements is crucial and was discussed in Miller and Dimotakis.¹⁷ To reiterate, the Kolmogorov²¹ scale can be estimated directly from its definition in terms of the mean energy dissipation rate, i.e.,

$$\lambda_K \equiv (\nu^3/\epsilon)^{1/4}. \quad (3)$$

Using the result of Friehe *et al.*²² for the kinetic energy dissipation rate ϵ on the centerline of a turbulent jet,¹¹ i.e.,

$$\epsilon = 48(U_0^3/d) [(x - x_0)/d]^{-4}, \quad (4)$$

the Kolmogorov scales for these measurements are found to range from roughly 50 to 250 μm . By similarity arguments, the velocity field spatial scale where the action of viscosity will become important, say, λ_v , will be some multiple of λ_K . Normalized energy spectra are found to break from a constant power law at a wave number k_v such that $k_v \lambda_K \approx 1/8$ (e.g., Chapman²³). This yields an estimate of

$$\lambda_v = \pi/k_v \sim 25\lambda_K. \quad (5)$$

The smallest expected scalar diffusion scale λ_s is smaller yet by a factor of $\text{Sc}^{1/2}$ (Batchelor²⁴), or ~ 30 in this case, yielding an estimate for λ_s very close to λ_K (in water). These estimates are corroborated by the gas phase experiments of Dowling and Dimotakis¹¹ as well as the measurements in water by Buch and Dahm²⁵ and suggest that the smallest diffusion scales may have been resolved in these experiments, at least at the lower Reynolds numbers.

There are three resolution requirements on these measurements: spatial, temporal, and signal-to-noise (SNR). If we convert our spatial resolution estimate to the units of Fig. 3, using the mean centerline velocities, we obtain values of about $f\tau_\delta = 1350$. Note that this value is the same on the nondimensionalized frequency axis for all four Re, just as with the large-scale passage times. If we accept that the highest resolvable frequency is half this value, we estimate our spectra are spatially resolved up to about 2.8 on the log scale of Fig. 3. Thus, at the lower Reynolds numbers, the spatial resolution is at least as restrictive as SNR resolution, while for the highest Re, the SNR may be slightly more important in determining the limit of resolution.

To estimate the impact of resolution on these measurements, we utilize a common classical model spectrum. At sufficiently high Re, one might expect the spectrum to have assumed a similarity form. We approximate this as a constant level from zero frequency to the large-scale passage frequency, a region of constant $-5/3$ slope, and zero beyond a cutoff at $f_c \tau_\delta$ (Fig. 5). The constant level value is defined as

$$K^2 \equiv E_c(f\tau_\delta < f_c \tau_\delta) / \bar{c}^2 \tau_\delta. \quad (6)$$

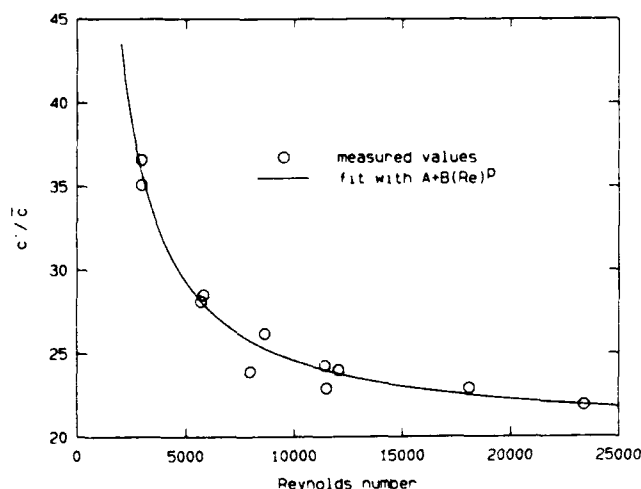


FIG. 4. Normalized scalar rms fluctuations for varying Re (on axis, $x/d = 100$ and 300). The data were fit with a function of the form $A + B \text{Re}^p$. The parameter values determined by the fit are $A = 0.20$, $B = 550$, and $p = -1.02$.

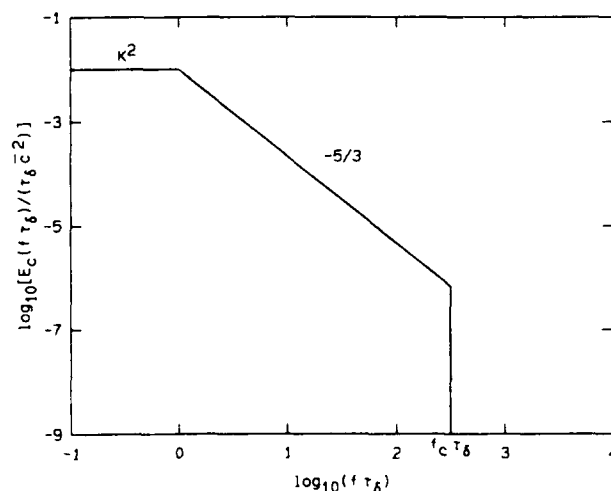


FIG. 5. Model spectrum.

The spectrum is normalized here to the variance of the scalar fluctuations, i.e.,

$$\overline{c'^2} = 2 \int_0^\infty \frac{E_c(f\tau_\delta)}{\tau_\delta} d(f\tau_\delta), \quad (7)$$

which relates the spectrum directly to c'/\bar{c} . We integrate the model spectrum

$$\begin{aligned} \frac{1}{2} \frac{\overline{c'^2}}{\bar{c}^2} &= \int_0^{f_\delta \tau_\delta} K^2 d(f\tau_\delta) \\ &+ \int_{f_\delta \tau_\delta}^{f_c \tau_\delta} K^2 (f\tau_\delta)^{-5/3} d(f\tau_\delta) \end{aligned} \quad (8)$$

to obtain the result

$$c'/\bar{c} = K \{2 + 3[1 - (f_\delta/f_c)^{2/3}]\}^{1/2}. \quad (9)$$

On the jet axis and at fixed x/d , this can be expressed as a function of Reynolds number by substituting for f_δ and f_c (cf. Dowling¹⁸), yielding

$$c'/\bar{c} = K [2 + 3(1 - 0.928 \text{Re}^{-1/2})]^{1/2}. \quad (10)$$

Several things are apparent from Eq. (10). First, it indicates that c'/\bar{c} would be expected to *increase* slightly with Reynolds number. This is opposite to the trend exhibited by our data. Also, we note that at infinite Reynolds number Eq. (10) predicts a finite value for c'/\bar{c} of $\sqrt{5}K$. To evaluate this expression for our measurements, we fit the level, low-frequency, portion of our highest Re spectrum to determine K^2 , yielding $K^2 \approx 0.0078$ and an asymptotic value of $c'/\bar{c} \approx 0.198$. This value of K^2 agrees well with the corresponding estimate from gas phase data,¹¹ while the asymptotic value of c'/\bar{c} agrees with the suggested infinite Re value of 0.20 obtained by fitting the data [parameter A in Eq. (2)]. Finally, the Reynolds number dependence of c'/\bar{c} in Eq. (10) is extremely weak. For Re in excess of 10^3 , c'/\bar{c} has attained over 99% of the infinite Re asymptotic estimate.

The model spectrum also helps demonstrate the effect resolution limitations would have on the resulting measure of c'/\bar{c} . The picture is much the same as in Fig. 5, but we assume that the measured spectrum is resolution-limited at some nondimensional frequency $f_r \tau_\delta$ (Fig. 6). The lost contribution to c'/\bar{c} , represented by the area under the spectrum between $f_r \tau_\delta$ and $f_c \tau_\delta$, i.e.,

$$\Delta c'/\bar{c} = c'/\bar{c} - [c'/\bar{c}]_r, \quad (11)$$

is equal to

$$\Delta c'/\bar{c} = \sqrt{3}K [(f_\delta/f_r)^{2/3} - (f_\delta/f_c)^{2/3}]^{1/2}, \quad (12)$$

while the ratio of the resolution-limited value and the true value is given by

$$\frac{[c'/\bar{c}]_r}{c'/\bar{c}} = \left(\frac{2 + 3[1 - (f_\delta/f_r)^{2/3}]}{2 + 3[1 - (f_\delta/f_c)^{2/3}]} \right)^{1/2}. \quad (13)$$

Here, again, the ratio f_δ/f_r is very small for the Reynolds numbers of interest. As a result, if the ratio f_δ/f_r is also kept small, resolution can hardly affect the measured c'/\bar{c} at these Re, because the expression in Eq. (13) is then very close to unity. Also note that if the scalar spectrum is adequately described by the model spectrum and a particular Reynolds number measurement is resolution limited, higher

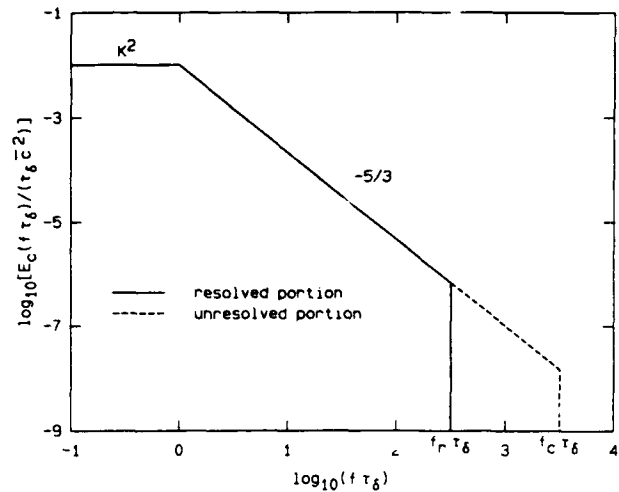


FIG. 6. Resolution-limited model spectrum.

Re data should yield the *same* (measured) value of $[c'/\bar{c}]_r$ (not less). This is clear because the measured spectra should then have the same shape and same extent, correspondingly yielding the same values of $[c'/\bar{c}]_r$. If a Batchelor k^{-1} region²⁴ was incorporated into the model spectrum, it would not alter these results at the present Schmidt number of about 10^3 (see Moffat²⁶). We conclude that our measurements of c'/\bar{c} are *not significantly affected by resolution difficulties*.

Finally, recall that we have argued that we may, in fact, be resolving the smallest diffusion scales in the flow, at least for the lower Reynolds number flows we have investigated. Specifically, we note that our measured spectra do not appear to support the k^{-1} Batchelor²⁴ prediction at high wave numbers (frequencies). This observation is significant at the value of the Schmidt number applicable here, since $Sc^{1/2} \sim 30$. This would have yielded a k^{-1} portion in the spectrum spanning roughly 1.5 decades in frequency. If our assessment of the resolution of our measurements, relative to the requisite physical scales, is correct, then the resolution and SNR of our measurements, at least at the lower Reynolds numbers, are sufficient to have elucidated this behavior. As regards the transport of scalars characterized by low diffusivity (large Sc) in turbulent jets in the Reynolds number range we have investigated, we are forced to conclude that they do not display a k^{-1} Batchelor spectrum.

This finding should be examined in the context of a theoretical difficulty with the k^{-1} spectrum. In particular, the Batchelor spectrum does not appear to exhibit the correct limiting behavior at high Schmidt numbers (holding all other flow parameters fixed). As Batchelor had noted,²⁴ the variance computed using the k^{-1} spectrum diverges logarithmically with increasing Sc. This divergence, however, is inconsistent with the required behavior of scalar fluctuations, which must remain bounded, irrespective of the value of the Schmidt number, as noted recently. Briefly,²⁷ the variance $\overline{c'^2}$ of a scalar bounded by $c = 0$ and $c = 1$ by the initial/boundary conditions is bounded, in turn, by

$$\max\{\overline{c'^2}\} = \bar{c}(1 - \bar{c}). \quad (14)$$

This maximum is expected in the limit of (identically) zero diffusivity, $\mathcal{L} \rightarrow 0$, or $Sc \rightarrow \infty$ if all other flow parameters are held fixed, and corresponds to a limiting pdf of

$$p(c) \rightarrow (1 - \bar{c})\delta(c) + \bar{c}\delta(1 - \bar{c}),$$

i.e., stirring but no (molecular) mixing by the turbulent flow. A logarithmic divergence of $\overline{c'^2}$ as $Sc \rightarrow \infty$, as estimated by the integral over the k^{-1} scalar spectrum, is inconsistent with the bound of Eq. (14).

V. CONCLUSIONS

We have conducted high-resolution, single-point, scalar measurements on the centerline in the far field of an axisymmetric, turbulent jet at high Schmidt number $Sc \sim 10^3$, over a range of Reynolds numbers between 3000 and 24 000. The jet (Taylor) microscale Reynolds number, estimated by¹¹

$$Re_T \approx 1.4 Re^{1/2}, \quad (15)$$

was, therefore, approximately 80 at $Re = 3000$ and 220 at $Re = 24\,000$. Except, perhaps, for the lowest values, such microscale Reynolds numbers are regarded as high by some turbulence criteria.²⁸ Nevertheless, our experiments indicate that, in a number of ways, at least at high Schmidt numbers, jet mixing has not attained asymptotic behavior by $Re \approx 2.4 \times 10^4$. In particular, pdf's and spectra of c'/\bar{c} , the normalized jet fluid concentration, are found to depend on Reynolds number. The rms concentration fluctuations c'/\bar{c} were found to continuously decrease with increasing Re , over the Reynolds number range examined.

We have argued, on the basis of our spectral measurements and the use of a simple model spectrum, that these results are not an artifact of inadequate resolution. In particular, the Reynolds number dependence of c'/\bar{c} , as estimated on the basis of the model spectrum, should have exhibited the opposite behavior to that observed. The limiting values of c'/\bar{c} at high Re , from both the model and the experimental estimates, agreed quite well, suggesting that $c'/\bar{c} \approx 0.20$ may represent an asymptotic value for the normalized rms of the jet fluid concentration fluctuations, at $Sc \sim 10^3$, on the jet axis. Our measurements did not extend to jet Reynolds numbers high enough to confirm such asymptotic behavior directly.

As noted earlier, measurements in gas phase jets at comparable Reynolds numbers¹¹ suggest that, at least for $Sc \sim 1$, the pdf of jet fluid concentration does not exhibit as strong a Reynolds number dependence as we are reporting here, if any at all. This difference in behavior may, of course, be a manifestation of Schmidt number effects. At this time, we cannot reconcile the disagreement between the Reynolds number dependence of the present results and the liquid phase "flame length" data of Weddell⁸ (see also Hottel, Ref. 9), and Dahm *et al.*²⁹ In particular, on the basis of our measured pdf's of concentration, we would conclude that, in liquid phase ($Sc \sim 10^3$) jets, one should observe decreasing flame lengths with increasing Reynolds number, at least within the Reynolds number range investigated here (see Appendix B). We note, however, that Kristmanson and Danckwerts¹⁰ found the flame length to vary with Re until

about twice as large a Reynolds number as Weddell, and Dahm *et al.*

In summary, we have found that the pdf's of the jet fluid concentration become narrower with increasing Reynolds number. A measure of this trend is provided by c'/\bar{c} , the normalized rms level of scalar fluctuations, which decreases as the Reynolds number increases. These measures of unmixedness suggest a more homogeneous turbulent, liquid phase, jet fluid concentration field, i.e., better molecular mixing, with increasing Reynolds number. Our spectra also evolve with increasing Reynolds number, developing a constant slope, close to $-5/3$, at the higher values.

Finally, we did not observe a k^{-1} spectral behavior at the small scales,²⁴ even though the predicted range of validity of this regime would be quite large at this Schmidt number and falls within the resolution range of our measurements at the lower Reynolds numbers that were investigated.

ACKNOWLEDGMENTS

We would like to acknowledge the contributions of D. Lang to the experiments, as well as helpful discussions with J. E. Broadwell and A. R. Kerstein.

This work was performed under AFOSR Grants No. 83-0213 and No. 88-0155, and GRI Contract No. 5087-260-1467.

APPENDIX A: ISSUES OF BUOYANCY

An experimental consideration that was addressed, in addition to resolution, is buoyancy. There are two cases to be considered: buoyancy from a jet fluid/reservoir fluid density difference, and possible heating of the jet at the measuring station by the laser beam. Briefly, a nondimensionalized buoyancy length scale,³⁰

$$\frac{L_b}{d} \equiv \left(\frac{\pi \rho_j}{4 \rho_r} \right)^{1/4} \left(\frac{\rho_j U_0^2}{(\rho_j - \rho_r)gd} \right)^{1/2}, \quad (A1)$$

where ρ_j the jet fluid density, ρ_r the reservoir fluid density, U_0 is the jet exit velocity, and g the acceleration of gravity, may be derived from dimensional analysis (e.g., Dowling,¹⁸ Sec. A.5). This parameter may then be compared with experimentally derived values to determine the role of buoyancy in the flow. In particular, Papanicolaou and List^{14,15} find that jets are momentum-dominated if x/L_b is less than one, while Chen and Rodi³¹ cite a limit of roughly 0.5.

We will estimate the maximum anticipated density difference and calculate the resulting value of L_b/d . The density difference may arise from the addition of the heavy dye to the jet fluid, or from a temperature mismatch between the jet fluid and the reservoir fluid. Let us consider the two contributions separately, since, it turns out, they are of different magnitudes. The fluorescein dye concentration used in the experiments was roughly 3.3×10^{-7} M. The formula weight of disodium fluorescein is 376.28. This yields an estimate for the dye-induced buoyancy length scale [from Eq. (A1)] of over 19 600 jet nozzle diameters at the lowest Re . For each run, the jet fluid was prepared by diluting a small amount of

concentrated stock solution of dye with sufficient water, taken from the reservoir shortly before the run, to yield the proper jet dye concentration. This procedure resulted in no observable temperature discrepancy between the plenum fluid and the reservoir fluid. Using Eq. (A1), the estimated buoyancy length scale resulting from a temperature difference of 0.1 °C, the accuracy of the thermometer, is 1500 jet nozzle diameters. While, of the two contributions, the possible influence of a worst-case temperature mismatch is larger, the resulting buoyancy length is 15 times the distance between the nozzle and the measurement location at $x/d = 100$. Therefore, based on the criterion of Chen and Rodi,³¹ the momentum-dominated region extends for a distance that is over seven times longer.

A second way buoyancy may arise is through heating of the fluid in the measuring volume via absorption of laser power by the dye. The approximate residence time of the fluid in the measurement volume is the measurement height (80 μm) divided by the calculated mean centerline velocity at the lowest Reynolds number (0.072 m/sec), or 0.001 sec. We estimate the laser attenuation as no more than 5% across the width of the jet, and treat the jet concentration as uniform in the radial direction for the purposes here (not too severe an approximation—cf. Dahm¹²). The attenuation across the measuring volume ($5 \times 10^{-7} \text{ cm}^3$) would then be about 0.005%. Assuming a worst case (all power attenuation goes into heat), the resulting temperature rise would then be approximately 0.02 °C. While the approximation of uniform concentration and velocity may tend to underestimate the temperature rise, the actual laser attenuation through the entire jet diameter is closer to 3%, or so, with less than half of the attenuated power converted into heat. Therefore this estimate is conservative.

A second point concerning the heating of the fluid by the laser beam is that, while some dilatation of the fluid occurs as it passes through the laser beam, it is a localized effect. Importantly, there is no global buoyancy force to affect the large-scale jet structure and entrainment, as there is when the jet and reservoir densities are different. Thus it is not appropriate to utilize criteria such as those of Chen and Rodi¹¹ in this case, since they apply to the situation with globally different densities. The primary influence here, i.e., local dilatation, will have an even weaker effect on the flow for a given temperature rise. The dilatation is extremely small, $\Delta\rho/\rho \approx 5 \times 10^{-6}$, and we argue that its influence in our flow environment is also insignificant.

Having addressed the issue of attenuation, we should also consider the possibility of attenuation-caused fluctuations of the laser beam contributing to the measured values of c'/\bar{c} . The beam attenuation across the diameter of the jet was typically 3%, or less. Fluctuations arising from this attenuation may be completely uncorrelated with the scalar fluctuations at the measurement location, in which case the variances of the two contributions add. Alternatively, the fluctuations may be exactly correlated, in which case the two contributions to c'/\bar{c} add. In either situation, the maximum influence would correspond to fluctuations between the minimum (zero) and maximum ($\sim 1.5\%$) attenuation possibilities, or a maximum correction to the value of c'/\bar{c} of

roughly 0.015. This would result in, at most, a 7% change in the measured value. This should be compared with the large percentage decrease in the measured values over the Reynolds number range investigated (Fig. 4). Therefore, even in a worst-case scenario, the fluctuations arising from the attenuation of the laser beam would represent only a small correction to the magnitude of the variation we have measured. The actual situation is obviously not nearly so adverse, and we conclude that the attendant contamination of our results, as a result of beam fluctuations, is extremely small.

APPENDIX B: INTERPRETATION OF FLAME LENGTHS

Given the jet fluid concentration pdf's $p(c, x; \text{Re})$, the "flame length" can be estimated as the distance required for $1 - \epsilon$ of the jet fluid (with, say, $\epsilon = 0.01$) to have mixed to the proper composition (jet fluid fraction) c_* , as required by the chemical reaction. This is related to the stoichiometric mixture ratio (equivalence ratio) ϕ , by the expression

$$c_* = \phi_r / (\phi_r + 1), \quad (\text{B1})$$

where ϕ_r is equal to the parts of reservoir fluid that must be molecularly mixed and reacted for the complete consumption of one part of (pure) jet fluid.

Assuming that the highest values of the jet fluid concentration occur on the jet axis, to estimate the flame length corresponding to a given c_* and ϵ , we need two additional assumptions. First, that the pdf of concentration on the jet axis is a function of c/\bar{c} only, i.e.,

$$p(c, x) \approx f(c/\bar{c}), \quad (\text{B2})$$

where the function of $f(c/\bar{c})$ may vary with Reynolds number (and Schmidt number), but is taken as independent of x/d . Note that it is $f(c/\bar{c})$ that was plotted under this implicit assumption in Fig. 2. This is the usual assumption, recently corroborated for gas phase ($\text{Sc} \sim 1$) turbulent jets,¹¹ with supporting evidence for liquid phase ($\text{Sc} \sim 10^3$) jets.¹⁴ The second assumption deals with the dependence of \bar{c} on x/d , i.e. (momentum-driven turbulent jets)

$$\bar{c} = \kappa d^* / (x - x_0). \quad (\text{B3})$$

In this expression, the (pure) jet fluid concentration is taken as unity, the dimensionless parameter κ is taken as a constant (which may, however, depend on Reynolds number),¹¹ d^* is the jet momentum diameter,^{6,7,12} and x_0 is a virtual origin (possibly weakly dependent on Reynolds number at low Reynolds numbers). Combining Eqs. (B2) and (B3), we have, for each Reynolds number

$$p(c, x) \approx f\left\{[(x - x_0)/\kappa d^*]c\right\}. \quad (\text{B4})$$

For a given ϵ , the flame length L_f may then be estimated as the implicit solution of the equation

$$\int_0^\epsilon p(c, L_f) dc = \epsilon. \quad (\text{B5})$$

It can be seen that the computed flame length is determined by the behavior of the pdf at high values of c/\bar{c} . Basically, if $f_1(c/\bar{c})$ is the pdf of c/\bar{c} at a Reynolds number Re_1 , then for $c_*/\bar{c} > 1$ (small ϵ) and $f_2(c_*/\bar{c}) > f_1(c_*/\bar{c})$, we will have $L_{f2} > L_{f1}$. In other words, and as perhaps obvious in retro-

spect, a larger c'/\bar{c} (less well-mixed jet) implies a longer flame length.

The inferred flame length dependence on Reynolds number made above assumes that any deviations of the x dependence of $p(c,x)$ from Eq. (B2), as well as the possible dependence of d^* , κ , and x_0 on Reynolds number, are not strong enough to offset the relatively large dependence of L_f predicted using Eq. (B4) and the assumptions outlined above. We note, however, that the validity of these assumptions may not be unassailable, especially at the high Schmidt number in this experiment.²⁷

- ¹ H. L. Toor, *AIChE J.* **8**, 70 (1962).
- ² J. E. Broadwell and M. G. Mungal, *Phys. Fluids A* **3**, 1193 (1991).
- ³ M. G. Mungal and P. E. Dimotakis, *J. Fluid Mech.* **148**, 349 (1984).
- ⁴ M. M. Koochesfahani and P. E. Dimotakis, *J. Fluid Mech.* **170**, 83 (1986).
- ⁵ M. G. Mungal, J. C. Hermanson, and P. E. Dimotakis, *AIAA J.* **23**, 1418 (1985).
- ⁶ W. J. A. Dahm and P. E. Dimotakis, *AIAA J.* **25**, 1216 (1987).
- ⁷ W. J. A. Dahm and P. E. Dimotakis, *AIAA Paper No.* 85-0056, 1985.
- ⁸ D. Weddell, Ph.D. thesis, Massachusetts Institute of Technology, 1941.
- ⁹ H. C. Hottel, *The 4th (International) Symposium on Combustion* (Williams and Wilkins, Baltimore, 1953), pp. 97-113.
- ¹⁰ D. Kristmanson, and P. V. Dankwerts, *Chem. Eng. Sci.* **16**, 267 (1961).
- ¹¹ D. R. Dowling and P. E. Dimotakis, *J. Fluid Mech.* **218**, 109 (1990).
- ¹² W. J. A. Dahm, Ph.D. thesis, California Institute of Technology, 1985.
- ¹³ F. C. Lockwood and H. A. Moneib, *Combust. Sci. Technol.* **22**, 63 (1980).
- ¹⁴ P. N. Papanicolaou and E. J. List, *Int. J. Heat Mass Transfer* **30**, 2059 (1987).
- ¹⁵ P. N. Papanicolaou and E. J. List, *J. Fluid Mech.* **195**, 341 (1988).
- ¹⁶ D. A. Papantoniou, Ph.D. thesis, California Institute of Technology, 1985.
- ¹⁷ P. L. Miller and P. E. Dimotakis, *Phys. Fluids A* **3**, 168 (1991).
- ¹⁸ D. R. Dowling, Ph.D. thesis, California Institute of Technology, 1988.
- ¹⁹ N. Wiener, *Extrapolation, Interpolation and Smoothing of Stationary Time Series* (Wiley, New York, 1949).
- ²⁰ W. H. Press, B. P. Flannery, A. A. Teukolsky, and W. T. Vetterling, *Numerical Recipes. The Art of Scientific Computing* (Cambridge U. P., New York, 1986).
- ²¹ A. N. Kolmogorov, *Dokl. Akad. Nauk SSSR* **30**, 299 (1941); [*Usp. Fiz. Nauk* **93**, 476 (1967)] [*Sov. Phys. Usp.* **10**, 734 (1968)].
- ²² C. A. Friehe, C. W. Van Atta, and C. H. Gibson, *AGARD Turbulent Shear Flows CP-93*, 18.1-7, 1971.
- ²³ D. R. Chapman, *AIAA J.* **17**, 1293 (1979).
- ²⁴ G. K. Batchelor, *J. Fluid Mech.* **5**, 113 (1959).
- ²⁵ K. A. Buch and W. J. A. Dahm, *Bull. Am. Phys. Soc.* **34**, 2264 (1989).
- ²⁶ H. K. Moffatt, *Rep. Prog. Phys.* **46**, 621 (1983).
- ²⁷ P. E. Dimotakis and P. L. Miller, *Phys. Fluids A* **2**, 1919 (1990).
- ²⁸ K. R. Sreenivasan, *Phys. Fluids* **27**, 1048 (1984).
- ²⁹ W. J. A. Dahm, P. E. Dimotakis, and J. E. Broadwell, *AIAA Paper No.* 84-0369, 1984.
- ³⁰ H. B. Fischer, E. J. List, R. C. Y. Koh, J. Imberger, and N. H. Brooks, *Mixing in Inland and Coastal Waters* (Academic, New York, 1979).
- ³¹ C. J. Chen and W. Rodi, *Vertical Turbulent Buoyant Jets. A Review of Experimental Data* (Pergamon, Oxford, 1980).

Appendix B

GILBRECH, R. J. & DIMOTAKIS, P. E. 1992 "Product Formation in Chemically-Reacting Turbulent Jets," *AIAA 30th Aerospace Sciences Meeting*, AIAA Paper 92-0581.



AIAA 92-0581

**Product Formation in Chemically-Reacting
Turbulent Jets**

R. J. Gilbrech and P. E. Dimotakis

California Institute of Technology

Pasadena, CA

**30th Aerospace Sciences
Meeting & Exhibit
January 6-9, 1992 / Reno, NV**

Product Formation in Chemically-Reacting Turbulent Jets*

Richard J. Gilbrech** and Paul E. Dimotakis†

Graduate Aeronautical Laboratories
California Institute of Technology
Pasadena, California 91125

Abstract

Results from experiments performed in a newly-constructed High Pressure Combustion Facility are presented. The experiments described here are designed to address Reynolds number effects on turbulent mixing and entrainment, and flame length in an axisymmetric, gas-phase turbulent reacting jet, in particular, over a large range of Reynolds numbers.

Introduction

Flame length in kinetically fast chemical reactions can be used as an important measure of Reynolds number effects and can be related to the rate of molecular mixing in turbulent jets (*e.g.*, Broadwell 1982). The experiments reported here rely on a new technique for measuring flame length, developed for the purpose of investigating Reynolds number, as well as other effects on flame length.

The facility is shown schematically in Fig. 1. The main apparatus is a 107 cm internal diameter by 183 cm length (1.64 m^3) pressure vessel, capable of operating at pressures from 0.1 atm to 15 atm. This allows an independent control of Reynolds number over 2.2 decades through the pressure, while holding other conditions constant (*e.g.*, flow-time scales, nozzle exit conditions, and buoyancy effects). Buoyancy effects, which scale as $\overline{\Delta\rho}/\rho_\infty$, where $\overline{\Delta\rho}$ is the average change in density, in the jet cone, owing to heat release and ρ_∞ is the ambient density, remain constant as the pressure is varied since both $\overline{\Delta\rho}$ and ρ_∞ scale directly with pressure.

* Copyright ©1992 by R. J. Gilbrech and P. E. Dimotakis. Published by the American Institute of Aeronautics and Astronautics, Inc. with permission.

** Currently with NASA, Stennis Space Center, MS 39529. AIAA Member.

† Professor, Aeronautics and Applied Physics. AIAA Associate Fellow.

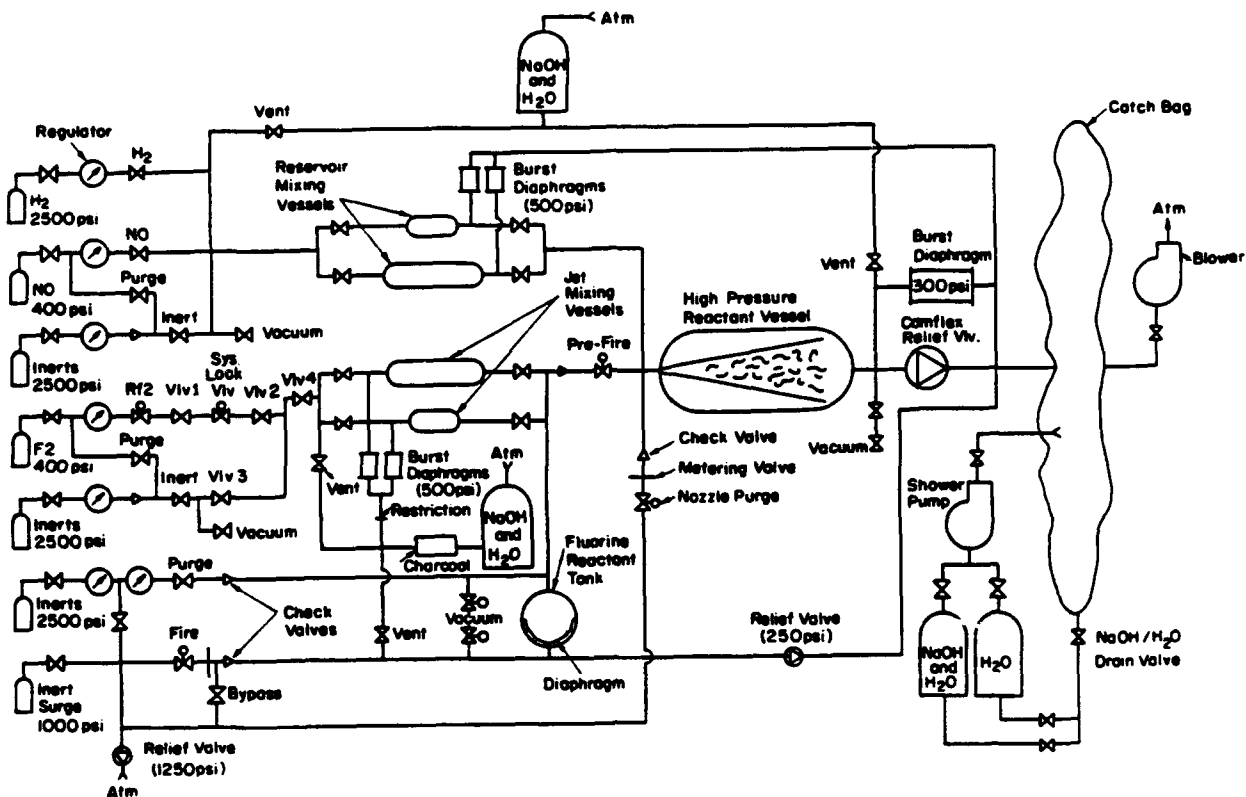


FIGURE 1 Schematic of the High Pressure Combustion Facility.

The chemical reactants chosen were F_2 and NO , diluted in N_2 , for several reasons. First, these reactants are hypergolic, obviating the need for ignition sources and avoiding flame stability issues. The resulting chemical kinetics are very fast, ensuring that the rate of chemical product formation is limited by the turbulent mixing process and not by the chemical kinetics (high Damköhler number regime), even at the low reactant concentrations employed here. Finally, an additional attractive characteristic of this chemical system is the ability to produce a very low adiabatic flame temperature rise, $\Delta T_f \sim 7\text{ K}$ for the experiments described here, mitigating buoyancy effects while retaining an overall reaction rate in the turbulent jet that is kinetically fast. On the other hand, the choice of these reactants, *vis-à-vis* safety considerations, dictates a strict adherence to materials properties, as well as facility assembly and maintenance, and experiment operating procedures.

In these experiments, the jet issues from the bottom of the pressure vessel upwards, through a 2.5 mm internal exit diameter nozzle that protrudes into the vessel. The radial profile of the internal nozzle contraction section is designed as a 6th order polynomial, optimized to avoid Taylor-Görtler vortices in the concave parts and for minimum exit boundary layer thickness. The outer nozzle profile is a paraboloid of revolution in an attempt to cater to the external potential flow field that is induced by the downstream entrainment.

The jet fluid is F_2 , diluted in N_2 . The reservoir fluid is NO , also diluted in N_2 . Partial pressure techniques utilizing intermediate mixing vessels are used to accurately produce the desired jet and reservoir concentrations. The jet charge is contained in a smaller volume (0.043 m^3) reactant tank which contains a teflon expulsion diaphragm. A metered sonic N_2 stream is fed to one side of the diaphragm, resulting in a fixed mass flow rate of jet gas through the nozzle. The reservoir pressure is held constant during the run with a Camflex pressure relief valve. See Fig. 1.

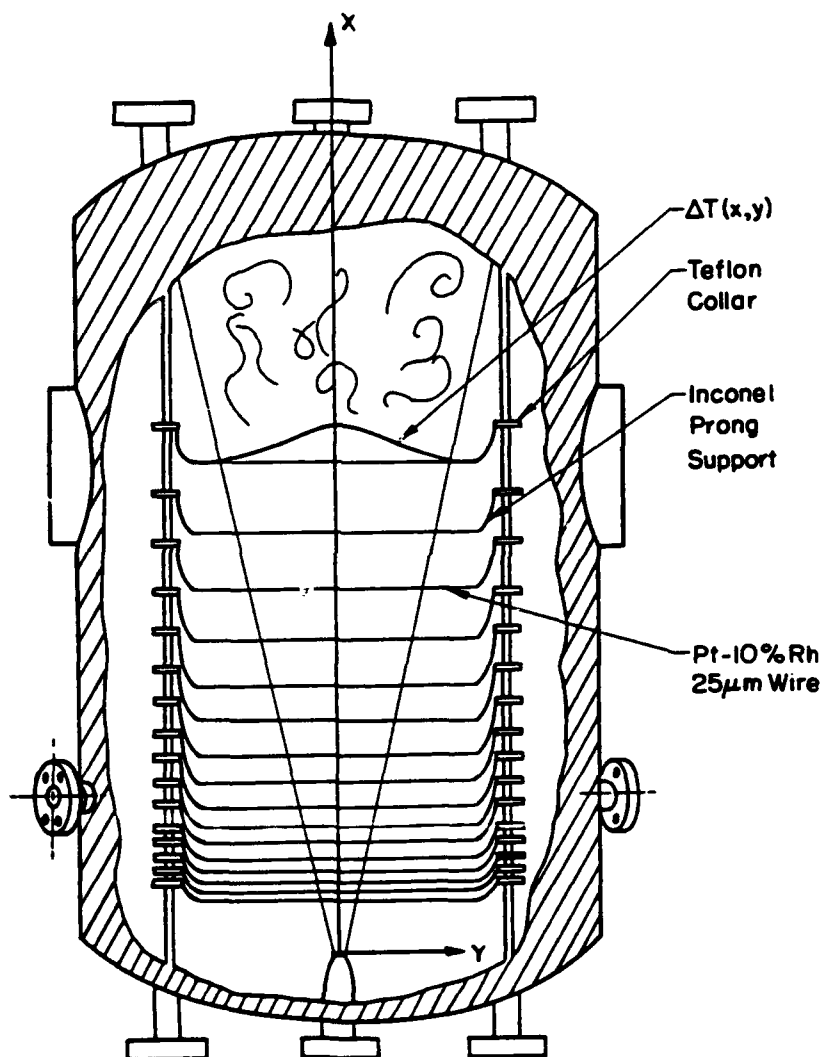


FIGURE 2 Schematic of jet geometry and diagnostics with the coordinate axes indicated.

The diagnostics utilized in these experiments were designed to give an accurate measure of flame length using constant current resistance thermometers. The thermometers are long (58 cm length), thin ($25\text{ }\mu\text{m}$ diameter), Pt-10%Rh wires,

stretched across the jet centerline at 16 axial locations, from $x/d_0 = 30$ to 240. Here x is the streamwise (jet-axis) coordinate and d_0 is the nozzle internal exit diameter. The wires extend well beyond the edges of the turbulent jet cone, spanning the heat release and temperature rise regions, at all downstream locations. The wire streamwise locations were selected to give uniform spacing on a $\log_{10}(x/d_0)$ axis. This spacing was suggested in view of a conjecture by Dimotakis that the line-integrated measurements of temperature rise in the flame region would depend logarithmically on x/d_0 . Figure 2 shows a schematic of the wires with the coordinate axes indicated.

Each wire formed one of the legs of a Wheatstone bridge circuit, whose output was amplified by a custom-built, low-noise signal amplifier, low-pass filtered by a third-order Butterworth filter with a knee set at 200 Hz, sampled at 500 Hz, and digitized to 12 bits. The wires were calibrated by allowing the interior of a slightly overpressurized vessel to equilibrate in temperature overnight and allowing the pressure to decrease over a few seconds in the morning. The resulting resistance change from each wire was recorded during the adiabatic cooling process. The small, common temperature drop experienced by each wire was estimated by measuring the internal vessel pressure using an electronic differential pressure transducer. In the course of a chemically reacting run, the mean temperature rise, determined from the change in total resistance of each wire, was estimated in this fashion to within, approximately, 30 to 50 mK.

The reason for choosing this particular measurement technique was motivated by the scaling laws of axisymmetric free turbulent jets. For the small heat release (temperature rise) employed in this experiment, the local wire resistance is a linear function of the local temperature. As a consequence, the total resistance of the cold wires, when stretched across the flame, yields an accurate estimate of the line-integrated heat release, *i.e.*, temperature rise, resulting from the chemical reaction.

At the end of the flame zone, shown schematically in Fig. 3, the F_2 has been completely consumed. No heat release occurs downstream of this location. Beyond the flame tip, at $x \simeq L_f$, the heat released by the reaction upstream is simply diluted by the subsequently entrained reservoir fluid. Therefore, for $x > L_f$, where L_f is the flame length, temperature excess is a conserved scalar.

Assuming that the flow achieves a self-similar temperature profile beyond the flame tip (as observed by Becker & Yamazaki 1978), the temperature rise for $x > L_f$ should obey the jet similarity law for a scalar quantity in a momentum-dominated jet. This similarity law can be derived from dimensional arguments (*e.g.*, Chen & Rodi 1980), has been verified experimentally (*e.g.*, Dowling & Dimotakis 1990), and is given by

$$\frac{\Delta T(x, y)}{\Delta T_f} = \kappa \frac{d^*}{x - x_0} g(\eta) , \quad (1a)$$

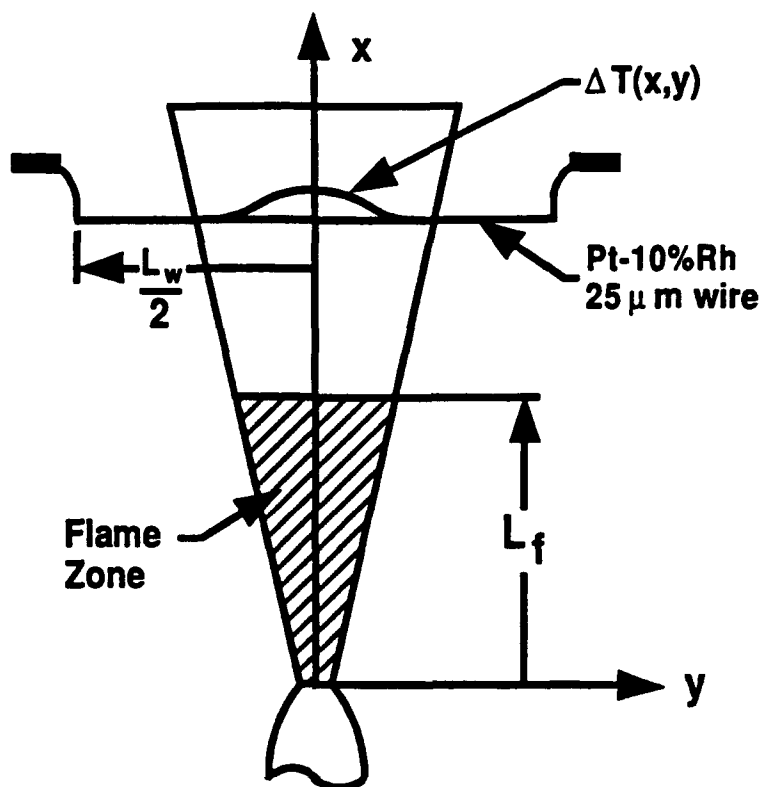


FIGURE 3 Schematic of the jet flame zone.

where $\Delta T(x, y)$ is the temperature rise at (x, y) , y is the transverse coordinate, ΔT_f is the adiabatic flame temperature rise, κ is a constant (determined by experiment), d^* is the momentum diameter of the jet, $g(\eta)$ is the similarity mean profile function (determined by experiment), η is the similarity variable defined as

$$\eta \equiv \frac{y}{x - x_0}, \quad (1b)$$

with x_0 the virtual origin. The function $g(\eta)$ has a maximum value of 1 at $\eta = 0$ and goes to zero outside the jet edges ($\eta > 0.25$). The momentum diameter d^* is considered to be the proper normalization for the downstream coordinate of the jet (e.g., Thring & Newby 1953, Avery & Faeth 1974, and Dahm & Dimotakis 1987), and is defined as

$$d^* = \frac{2\dot{m}_0}{\sqrt{\pi\rho_\infty J_0}}, \quad (2)$$

where \dot{m}_0 and J_0 are the nozzle exit mass and momentum fluxes, and ρ_∞ is the reservoir gas density.

Taking the line integral of Eq. 1a along y , at constant x (along a wire), and realizing that $g(\eta)$ goes to zero before $y = \pm L_w/2$, yields

$$\begin{aligned}
 \frac{1}{L_w} \int_{-L_w/2}^{L_w/2} \frac{\Delta T(x, y)}{\Delta T_f} dy &= \kappa \frac{d^*/L_w}{x - x_0} \int_{-L_w/2}^{L_w/2} g(\eta) dy \\
 &= \kappa \frac{d^*/L_w}{x - x_0} \int_{-\infty}^{\infty} g(\eta) dy \\
 &= \kappa \left(\frac{d^*}{L_w} \right) \int_{-\infty}^{\infty} g(\eta) d\eta \\
 &\neq f_n(x) ,
 \end{aligned} \tag{3}$$

where L_w is the span (length) of the wire.

As noted above, the measurement performed by each wire is the line integral of the temperature excess at constant x . This is given by

$$\frac{1}{L_w} \int_{-L_w/2}^{L_w/2} \Delta T(x, y) dy . \tag{4}$$

This quantity is analogous to the product thickness used for the shear layer (e.g., Dimotakis 1989). In particular, the product thickness $\delta_P(x)$, normalized by L_w , will be defined as

$$\frac{\delta_P(x)}{L_w} \equiv \frac{1}{L_w} \int_{-\infty}^{\infty} \frac{\Delta T(x, y)}{\Delta T_f} dy . \tag{5}$$

The product thickness $\delta_P(x)$ is equal to the width of a top-hat temperature profile of height ΔT_f that yields the same area as that found under the $\Delta T(x, y)$ temperature rise profile for that x location. Equations 3 and 5 are equivalent to Eq. 4 divided by ΔT_f .

The time-averaged, line-integrated mean temperature rise measured at each wire beyond the flame tip, i.e., for $x > L_f$, is expected to asymptote to a constant value. Accordingly, the line integral will rise to that asymptotic value as dictated by the cumulative mixing and chemical product formation up to that location for values of $x < L_f$.

Results and Conclusions

Figure 4 shows a sample of the raw data from the 16 wires spanning $x/d_0 = 30$ to 240, along with two reference wires placed outside of the jet cone at $x/d_0 = 0$ and 240, and the scaled velocity trace. Starting from the bottom trace and working upwards, the lowest trace is the reference wire at $x/d_0 = 0$ (partially obscured by the x -axis of the figure), then the 16 measurements from $x/d_0 = 30$ to 240, the other reference wire at $x/d_0 = 240$, and, finally, the scaled velocity trace. The reference wire at $x/d_0 = 0$ measures the temperature of the ambient reservoir fluid and the reference wire trace at $x/d_0 = 240$ indicates the arrival of hot recirculated products at the last measuring station, thus determining the temporal extent of uncontaminated data. The scaled velocity trace indicates the time required to establish steady state flow.

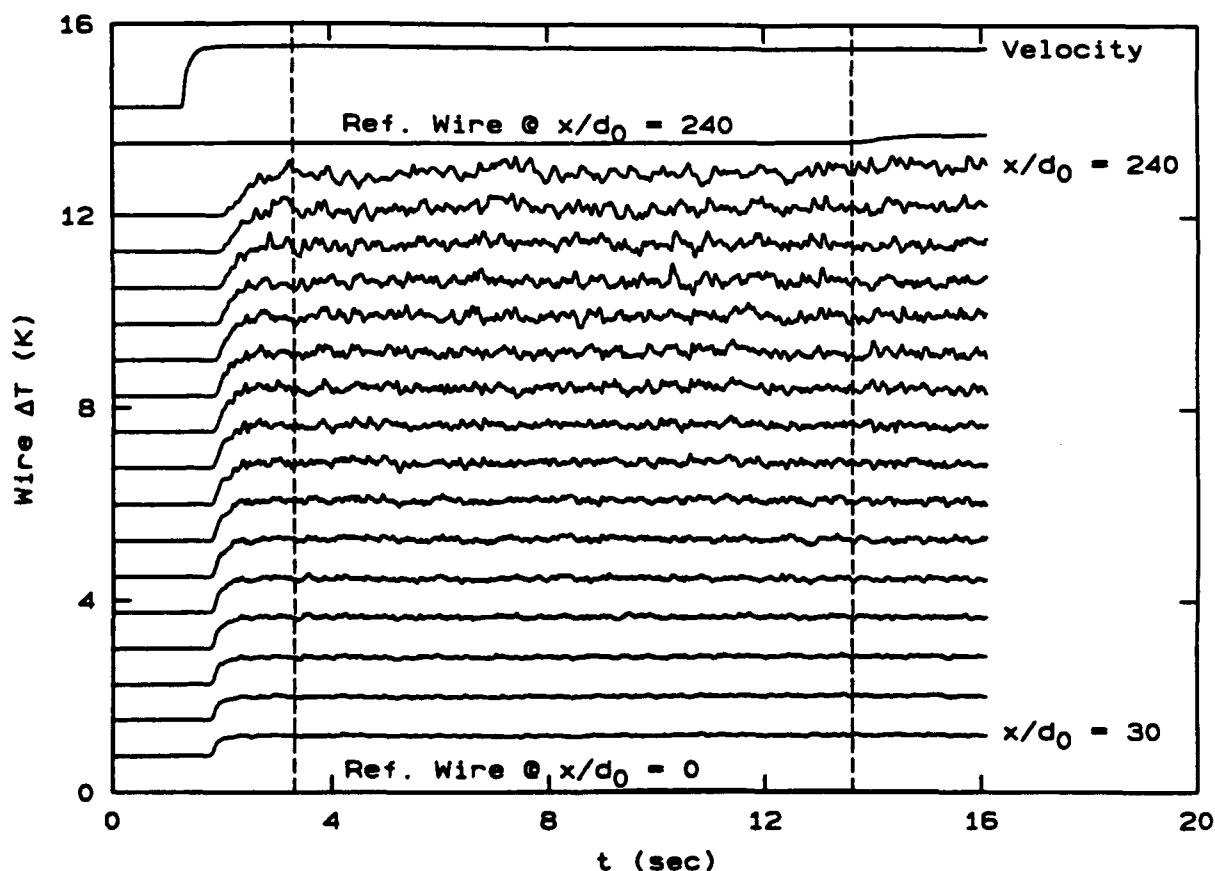


FIGURE 4 Sample traces of cold wire raw data for $\phi = 15$ and $\Delta T_i = 7$ K. Vertical dashed lines mark the averaging interval used for the corresponding data in Fig. 5. See text for details.

In the typical data in Fig. 4, note the small delay between the time the jet velocity has reached its steady value and the time the temperature rise is registered in the first wire at $x/d_0 = 30$. This time corresponds to the time required to flush the jet plenum of its original contents of reservoir fluid and charge it with the F_2 -bearing jet fluid. Note also the increasing delay required for the reaction head to reach the wires at increasing x/d_0 . The first vertical dashed line, at $t_1 \simeq 3.3$ sec, marks the beginning of the time interval over which the data from each wire are to be averaged. The second vertical dashed line, at $t_2 \simeq 13.6$ sec, marks the end of the averaging interval, prior to the arrival of the recirculating hot product gases, as registered on the top reference wire at $x/d_0 = 240$, outside the turbulent jet cone (second trace from the top). Note that the absolute span-averaged temperature change registered by the first wire is approximately 0.5 K. Small changes in the vessel temperature in the course of the run, as registered by the reference wire at $x/d_0 = 0$, are subtracted from the temperature registered by each wire and the difference for each wire is averaged over the selected (t_1, t_2) time interval for each run. As can be seen from the time-trace of the wire at $x/d_0 = 30$, the time-averaged mean temperature rise is determinable to a very good fractional accuracy.

The run recorded in Fig. 4 was for a stoichiometric mixture ratio of $\phi = 15$ and an adiabatic flame temperature rise of $\Delta T_f = 7$ K. The stoichiometric mixture ratio ϕ represents the mass of reservoir fluid that must be entrained, mixed on a molecular scale, and reacted to completely consume a unit mass of jet fluid. It is defined by

$$\phi \equiv \frac{(Y_{F_2}/Y_{NO})}{(Y_{F_2}/Y_{NO})_{st}}, \quad (6)$$

where, for a mixture of N species, the mass fraction, Y_i , is defined as

$$Y_i \equiv \frac{m_i}{\sum_{i=1}^N m_i}, \quad (7)$$

with m_i equal to the mass of the i^{th} species in the mixture. The resulting averaged data points from the run in Fig. 4 are depicted in the corresponding $\phi = 15$ trace in Fig. 5.

Data for a number of stoichiometric mixture ratios ϕ and an adiabatic flame temperature rise of $\Delta T_f = 7$ K were processed, as described above, to produce the plot depicted in Fig. 5. The data correspond to the nondimensional product thickness (Eq. 5) and are plotted versus $\log_{10}(x/d^*)$ for the four stoichiometric mixture ratios ϕ indicated. The solid line for each set of data is a compound curve fit with a linear least squares fit to the ramp region and a cubic spline fit to the knee region, with the appropriate matching of value, slope, and curvature at the crossover. The flame length L_f will be defined as the 99% of maximum δ_p/L_w point, in the same spirit as the definition of a 99% boundary layer thickness. The expected

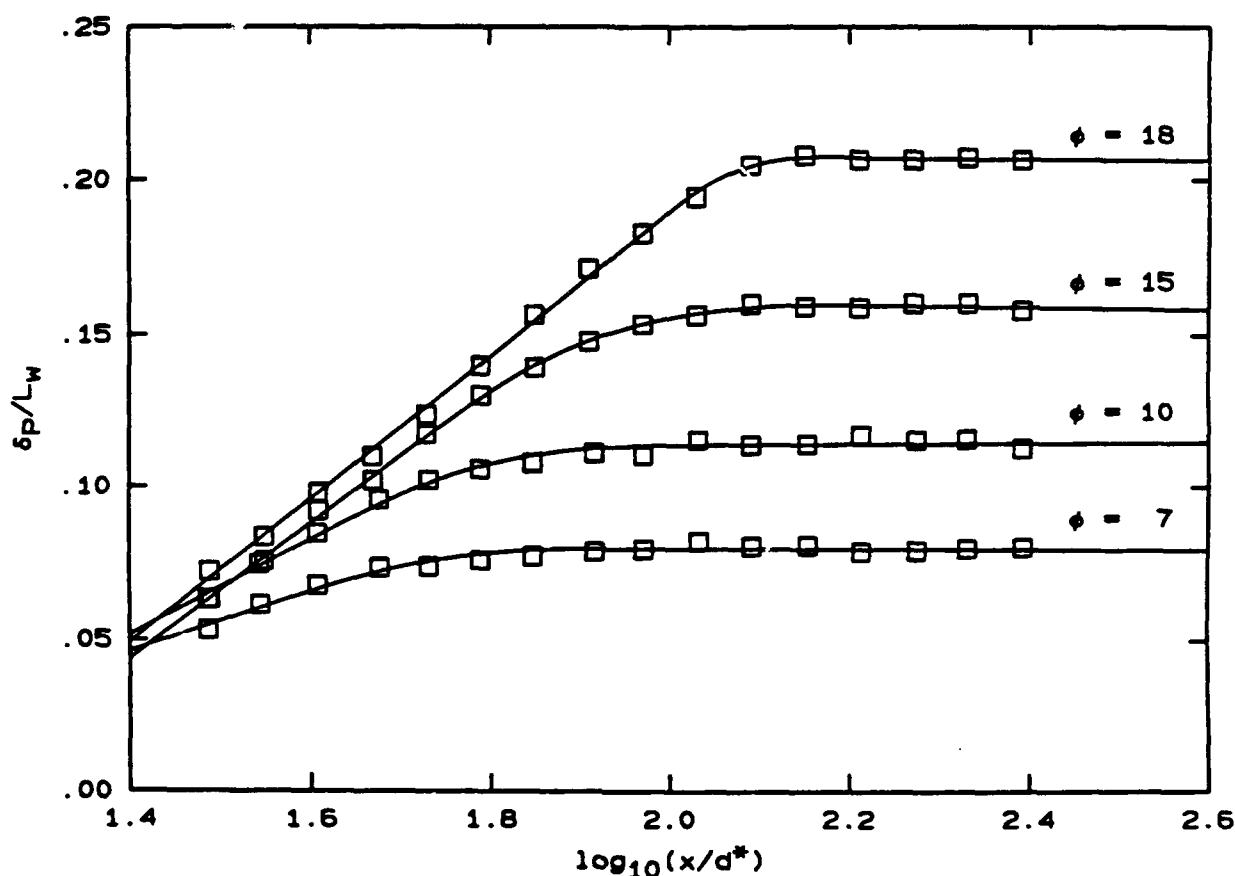


FIGURE 5 Sample plot of product thickness *vs.* $\log_{10}(x/d^*)$ for several ϕ 's and an adiabatic flame temperature rise of $\Delta T_f = 7$ K.

increase in the integrated temperature rise is observed, as well as the asymptotic value at the end of the flame tip. The constant temperature level measured by the wires beyond the flame tip is proportional to ϕ , as can be shown from simple scaling arguments. The results display a linear behavior in the flame region, when plotted in the semi-logarithmic coordinates suggested by the choice of wire spacing, and corroborate the conjecture by Dimotakis mentioned above.

The results of additional experiments will be reported in the near future that address the flame length dependence on Reynolds number, the transition of the jet from a momentum-dominated to a buoyancy-dominated regime, and the effects of finite rate kinetics (Dahmköhler number) on mixing in the turbulent jet.

Acknowledgements

We would like to acknowledge the contributions of Godfrey Mungal who was responsible for the initial design of the High Pressure Reactant Vessel and Dan Lang for the data acquisition system and the the wire signal amplifier circuits, discussions and other assistance by Cliff Frieler, David Dowling, Jeff Hall, Paul Miller, Gene Broadwell and Ed Zukoski. Finally, we would like to acknowledge the invaluable contributions of Earl Dahl in the construction and operation of the facility and experiments.

This work was jointly funded by the Gas Research Institute through Contracts 5083-260-0878 and 5087-260-1467, and the Air Force Office of Scientific Research through Grants 83-0213 and 88-0155.

References

AVERY, J. F. AND FAETH, G. M. [1974] "Combustion of a Submerged Gaseous Oxidizer Jet in a Liquid Metal," *15th Annual Combustion Institute*, 501-512.

BROADWELL, J. E. [1982] "A Model of Turbulent Diffusion Flames and Nitric Oxide Generation. Part I," TRW Document No. 38515-6001-UT-00, EERC Final Report, PO No. 18889.

BECKER, H. A. AND YAMAZAKI, S. [1978] "Entrainment, Momentum and Temperature in Vertical Free Turbulent Difusion Flames," *Comb. and Flame* **33**, 123-149.

CHEN, C. J. AND RODI, W. [1980] *Vertical Turbulent Buoyant Jets. A Review of Experimental Data* (Pergammon Press, Oxford).

DAHM, W. J. A. AND DIMOTAKIS, P. E. [1987] "Measurements of Entrainment and Mixing in Turbulent Jets," *AIAA J.* **25**(9), 1216-1223.

DIMOTAKIS, P. E. [1989] "Turbulent Free Shear Layer Mixing," *AIAA 27th Aerospace Sciences Meeting*, 9-12 January 1989 (Reno, Nevada), AIAA-89-0262.

DOWLING, D. R. AND DIMOTAKIS, P. E. [1990] "Similarity of the concentration field of gas-phase turbulent jets," *J. Fluid Mech.* **218**, 109.

THRING, M. W. AND NEWBY, M. P. [1953] "Combustion length of enclosed turbulent jet flames," *4th (International) Symposium on Combustion* (The Williams and Wilkins Co.), 97.

Appendix C

DIMOTAKIS, P. E. 1991 "Fractals, dimensional analysis and similarity, and turbulence," *Nonlinear Sci. Today* #2/91, pp. 1, 27-31.

Nonlinear Science

Totally

Fractals, Dimensional Analysis and Similarity, and Turbulence

Paul E. Dimotakis*

[Paul Dimotakis and K. R. Sreenivasan were invited to each write a brief piece on the relevance of fractals to the analysis and description of turbulence. The first of these follows; we hope to publish the second in a subsequent issue. — THE EDITORS]

In a series of papers and two books, Mandelbrot proposed to apply the notion of stochastic geometric similarity to describe a host of physical phenomena. This description was proposed as appropriate to phenomena that do not possess an inherent characteristic scale and give rise to sets that can be covered by a number $N(\lambda)$ of elements of size λ , given by

$$N(\lambda) \propto \lambda^{-D} \quad (1)$$

Sets whose coverage could be described in this manner he dubbed *fractal*, with the exponent D identified as the associated *fractal dimension*. See discussion in Mandelbrot [1977, 1982], and references therein.

Mandelbrot proposes that, in practice, the fractal dimension D can be determined by a straight line fit to a log-log plot of $N(\lambda)$ versus λ of the coverage law of Eq. (1). Equivalently, it can be computed from the logarithmic derivative

$$D = - \frac{d \log N(\lambda)}{d \log \lambda} \quad (2)$$

Strictly speaking, the dimension D is implicitly defined by Eq. (1), or Eq. (2), in the limit of $\lambda \rightarrow 0$. This is also the case for the *Hausdorff-Besicovitch dimension*, defined as the critical value of the exponent D , where the measure

$$M(D) = \sum N(\lambda) \lambda^D \rightarrow 0 \quad (3)$$

transitions from zero to infinity, in the limit of $\lambda \rightarrow 0$. The summation is to be taken over the set T with a factor $\lambda(D)$ that

*Graduate Aeronautical Laboratories, California Institute of Technology, Pasadena, CA 91125.

Continued on p. 27



Short time exposure photograph of burning "three-dimensional surface in a turbulent diffusion flame. Are such turbulent flow-generated interfacial surfaces fractal?" (Photograph © 1991 by Paul E. Dimotakis.)



PUBLISHED BY
SPRINGER-VERLAG
VOLUME 1, NUMBER 2 1991

Articles in this issue...

1 **Fractals, Dimensional Analysis and Similarity, and Turbulence**
Paul E. Dimotakis

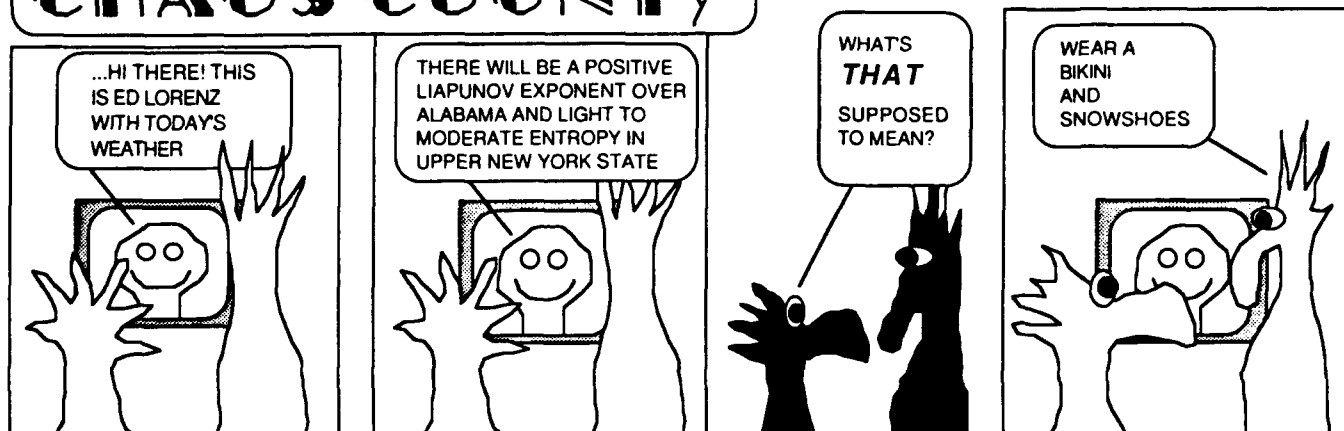
9 **Chaos, Contingency, and Convergence**
Jack Cohen and Ian Stewart

14 **Symmetry, Stability, Geometric Phases, and Mechanical Integrators (Part II)**
J. F. Marsden, O. M. O'Reilly, F. J. Wicklin, B. W. Zompro

Complete contents on p. 2

CHAOS COUNTY

by *Cesqore*



Dimotakis Continued from p. 1

can depend on the elements used to cover the set (see, for example, Feder [1988, p. 14]). In the Mandelbrot 1977 and 1982 discussions, the two quantities are used interchangeably, by considering cases, as he says, for which this equivalence can be accepted.

As Mandelbrot notes [1982, pp. 357–360], the basic mathematical ideas can be traced to earlier proposals and discussions. Equation (2) was essentially used by Pontrjagin and Schnirelman in the 30s, and the quantity D defined by Eqs. (1) and (2) can be identified with the *Kolmogorov capacity* (Kolmogorov and Tihomirov, 1959), or, as it was subsequently dubbed, the *box-counting dimension*. There can be no doubt, however, that it was Mandelbrot who realized the importance of these ideas, brought them to the attention of a community outside that of pure mathematics, and argued that they should be expected to prove applicable and useful in the description of many physical phenomena. A considerable body of research has appeared on the record in response to his proposals relating to a spectrum of phenomena too numerous to trace.

In the context of many of the phenomena proposed by Mandelbrot to be potentially describable by the fractal power law coverage similarity, however, one must require that Eqs. (1) and (2) hold for λ not only strictly positive, but over some nonvanishing range of scales λ , i.e., for

$$0 < \lambda_{\min} \leq \lambda \leq \lambda_{\max}. \quad (4)$$

This is a necessary assumption if one is to derive many of the benefits of this analysis. It will also prove important on another score.

Specifically, to return to the basic proposal, it is important to note that as regards the description of physical entities in which λ has units, Eq. (1) is *not dimensionally correct*; only a dimensionless group can be equal to a pure number. Of course, one could argue that a proportionality constant C is implicit in Eq. (1), i.e.,

$$N(\lambda) = C \lambda^{-D}. \quad (5)$$

Such a constant would be *dimensional*, however, with units as dictated by those of λ and the value of D , i.e., $C = \text{fn}(D)$. In using Eq. (5) as an implicit definition of D , in other words, in which D is the independent variable, the “constant” of propor-

tionality C is not a constant at all and hides important scaling information.

To illustrate the point, consider a set representing a surface in a d -dimensional (Euclidean) space, for example, fixed threshold crossing of a scalar time trace, or linear image ($d = 1$); isoscalar contours of a scalar field, e.g., $c(x, y) = c_{th}$, in a planar image ($d = 2$); or isoscalar surfaces, e.g., $c(x, y, z) = c_{th}$, of a scalar field in three dimensions ($d = 3$). Consider a volume given by L^d , in each case, where L is the (linear) extent of the space spanned by the data. The total number of λ -sized elements that can fit in this space is given by $(L/\lambda)^d$.[†] The total coverage $N_d(\lambda)$ of the set can then be expressed as the fraction of the number of λ -elements covering the set, times the total number of λ -elements in the d -dimensional (data) space, i.e.,

$$N_d(\lambda) = F_d(\lambda) \left(\frac{L}{\lambda} \right)^d. \quad (6)$$

The proposal that $N_d(\lambda) \propto \lambda^{-D_d}$ is then equivalent to a dependence of the coverage fraction on λ , i.e., the probability that a λ -element covers a portion of the set, given by

$$F_d(\lambda) \propto \lambda^{d-D_d}. \quad (7)$$

Since $F_d(\lambda)$ is a probability and therefore dimensionless, Eq. 7 requires that λ must be scaled by some like-dimensioned quantity, or characteristic scale, λ_0 , i.e.,

$$F_d(\lambda) = F_{d0} \left(\frac{\lambda}{\lambda_0} \right)^{d-D_d}. \quad (8)$$

We can combine this with Eq. 6 to yield what is implicit in the original equation, namely,

$$N_d(\lambda) = F_{d0} \left(\frac{\lambda}{\lambda_0} \right)^{d-D_d} \left(\frac{L}{\lambda} \right)^d. \quad (9)$$

In this expression, the now dimensionless constant F_{d0} is equal to the required fraction of set-covering elements of size $\lambda = \lambda_0$, provided, of course, the characteristic scale λ_0 falls within the $(\lambda_{\min}, \lambda_{\max})$ interval in which Eq. 9 applies. While, in principle, the factor F_{d0} could be absorbed in a redefined λ_0 , it is useful to retain it; the characteristic scale λ_0 might well be definable on some other physical basis quite independently of a fit to the coverage of the set of interest using Eq. 9.

[†]Barring edge effects, which, however, can be eliminated in any of a number of ways—for example, by considering λ 's that are exact binary submultiples of L , i.e., $\lambda_n = L/2^n$.

As an aside, it might appear that Eq. (3), the Hausdorff-Besicovitch expression for D , is not subject to the same difficulty. Strictly speaking, it is dimensionally correct as it stands. Nevertheless, one would prefer not to be using a measure that is *dimensional* (with units that depend on the value of D), or to be taking the limit with a *dimensional* $\lambda \rightarrow 0$, to determine the critical value of D . Instead, one would prefer a measure based on a *scaled* λ , e.g., $M(\lambda/\lambda_0; D)$, with D computed as the critical exponent in the limit of $\lambda/\lambda_0 \rightarrow 0$. Again, in other words, there is a need for a characteristic scale λ_0 , even if not as manifestly as with the box-counting coverage expression of Eq. (1).

These observations have an interesting consequence.

Returning to Eqs. (1), (5), or (9), we see that they can be expected only to apply to processes that observe a characteristic scale λ_0 . The resulting coverage function $N(\lambda)$ could then depend strongly on this characteristic scale, or not, depending on the value of the dimension exponent D . More importantly, however, the coverage of sets generated by processes that do not possess such a characteristic scale cannot be expected to be described by these equations.

Turning to the more specific question, an area in which there have been many attempts to apply power law fractals is "... the grand chapter of Physics, the study of turbulence in fluids" [Mandelbrot, 1977, p. 145]—the dynamics, in other words, of high Reynolds number fluid motion. Turbulent-flow-generated sets, especially at high Reynolds numbers, are known to exhibit a host of similarity properties. These can be expected to hold over a large range of space and time scales that are bracketed by

$$\lambda_{\max} \sim \delta, \quad (10a)$$

the outer flow scale, and

$$\lambda_{\min} \sim \lambda_K \equiv \left(\frac{\nu^3}{\bar{\epsilon}} \right)^{1/4}, \quad (10b)$$

the inner Kolmogorov [1941a] scale, in which ν is the kinematic viscosity and $\bar{\epsilon}$ is the mean dissipation rate of the kinetic energy per unit mass. At high Reynolds numbers Re , the bounds of this (inertial) range are in the ratio

$$\frac{\lambda_{\max}}{\lambda_{\min}} \sim \frac{\delta}{\lambda_K} \sim Re^{3/4}. \quad (11)$$

This potentially very large similarity range would seem to provide a promising arena for the Mandelbrot fractal proposals. Sets generated by turbulent flow processes that have been analyzed in this light include selected velocity component time traces, estimates of the local energy dissipation and its fluctuations, temporal as well as spatial scalar fluctuations and isoscalar surfaces, etc. The recent review by Sreenivasan [1991] can be consulted for a discussion and references.

Let us examine this proposal in view of some of the similarity properties in the inertial range of scales and the preceding discussion.

In his first and second similarity hypotheses, Kolmogorov [1941a] proposed that the only dynamically important quantity at a scale $\lambda = 2\pi/k$ within the range of Eq. (4), with the identifications in Eqs. (10), is the mean dissipation rate $\bar{\epsilon}$. This proposal immediately leads to the celebrated Kolmogorov $-5/3$ spectrum by dimensional analysis, i.e.,

$$E(k) \approx C_K \bar{\epsilon}^{2/3} k^{-5/3}, \quad (12a)$$

where C_K is a (dimensionless) constant of proportionality of order unity. The right-hand side is the only group that can be formed with $\bar{\epsilon}$ and k that has the requisite dimensions.

Physically, the first and second Kolmogorov hypotheses are equivalent to assuming that the dynamics of the turbulent strain-

ing motions that take an eddy of a scale λ_1 to a scale λ_2 , for

$$\delta \gg \lambda_1 > \lambda_2 \gg \lambda_K,$$

depend only on the local scale and therefore only on the ratio λ_1/λ_2 . In particular, they are equivalent to assuming that the dynamics do not depend on the ratio of the local scale λ to the outer scale δ , the inner scale λ_K or any other scale.

In subsequent refinements by Kolmogorov [1962], Oboukhov [1962], and others, the kinetic energy dissipation rate $\epsilon = \epsilon(\mathbf{x}, t)$ was accommodated as the local, intermittent field that it is. This introduced the outer scale δ as a scale *weakly* admissible in the dynamics, resulting in small corrections to the $-5/3$ spectrum. Specifically, with a log-normally distributed $\epsilon(\mathbf{x}, t)$, the energy spectrum becomes

$$E(k) \approx C_K \bar{\epsilon}^{2/3} (k\delta)^{-\mu/3} k^{-5/3}, \quad (12b)$$

where μ is the intermittency exponent, estimated to be in the range of $0.2 < \mu < 0.5$ (e.g., Monin and Yaglom [1975, p. 642]). Significantly, the difference between Eqs. (12a) and (12b) is too small to be discernible experimentally. At least by this measure, we may conclude that the Kolmogorov [1941a] hypothesis of scale independence, that leads to the $-5/3$ spectrum law, must very nearly be right.

This conclusion has consequences, in light of the preceding discussion of the need for a characteristic scale to exist, if the power law fractal similarity is to describe the coverage. In the case of sets with scales in the inertial range and the (near) absence of a characteristic scale λ_0 , we cannot expect Eq. (9) to apply if the fractal dimension exponent D_3 for coverage of three-dimensional sets is to be assigned values in the range of $D_3 = 2.36 \pm 0.05$, as was suggested, for example, by Sreenivasan [1991, p. 556]. This is also a value close to $D_3 = 5/2$ that Mandelbrot suggests "is reducible to the Kolmogorov theory and the empirical spectra,"^{††} which he also argues corresponds to a value of $D_2 = 5/3$ for planar sections [Mandelbrot 1977, p. 52].

We note here that, implicit in the assignment of both the reported experimental estimate of $D_3 = 2.36 \pm 0.05$ of Sreenivasan, as well as the correspondence between the value of $D_3 = 5/2$ and $D_2 = 5/3$ proposed by Mandelbrot as applicable to isoscalar surfaces, is the relation

$$d_1 - D_{d_1} = d_2 - D_{d_2}, \quad (13)$$

where d_1 and d_2 denote the topological dimension, e.g., $D_3 = D_2 + 1$ and $D_3 = D_1 + 2$, as was asserted by Sreenivasan and Meneveau [1986, Sec. 2.2]—recall also Eqs. (8) and (9). Specifically, in the case of the experimental values reported, the value of D_3 cited was inferred from measurements of one-dimensional ($d = 1$) or two-dimensional ($d = 2$) data, assuming Eq. (13). A suggestion to that effect had previously been made by Mandelbrot, whom Sreenivasan and Meneveau [1986] cite as a reference for this, and who says that "it is 'almost sure' " that the intersection of a three-dimensional surface with a plane yields a dimension $D_2 = D_3 - 1$ [Mandelbrot, 1982, p. 135], especially if the three-dimensional surface of interest is irregular (ibid., p. 136). The latter proviso would of course be satisfied in the case for an isoscalar surface in turbulence, for example (see also the discussion in Mandelbrot [1976, p. 124; 1977, p. 52] cited above). We will return to this point below.

Accepting Eq. (13) at face value for now, we can argue that such values for D_3 for an isoscalar surface, for example, are too far from the topological dimension of a three-dimensional object, i.e., $D_3 = 3$, and, despite Mandelbrot's assertion, that the resulting dependence of the coverage function $N_3(\lambda)$ on whatever

^{††}It is not clear whether Mandelbrot, in his reference here to "the Kolmogorov theory and the empirical spectra," is thinking of the original (1941a) arguments leading to the $-5/3$ spectrum [Eq. (12a)], or the revised (1962) proposals that lead to Eq. (12b).

characteristic scale λ_0 is used in Eq. (9) is too strong to be consistent with turbulent flow inertial range similarity. This conclusion can be reached by considering the properties of an isoscalar surface and its proposed (power law) fractal coverage $N_3(\lambda)$, assuming that

$$\lambda_0 \propto \delta, \quad (14)$$

as one might in view of the turbulent cascade process from larger to smaller scales. If we consider, for example, two gedanken experiments in the same type of flow, arranged to generate the same inner scales λ_K , but with outer scales δ_1 and δ_2 differing by, say, a factor of 10, and compare the coverage $N_3(\lambda)$ at a fixed scale λ , say, for $\lambda = 10\lambda_K \ll \delta_1, \delta_2$. The analysis of such a comparison is beyond the purposes of the present brief, informal discussion and is not included here.

This argument was recently noted in Miller and Dimotakis [1991], who did not find Eq. (1) [or, equivalently, Eq. (9)] applicable to measurements of temporal isoscalar intersections at a fixed point, or to spatial measurements derived from linear images, in the far field of turbulent jets where it had previously been reported to apply (e.g., Sreenivasan and Meneveau [1986]). In a note added in proof, Sreenivasan [1991] suggested that the discrepancy could be attributable to the fact that Miller and Dimotakis analyzed temporal data. As noted above, however, not only had such behavior been reported previously for temporal data,* but in their discussion Miller and Dimotakis included measurements and the analysis of temporal, spatial, as well as spatio-temporal (streak image) data, with similar results.

Briefly, to cover a total of N_T transitions in a one-dimensional record of length L , we must find

$$N_1(\lambda) \rightarrow \begin{cases} N_T & \text{for } \lambda \rightarrow 0 \\ L/\lambda & \text{for } \lambda > \delta. \end{cases} \quad (15)$$

The small-scale limiting behavior can be understood by appreciating that, once the covering element scale λ has decreased below the shortest separation between threshold transitions in the scalar trace, the total number of elements of size λ required to cover those transitions becomes equal to the total number N_T of transitions in the record of length L .

The large-scale limiting behavior can be understood by appreciating that every covering element of size λ much larger than the outer scale δ will cover transitions and, therefore, the total number of elements required to cover those transitions must tend to the total number of elements L/λ that can fit in the record. In other words, we must have $F_1(\lambda) \rightarrow 1$ for $\lambda \gg \delta$ (cf. Eq. 6). It is also easy to appreciate that, for typical traces derived from turbulent flow, the number of elements $N_1(\lambda)$ needed to cover the corresponding sets would only gradually approach the limiting values in Eq. (15), for small and large λ .

In view of the above and Eq. (2), we must have, for one-dimensional isoscalar data, that

$$D_1 \rightarrow \begin{cases} 0 & \text{for } \lambda < \lambda_B \\ 1 & \text{for } \lambda > \delta, \end{cases} \quad (16)$$

where λ_B is the Batchelor [1959] scalar diffusion scale (below which the isoscalar surface can be regarded as differentiable), and that, therefore, the exponent D_1 cannot be treated as a constant.

While it may be a minor point, it should be noted that if the measurements are alias-free with some margin, i.e., if they have been sampled at a frequency comfortably higher than the Nyquist

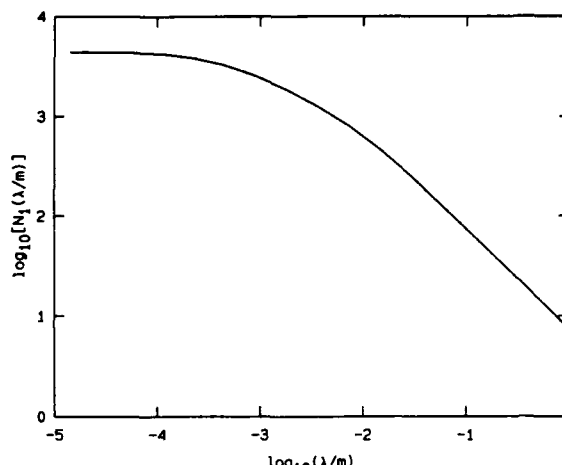


Figure 1: Coverage $N_1(\lambda)$ derived from temporal data of jet fluid concentration crossings of the local \bar{c} , measured on the axis of a turbulent jet at $x/d = 100$ and a Reynolds number of 1.15×10^4 . The scale λ here is converted to meters. Data from Miller and Dimotakis [1991].

frequency, and sufficiently noise-free, $N(\lambda)$ should tend to a constant at the smallest values of λ resolved by the data [for the reasons stated in reference to Eq. (15)] whether or not the smallest scale of the physical process has been resolved. It should also tend to the corresponding limit at large λ if the record length L spans a sufficient number of outer flow scales. Accordingly, we can always expect the limits in Eq. (16) to be attained by the analysis of proper data.

Of course, the preceding alone does not preclude, *a priori*, the existence of a $D_1(\lambda)$ that oscillates a constant value over a range of scales λ .

$$\lambda_B < \lambda_{\min} < \lambda < \lambda_{\max} < \delta,$$

in the case of isoscalar surfaces. That is rendered unlikely by the additional requirement for a characteristic scale λ_0 appropriate to that range, as noted above.

Rewriting Eq. (2), we conclude that, in general, we must allow the exponent D to be a function of λ , i.e.,

$$D_d(\lambda) = -\frac{d \log N_d(\lambda)}{d \log \lambda}, \quad (17)$$

as suggested in Miller and Dimotakis. In the analysis of their turbulent jet fluid scalar data, they find a $D_1(\lambda)$ smoothly rising from 0 to 1, over a range of jet Reynolds numbers, $3.0 \times 10^3 \leq \text{Re} \leq 2.4 \times 10^4$, with no indication of any preferred intermediate value. They also report that the observed $D_1(\lambda)$ is very close to one derived from a simple model process in which scalar threshold transitions are log-normally spaced.

Figure 1 depicts $N_1(\lambda)$, as required to cover transitions of the scalar jet fluid concentration trace $c(t)$, of a threshold set at the local mean \bar{c} ,* on the axis of a turbulent jet in water, at $x/d = 100$, and a Reynolds number of 1.15×10^4 . In this plot, the covering element scale λ was converted to an equivalent spatial extent, measured in meters, to facilitate comparison with other temporal data, at both higher and lower Reynolds numbers (cf. Miller and Dimotakis [1991, Fig. 4]). The outer scale (local jet diameter) is estimated to be $\delta \approx 0.11$ m, i.e., $\log_{10}(\delta/m) \approx$

*Note reference to the use of Taylor's frozen flow hypothesis in Sreenivasan, Ramshankar and Meneveau, [1989, Table 1]. Note (d), where the Sreenivasan and Meneveau [1986] jet data are cited.

*The important issue of the choice of the threshold was addressed in Miller and Dimotakis [1991]. The reader is referred to that discussion for further details.

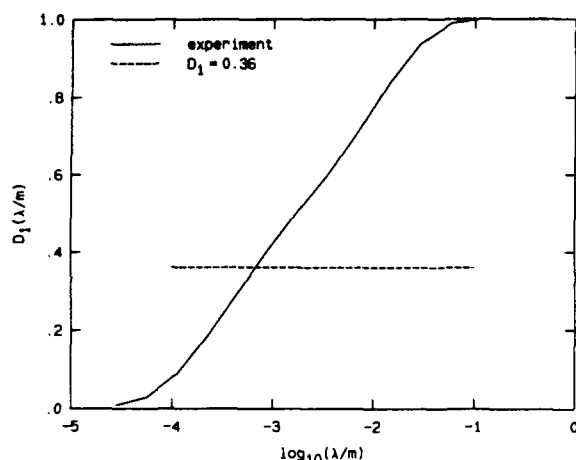


Figure 2: Logarithmic derivative $D_1(\lambda/m)$, Eq. (17), of the coverage $N_1(\lambda)$ plotted in Figure 1.

-1.0. As can be seen, the computed coverage observes the required limits noted in Eq. (15).

Figure 2 plots the logarithmic derivative $D_1(\lambda)$, computed from the $N_1(\lambda)$ coverage plotted in Figure 1. Note that the measured $D_1(\lambda) \rightarrow 0$, at the smallest scales, and $D_1(\lambda) \rightarrow 1$ for $\lambda \sim \delta$, or larger, as required. The dashed line in Figure 2 marks the level $D_1 = 0.36$. The latter was the value reported to have been derived from direct measurements of one-dimensional temporal data by Sreenivasan and Meneveau [1986]. It would also be the value derived from the previously cited estimate of $D_3 \approx 2.36$ if the assertion that $D_3 = D_1 + 2$ is accepted [Eq. (13)]. However, while the assertion of Eq. (13) may be true in special cases, it must in general be false, as will be argued below.

Consider an isotropic random surface in three dimensions, which we accept as possessing a fractal dimension D_3 , and its intersection with a plane, yielding a two-dimensional curve, which we will also accept as possessing a fractal dimension D_2 . Using the two-dimensional curve, we generate (extrude) a cylindrical surface by translating the two-dimensional curve along a direction perpendicular to its plane. As Feder [1988, Fig. 13.1 and related discussion] notes, the dimension of the resulting cylindrical surface, which has very different space-filling properties, is given by $D_2 + 1$. Equivalently, we can expect the required coverage fraction $F_1(\lambda)$, cf. Eqs. 6, 8, and 9, to be different for the original three-dimensional isotropic surface, vs. the generated cylindrical surface.

This suggests that for a random surface in three-dimensions, of dimension D_3 , and a planar section of the same surface of dimension D_2 , we can expect, in general,

$$D_3 \neq D_2 + 1 \quad (18)$$

(analogously, for curves that are originally planar of dimension D_2 versus linear cuts yielding intersections of dimension D_1).

Is the implication that there can be no (power law) fractals? Not at all.

To return to the earlier point on similarity and dimensional analysis, the inference that should be drawn is that a (power law) fractal coverage relation requires a characteristic scale. Without that, and as opposed to the original proposals, we cannot write Eq. (1) dimensionally correctly. Conversely, processes that do possess relevant characteristic scales could exhibit (power law) fractal behavior.

What is then the relevant characteristic scale for the triadic Cantor set (e.g., Mandelbrot [1977, p. 98]), often described as

self-similar, for example?

It is easy to appreciate that, for the triadic Cantor set, the characteristic scale is the original length L that is successively subdivided into thirds, i.e., $\lambda_0 = L$ in Eq. 9. The resulting set is obviously *not* self-similar at all scalings; it is not the same if we cut the original length L in half, for example. It is also not self-similar homogeneously; successive subdivisions do not endow the middle third of the original L with any Cantor "dust." Only the first and last third subsegments of any (sub)segment of the Cantor set are similar. This represents a rather restricted similarity scaling, which is pegged to the original length L and a coverage phased with respect to the original segment. The oscillations in the calculations of Smith et al. [1986], as well as in the spectrum of the triadic Cantor set,[†] can be understood in this light.

Accepting that the geometry of coastlines may be describable by a power law fractal relation, for example (cf. Feder [1988, Fig. 2.7]), one can think of several candidate characteristic scales that could be relevant. Potentially, these range from buoyant scales of the motion within the earth's mantle, responsible for tectonic motion on continental dimensions, to ocean wave scales at intermediate topography scales, to rock grain boundary and fracture scales, and below, as appropriate for microscopic and submicroscopic stochastic geometry scales. One could imagine the application of Eq. (9), corresponding to each of these separate characteristic scales, with, potentially, a different value of the exponent D for each one.

In the context of fluid mechanics and turbulence, this is also not to say that (power law) fractal relations and constant fractal dimension exponents are ruled out. The arguments here attempt to address issues arising in fully developed, turbulent flow in the intermediate, inertial range of scales, where power law fractals have been proposed to apply. Conversely, however, isoscalar surfaces that, for example, demark the boundaries of a turbulent region and even may serve as the definition of the outer scale δ are susceptible to dynamics that are obviously not independent of a characteristic scale, namely, the outer scale δ . Such interfaces would then appear to possess the necessary condition for a power law fractal description to be applicable and may indeed be found to display such behavior. It would then, however, be surprising if the resulting fractal dimension exponents were found to be universal, i.e., independent of the details of the flow geometry, Reynolds number, Schmidt number, etc.

More generally, however, one might accept the need to analyze stochastic geometric data, using the tools of fractal analysis, without requiring that they conform to power law similarity relations. Non-power-law stochastic geometry similarity could be useful for analogous purposes, as was suggested by Miller and Dimotakis, who instead found log-normal similarity applicable in their analysis of turbulent jet fluid scalar fluctuation records.

Indeed, the log-normal distribution was originally proposed by Kolmogorov (1941b) to describe the self-similar fragmentation process resulting from successive rock crushings.

Acknowledgments

Many people have contributed, over some time, to the evolution of these ideas. Over the last few years, I would like to acknowledge the many discussions at Caltech with Paul Miller, with whom the experiments cited here were conducted, as well as Tony Leonard. Without wishing to imply endorsement, I would also like to acknowledge some recent discussions with Uriel Frisch and Larry Sirovich that spawned improvements in the exposition of the arguments presented here.

[†]P. Miller, private communication.

References

- G. K. BATCHELOR [1959] Small-scale variation of convected quantities like temperature in turbulent fluid. Part 1. General discussion and the case of small conductivity, *J. Fluid Mech.* 5, 113–133.
- J. FEDER [1988] *Fractals*, Plenum Press, New York.
- A. N. KOLMOGOROV [1941a] Local structure of turbulence in an incompressible viscous fluid at very high Reynolds numbers, *Dokl. Akad. Nauk SSSR* 30, 299. Reprinted in: *Usp. Fiz. Nauk* 93, 476–481 (1967). Translated into English in: *Sov. Phys. Usp.* 10(6), 734–736 (1968).
- A. N. Kolmogorov [1941b] The logarithmically normal law of distribution of dimensions of particles when broken into small parts, *Akad. Nauk SSSR* 31(2), 99–101. Translated into English by V. Levin in NASA-TT F-12, 287 (1969).
- A. N. KOLMOGOROV [1962] A refinement of previous hypotheses concerning the local structure of turbulence in a viscous incompressible fluid at high Reynolds number, *J. Fluid Mech.* 13, 82–85.
- A. N. KOLMOGOROV AND V. M. TIHOMIROV [1959] ϵ -entropy and ϵ -capacity of sets in functional spaces, *Am. Math. Soc. Translations*, 1961 (Section II), 277–364.
- B. MANDELBROT [1976] Intermittent turbulence and fractal dimension: kurtosis and the spectral exponent $\frac{5}{3} + B$, *Turbulence and the Navier Stokes Equations, Conf. Proc.* (U. Paris-Sud, Orsay), 12–13 June 1975, *Lecture Notes in Mathematics* No. 565, Eds. A. Dold, B. Eckmann, Springer-Verlag, New York, pp. 121–145.
- B. B. MANDELBROT [1977] *Fractals. Form, Chance, and Dimension*, W. H. Freeman & Co., San Francisco.
- B. B. MANDELBROT [1982] *The Fractal Geometry of Nature*, W. H. Freeman & Co., New York.
- P. L. MILLER AND P. E. DIMOTAKIS [1991] Stochastic geometric properties of scalar interfaces in turbulent jets, *Phys. Fluids A* 3(1), 168–177.
- A. S. MONIN AND A. M. YAGLOM [1975] *Statistical Fluid Mechanics: Mechanics of Turbulence II*, J. Lumley (ed.), MIT Press, Cambridge, MA.
- A. M. OBOUKHOV [1962] Some specific features of atmospheric turbulence, *J. Fluid Mech.* 13, 77–81.
- L. A. SMITH, J.-D. FOURNIER, AND E. A. SPIEGEL [1986] Lacunarity and intermittency in fluid turbulence, *Phys. Lett. A* 114, 465–468.
- K. R. SREENIVASAN [1991] Fractals and multifractals in fluid turbulence, *Ann. Rev. Fluid Mech.* 23, 539–600.
- K. R. SREENIVASAN AND C. MENEVEAU [1986] The fractal facets of turbulence, *J. Fluid Mech.* 173, 357–386.
- K. R. SREENIVASAN, R. RAMSHANKAR, AND C. MENEVEAU [1989] Mixing, entrainment and fractal dimensions of surfaces in turbulent flows, *Proc. Roy. Soc. London A* 421, 79–108.